Freeze Casting – From Battery Separators to Ceramic Scaffolds

Thesis by

Chun-Wei Vince Wu

In Partial Fulfillment of the Requirements for

the degree of

DOCTOR OF PHILOSOPHY

CALIFORNIA INSTITUTE OF TECHNOLOGY

Pasadena, California

2023

Defended May 31, 2023

© 2023

Chun-Wei Vince Wu
ORCID: 0009-0002-4509-9713

ACKNOWLEDGEMENTS

I am also very grateful for all the support and help from my friends and cohorts at Caltech, particularly Newton Nguyen, Adrian Tan, and Andrei Ruskuc, and from the Caltech administrative staff, Christy, Jennifer, and Katie.

Finally, huge thanks to my family and friends in both Taiwan and Korea for their constant support. Their encouragement and belief in me serves as a driving force for me to keep going until I reach the final goal. Special and tremendous thanks go to my wife, Jiyoon Grace Shim. I cannot thank her enough for her unwavering love, care and support and always being on my side.

ABSTRACT

Freeze casting is a versatile pore-forming technique which allows tunability of pore structures including pore size, size distribution, morphology, and alignment in various material systems. It is that versatility that makes freeze casting a prospective candidate for fabrication of porous components used in a wide range of fields, ranging from biomaterials to supercapacitors. This work explores freeze casting as the processing route to fabricate battery separators and ceramic scaffolds.

The first part of this study assesses the feasibility of tape/freeze casting, a combination of tape casting and freeze casting, in fabricating battery separators for sodium-ion batteries. Poly(vinylidene fluoride-co-hexafluoropropylene) (PVDF-HFP) is chosen as the separator material due to its chemical inertness in battery environments, and dioxane is selected as the solvent for PVDF-HFP owing to its dendritic crystal structure and the absence of demixing upon freezing the solution. PVDF-HFP membranes fabricated by a bi-directional tape/freeze casting with dioxane exhibit through-thickness, directionally aligned pore structures. Although PVDF-HFP is shown to surpass reference separators in electrolyte affinity and electrochemical performance, composite strategies are designed to provide enhanced mechanical and electrochemical properties.

Firstly, the effects of alumina, a reinforcing agent introduced via ball milling with dioxane to form suspensions prior to tape/freeze casting, are examined. Composite PVDF-HFP/Al_2O_3 membranes show similar microstructures to their polymer counterpart, with enhanced resistance to thermal shrinkage, elastic modulus, electrolyte uptake, and ionic conductivity. Moreover, coin cells made with composite membranes deliver better rate performance and cycling stability than those with polymer membranes and filter paper reference materials.

Secondly, an alternative route to incorporate inorganic reinforcing elements into PVDF-HFP membranes is found through a co-solvent process. Silica particles from a sol-gel reaction of tetraethoxysilane (TEOS) are introduced into PVDF-HFP membranes via a co-solvent method in conjunction with dimethyl sulfoxide (DMSO). The tape/freeze-cast

PVDF-HFP membranes fabricated with DMSO alone exhibit directionally aligned pores, while a hierarchical pore morphology with circular pores on the aligned pore walls is observed in composite membranes fabricated with TEOS, and hence, silica additions. Composite PVDF-HFP/SiO$_2$ membranes outperform their unreinforced polymer counterpart in terms of elastic modulus, thermal stability, electrolyte affinity, and ionic conductivity, along with capacity retention and cycling performance when assembled into coin cells.

The final portion of this study evaluates the capability of freeze casting for highly permeable ceramic scaffolds using a polymethylsiloxane preceramic polymer with tert-butyl alcohol (TBA), a solvent creating prismatic pores without side arms that affords high permeability. A double-sided freeze-casting configuration results in more controlled freezing of the polymer solutions in comparison with the conventional single-sided counterpart, and hence a more aligned pore structure is obtained. Further improvement in pore alignment accompanied by an eight-fold increase in water permeability is realized by templating the substrate in freeze-casting molds.

PUBLISHED CONTENT AND CONTRIBUTIONS

[1] Chun-Wei Vince Wu, Xiaoping Lin, Abhinav Prabhakar, Zachary Kelly, Hansan Liu, and Katherine T. Faber. Tape/Freeze-cast PVDF-HFP/Al_2O_3 composite membranes for battery separators. Manuscript in preparation, 2023.
C. Wu conceived composite processing strategy, fabricated and characterized PVDF-HFP/Al_2O_3 composite membranes using SEM and FTIR, their porosities, thermal stability, and mechanical properties, and wrote the manuscript.

[2] Chun-Wei Vince Wu, Xiaoping Lin, Abhinav Prabhakar, Zachary Kelly, Hansan Liu, and Katherine T. Faber. PVDF-HFP/SiO_2 composite membranes for separators in Na-ion batteries. Manuscript in preparation, 2023.
C. Wu conceived composite processing strategy, fabricated and characterized PVDF-HFP/SiO_2 composite membranes using SEM, FTIR, and TGA, their porosities and mechanical responses, and wrote the manuscript.

[3] Advanced multifunctional battery separator membranes for novel liquid electrolytes and methods of use thereof.
Hansan Liu (Talos Tech), Vince Chun-Wei Wu (Caltech), Xiaoping Lin Talos Tech), Katherine T. Faber (Caltech).
United States Application No. 63/429,466; Caltech Ref.: CIT 8925-P, PAC Ref.: 22548.00004.

[4] Chun-Wei Vince Wu and Katherine T. Faber. Directionally aligned macroporous SiOC via modified freeze casting of polysiloxane/tert-butyl alcohol solution. Manuscript in preparation, 2023.
C. Wu fabricated and characterized SiOC samples using SEM and MIP and their permeabilities, and wrote the manuscript.

TABLE OF CONTENTS

LIST OF ILLUSTRATIONS

LIST OF TABLES

C h a p t e r   1

INTRODUCTION

1.1 Motivation

Freeze casting is a versatile pore-forming technique which relies on the removal of thermal energy to achieve phase segregation between the frozen solvent and the rejected solute or dispersed particles and the subsequent extraction of frozen solvent to leave porous structures patterned from the solidified phase. The versatility of freeze casting lies not only in its capability of tailoring pore structures by tuning processing parameters including solvent type, solid content, freezing front velocity, and thermal gradient, but also in its versatility for working with both solutions and suspensions and integrating with other processing techniques such as tape casting to form a hybrid tape/freeze casting. Because of this, freeze casting has been shown to be a promising route to produce a wide range of porous structures, ranging from porous polymer membranes to permeable ceramic scaffolds. Both of these will be treated in this thesis.

During the freezing of solvent, the inherent thermal gradient of freeze casting facilitates the growth of solvent crystals along the thermal gradient, and hence a directionally aligned pore structure results. A porous structure with directionally aligned pore morphology is advantageous when it comes to transport properties due to its low tortuosity which provides shorter transport paths. Directionally aligned pore morphologies with improved transport properties are found beneficial for applications such as separators for batteries and ceramic scaffolds which require high ionic conductivity and fluid permeability, respectively, two topics which will be treated in this thesis.

Amongst numerous types of batteries, despite the extensive use of lithium ion batteries (LIBs) in portable electronics, wearable devices, electric vehicles, and smart grids, concerns revolving around sustainability and safety due to limited Li source and battery failure are repeatedly in the spotlight. Hence, new battery technologies beyond lithium are being

extensively explored in the search for alternatives. Sodium ion batteries (SIBs) are considered to be one of the most promising alternatives due to the abundance of Na and the similarity in chemistry to that of LIBs. Although a great deal of research has focused on the development of electrode materials and electrolytes for SIBs, the separator, located between the electrodes to prevent short-circuiting while facilitating working ion transport, has not received as much attention as the other battery components. Currently, most SIB research relies on filter papers as separators, which are not practical for SIB commercialization due to their reactivity with electrolytes as well as their relatively large thickness. Moreover, adopting commercial separators for LIBs into SIBs is not a feasible option owing to the poor affinity of the commercial separators with cyclic carbonate electrolytes and ionic liquids that are particularly desirable for SIBs. Without appropriate separators, accurate and proper evaluation of electrochemical performance of SIBs is not feasible. As a consequence, the above challenges serve as motivation to develop a new class of separators with directionally aligned pores for better transport property and suitable for SIBs. Tape/freeze casting is an obvious candidate for processing such materials.

From the aspect of ceramic scaffolds, their permeability strongly depends on the pore morphology and alignments of scaffolds. Pore morphology is well known to be controlled by the choice of solvent [1]. Although tert-butyl alcohol (TBA) is found to exhibit a prismatic pore morphology which is useful for high permeability, the unstable growth of TBA crystals observed during conventional freeze casting reduces the resultant pore alignment [2]. In terms of pore alignment, apart from the inherent thermal gradient in freeze casting, external aids including grain-selection templates and magnetic fields have also been applied to improve the pore alignment. However, the employment of grain-selection templates extends processing time, while alignment improvement by magnetic fields is restricted to ferromagnetic materials. As a result, a search for a facile but effective way to obtain enhanced pore alignment along with excellent permeability in porous structures fabricated by TBA acts as our motivation.

1.2 Objectives

This work aims to explore the versatility of freeze casting for fabricating porous engineering materials, specifically polymer and composite membranes for separators in SIBs and permeable ceramic scaffolds. First, polymer-ceramic composite membranes which provide greater functionality and mechanical robustness to the design of separators are investigated. The feasibility of hybrid tape/freeze casting technique in fabricating polymer membranes with directionally aligned pore structures is assessed. Specifically, to reinforce the polymer membranes, oxide fillers including Al_2O_3 and SiO_2 are introduced via suspensions or via co-solvents during the freeze casting. More importantly, the effects of reinforcing oxide fillers on the microstructure, thermal stability, mechanical properties, electrolyte affinity, and electrochemical properties of polymer membranes when assembled into coin cells are appraised to establish the efficacy of the composite membranes for separators in sodium ion batteries.

Second, with regard to ceramic scaffolds, solvents that exhibit uncontrolled freezing behavior but desirable pore morphology under conventional freeze casting are explored. In order to control the TBA growth from preceramic polymer/TBA solutions, the reason for the uncontrolled growth is revealed by constructing a phase diagram of preceramic polymer and TBA. Moreover, to obtain better pore alignment, the effects of different freeze casting configurations, including single-sided (SS), double-sided (DS), and template-assisted double-sided (TDS) configurations, on the freezing behavior of the preceramic/TBA solutions and the resultant microstructures are studied. Additionally, the improvement in pore alignment in scaffolds when switched from the DS to the TDS configuration is assessed by water permeability measurements.

1.3 Thesis Organization

This thesis is organized as follows: Chapter 2 provides the necessary background on freeze casting, the freezing behavior of polymer solutions, and emerging applications of freeze-cast materials including battery separators and permeable ceramic scaffolds. Chapter 3 investigates the feasibility of the hybrid tape/freeze casting in fabricating separators for sodium ion batteries from PVDF-HFP/dioxane solutions. The effects of alumina, a reinforcing agent introduced via ball milling to form suspensions with the solvent, on the microstructure, thermal stability, mechanical properties, and electrolyte affinity of PVDF-HFP membranes are examined. Coin cells are assembled with tape/freeze-cast membranes to evaluate their electrochemical properties. Chapter 4 explores an alternative route to reinforcement through the incorporation of silica into the PVDF-HFP membranes through a co-solvent method with TEOS followed by a sol-gel reaction. The effects of TEOS on the freezing behavior of casting solutions and resultant microstructure of membranes are studied. Like the composite membranes with alumina additions, thermal, mechanical, and electrochemical properties are investigated to evaluate the membranes as separators for SIBs. Chapter 5 discusses the opportunity of different freeze casting configurations to fabricate permeable ceramic scaffolds with preceramic polymer and TBA and improve the pore alignment as well as water permeability. Chapter 6 summarizes the results, compares the properties of the two reinforced composite membranes, and concludes with suggestions for future studies.

C h a p t e r   2

INTRODUCTION

2.1 Freeze Casting

Freeze casting, also known as ice templating, is a form of sacrificial templating which utilizes the phase segregation between frozen solvent/dispersion medium and rejected solute/dispersed phase upon freezing to achieve porous structures. The process of freeze casting generally contains four steps, as summarized in Figure 2.1

First, casting suspensions/solutions are prepared by dispersing/dissolving powders/polymers in a dispersing medium/solvent (1a and 1b). Next is the critical freezing step in which the suspension/solution is frozen and the phase segregation between the dispersing medium/solvent and the dispersed phase/solute takes place. The dispersing medium/solvent crystals grow along the thermal gradient while expelling the dispersed/dissolved phase to form the resultant pore walls (2). Third, the frozen suspension/solution undergoes a sublimation process where the frozen phase is removed, leaving a porous body with a microstructure templated from the frozen phase (3). Lastly, depending on the material system, the porous body is sintered or pyrolyzed to densify or convert the polymer into ceramic (4a and 4b).

Despite the simplicity of freeze casting, a number of processing parameters can be tuned to tailor the resultant pore structure and accompanied properties. For example, while preparing for casting suspensions and solutions, solid content and choice of solvent/dispersing medium are easily adjustable. During solidification, freezing front velocity and thermal gradient are two dominant factors that affect the resultant pore structures. Apart from the two processing parameters, external aids such as grain-selection template and magnetic fields can be applied during freezing. The above processing parameters are discussed further in the following sections.
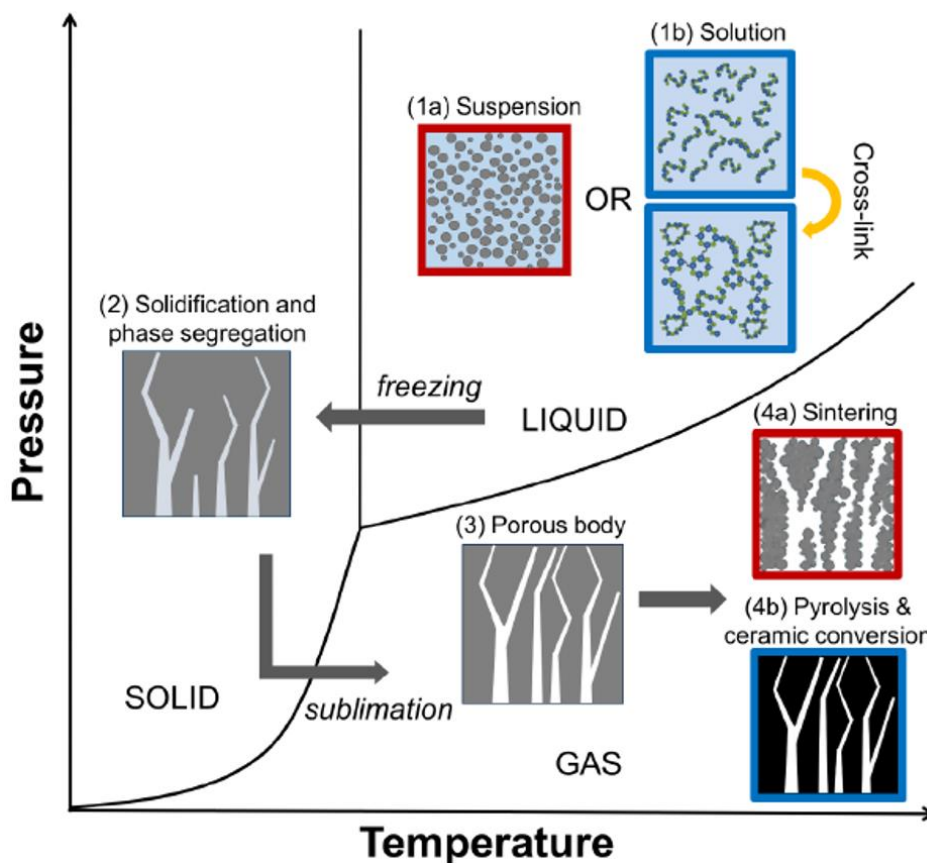
Figure 2.1 Schematic of the freeze casting process showing four steps: (1) preparation of solution or suspension, (2) solidification, (3) sublimation, and (4) sintering or pyrolysis [2].

2.1.1 Solid Content

The two main parameters associated with solid content are chemical composition and solid loading. Although the majority of work on freeze casting has centered on ceramic powders, metallic materials such as titanium [3, 4], iron [5], and nickel [6] have been studied while polymeric systems including poly(vinyl alcohol) (PVA) [7], poly(L-lactic acid) (PLLA) [8], poly(vinylidene fluoride) (PVDF) [9], and cellulose [10] have also been explored. It should be noted that freeze casting of polymers is essentially different from that of ceramic and metallic suspensions since polymers are usually dissolved in solvents to form solutions.

The porosity of the freeze-cast bodies is directly related to solids loading, that is the initial concentration of solutes or dispersed phase in solutions or suspensions. Low solids loading results in high porosity, which is beneficial for transport properties but often accompanied by compromised mechanical robustness. Alternatively, high solids loading leads to low pore fraction, which is advantageous from the aspect of mechanical properties, while the increased viscosity poses a challenge to obtain stable and homogeneous solutions or suspensions [11, 12]. Pore size of the freeze-cast structure generally decreases with increasing solids loading due to restricted solidification kinetics of solvent/dispersing medium during freezing caused by the high viscosity [13].

2.1.2 Solvents and Additives

Given that the pore structure of a freeze-cast body is a negative replica of the solidified solvent crystals, choice of solvent greatly influences the resultant pore morphology. A useful parameter to predict the structure of a solidified solvent is the Jackson alpha-factor, α [14].

$$\alpha = \frac{h_E \xi}{R T_E} \tag{2.1}$$

where h_E is the latent heat, ξ is an empirical factor dependent on the interface crystallography, R is the gas constant, and T_E is the equilibrium temperature between the solid and liquid phases. Generally speaking, crystals grow in a non-faceted manner with $\alpha < 2$, while faceted crystals with higher degree of anisotropy form when $\alpha > 2$ [15]. The Jackson alpha-factor can be seen as a product of an entropic term, h_E/RT_E, and a crystallographic term, ξ, which usually ranges between 0.25 and 1.

Table 2.1 Heat of fusion, melting point, entropic term of the Jackson alpha factor and pore morphology of selected solvents. Adapted from [2].

Solvent	Heat of fusion (kJ/mol)	Melting point (˚C)	Entropic term, h_E/RT_E	Pore morphology
Cyclooctane	14.6	2.41	1.01	Isotropic
Cyclohexane	6.5	2.68	1.15	Dendritic
Tert-butyl alcohol	25.3	6.70	2.70	Prismatic
Dimethyl carbonate	3.5	13.22	5.75	Lamellar

A connection between the entropic term of the Jackson alpha-factor and the structures of solidified solvent crystals with the resultant freeze-cast pore morphology has been made by Naviroj [2]. Table 2.1 lists four selected solvents including cyclooctane, cyclohexane, tert-butyl alcohol, and dimethyl carbonate in the order of increasing entropic terms of the Jackson alpha-factor. Figure 2.2 summarizes the optical micrographs of the crystal structures of the selected solvents along with their corresponding SEM micrographs from the freeze-cast bodies. With an increasing entropic term, distinct pore morphologies with growing anisotropy ranging from isotropic, dendritic, prismatic to lamellar structures have been shown to be created by cyclooctane, cyclohexane, tert-butyl alcohol, and dimethyl carbonate solvents, respectively. Although exceptions are seen in the cases of water with an intermedia value of 2.65 showing a lamellar structure [16] and dioxane forming dendritic crystals [2] despite a high value of 5.21, the entropic term of the Jackson alpha-factor serves as a good indicator of the solidified solvent structure and the corresponding freeze-cast pore morphology.
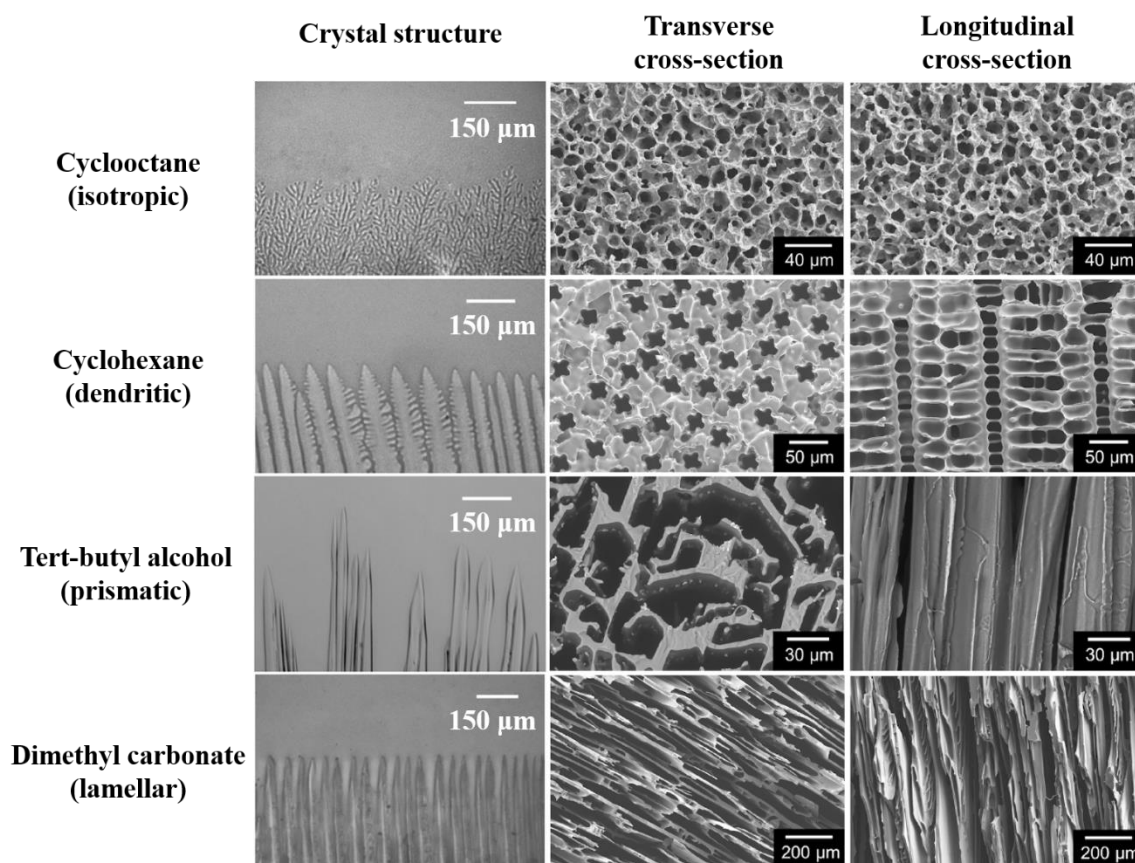
Figure 2.2 Optical micrographs of the SiOC crystal structures formed by selected solvents and the SEM micrographs of corresponding freeze-cast pore morphology. Adapted from [2].

Additives, including co-solvents, also have been introduced to regulate the solvent solidification behavior and therefore alter the resultant pore structures. Munch et al. studied the effects of various additives, including NaCl, sucrose, trehalose, glycerol, ethanol, gelatin, and citric acid, on the kinetics of ice growth and the microstructures of ice crystals [17]. In addition, a number of studies have suggested that the change in pore size is related to the change in viscosity caused by the polymeric additives, such as PEG [18] and PVA [19, 20]. Co-solvent effects on freezing point depression and pore size reduction are observed in dioxane/acetone [21] and dioxane/dimethyl sulfoxide systems [22]. Furthermore, co-solvents such as tetraethoxysilane (TEOS) are used to create hierarchical pore structures and as precursors for silica to produce polymer/ceramic composites [23].

2.1.3 Freezing Conditions

The freezing conditions during the solidification process have profound effects on the resultant pore structures since they directly affect the solidification behavior of the solvents. Figure 2.3 shows a microstructure selection map in which crystal morphology and size are a function of two important processing parameters, temperature gradient (thermal gradient), and growth rate (freezing front velocity) [24]. With control over the both parameters, freeze-cast bodies of identical chemistry but with different pore morphologies and varied pore sizes can be achieved. According to the microstructure selection map, a straightforward way to tune the pore size is to change the cooling rate, the product of thermal gradient and freezing front velocity. A higher cooling rate yields finer crystals and hence smaller pore sizes, whereas a lower cooling rate gives rise to coarser crystals and consequently larger pore sizes. Apart from pore size, Zeng et al. [25] and Arai et al. [26] have demonstrated the ability to migrate from the dendritic regime to the cellular regime on the microstructure selection map by carefully manipulating both thermal gradient and freezing front velocity.
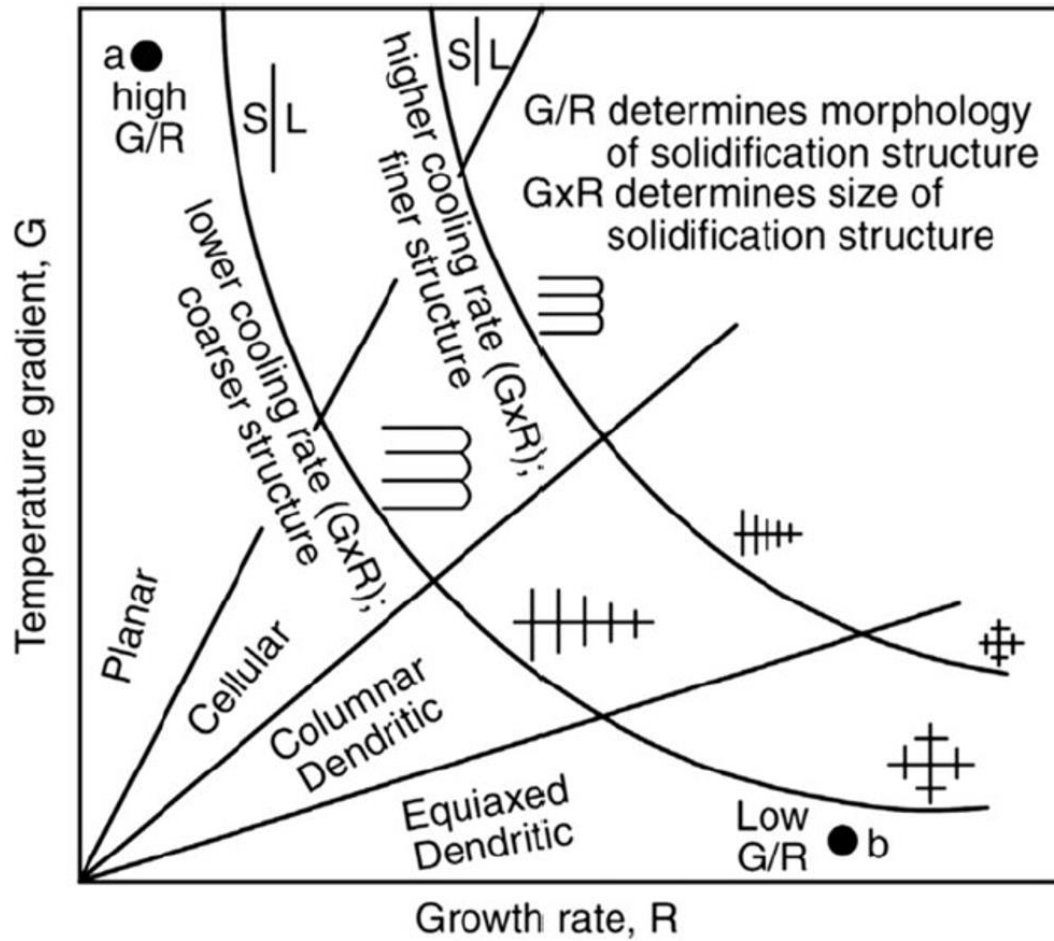
Figure 2.3 Microstructure selection map of crystal morphology and size as a function of temperature gradient and growth rate. Reprinted from [24] with permission from John Wiley and Sons, Inc.

The direction and magnitude of the thermal gradient during solidification are two dominant factors that determine the alignment of the frozen crystals, and hence the pore alignment. Solvent crystals grow in a resultant direction controlled by the imposed thermal gradient and the preferred growth direction of the crystals, as illustrated in Figure 2.4 [16].
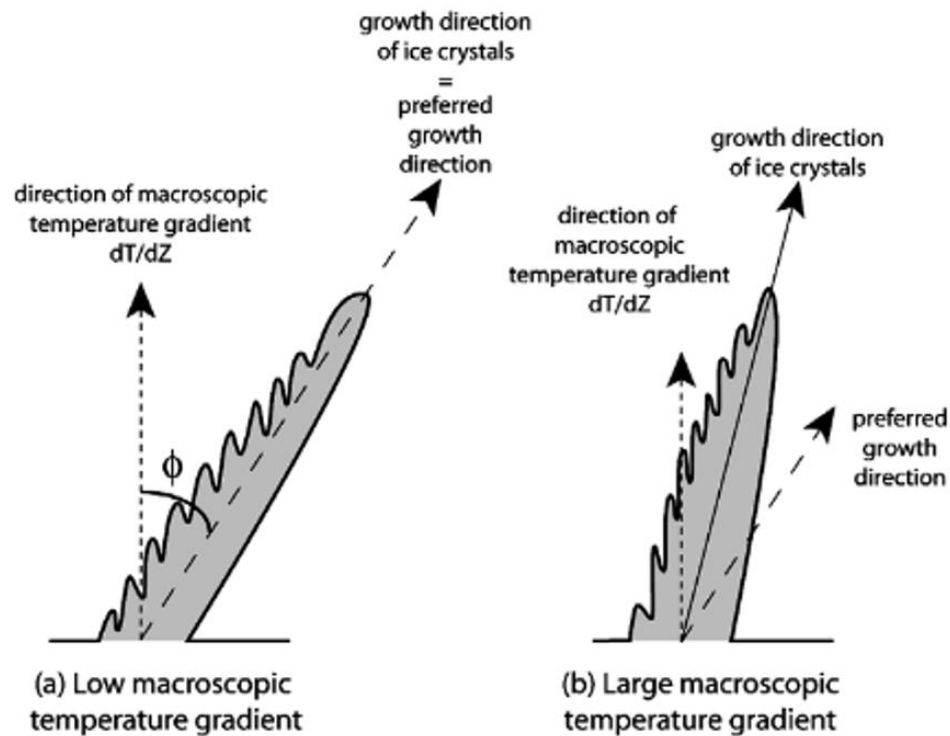
Figure 2.4 Alignment of ice crystals and relationships with imposed thermal gradient and preferred growth direction for two thermal gradients. Reprinted from [16] with permission from Elsevier.

Conventional freeze casting is conducted in a unidirectional fashion where a cooling source is placed at the bottom of the casting solution or suspension to induce direction freezing. However, several studies have employed different freeze casting setups to produce dual and radial thermal gradients. Waschkies et al. [27] have demonstrated that a long-range, lamellar structure with almost constant lamellar spacing can be fabricated by controlling the solidification velocity of particle-water-suspensions with a double-sided cooling setup. Su et al. [28] have shown that freeze-cast samples produced by radial-concentric freeze casting exhibit radially aligned microstructure and thus show better axial compressive modulus and splitting tensile strength than the samples made via conventional freeze casting. Bai et al. have shown the nucleation of ice crystals can be controlled under dual temperature gradients

by modifying the cold finger with a polydimethylsiloxane (PDMS) wedge, as shown in Figure 2.5 [29].
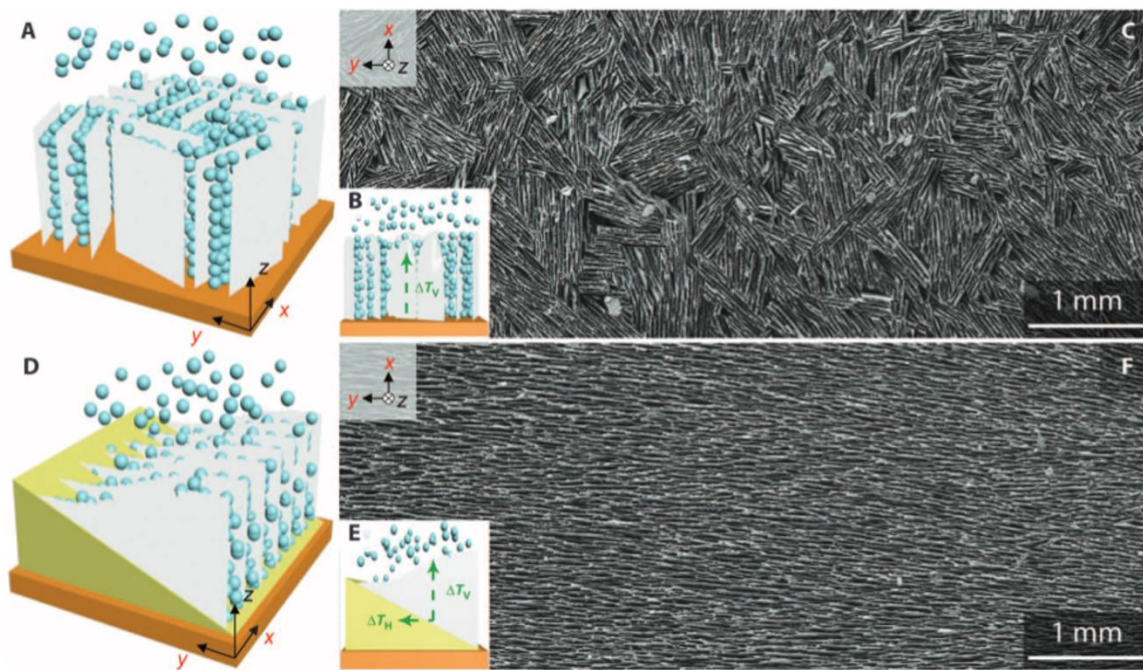
Figure 2.5 Short-range, multiple-domain lamellar structure and long-range, mono-domain lamellar structure created by conventional and bi-directional freezing techniques from [29]. Reprinted with permission from AAAS.

2.1.4 External Aids

In addition to the intrinsic factors of freeze casting discussed above, extrinsic factors including mechanical templates and externally applied fields can also be implemented to regulate the pore structures. Han et al. [30] employed a polymer sponge that serves as a sacrificial placeholder in the slurry to produce additional porosity in the freeze-cast structure. Naviroj et al. [31] have utilized a grain-selection template to limit the nucleation process during solidification and thus improve the pore alignment. Figure 2.6 (a) [32] shows that application of a static or rotating magnetic field on TiO_2 slurries doped with Fe_3O_4 promotes long-range alignment of lamellar structures. Zhang et al. [33] have demonstrated that the

dense layer thickness in a dense/porous bilayered Al_2O_3 structure can be controlled by the intensity of electric fields, as shown in Figure 2.6 (b).
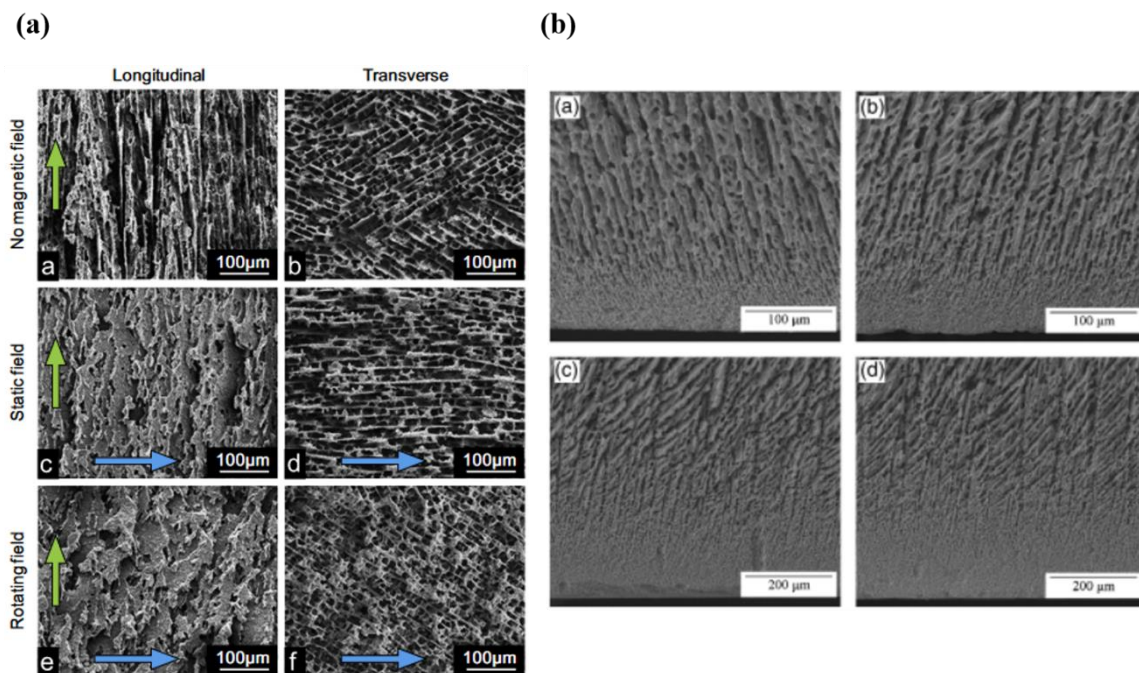
Figure 2.6 (a) SEM micrographs showing the effects of magnetic field alignment on the TiO_2 scaffolds alignment containing 3 wt% Fe_3O_4 (Reprinted from [32] with permission from Elsevier) (b) SEM micrographs showing the effects of electric field intensity on dense layer thickness of bilayered Al_2O_3 structures (Reprinted from [33] with permission from John Wiley and Sons, Inc.).

A hybrid technique, freeze tape-casting (or tape/freeze casting), combines the processing steps of tape casting (doctor blading) and freeze casting to fabricate large-area tape samples. First, a suspension is tape-cast onto a casting bed by a doctor blade. Then, the casting bed is moved towards a freezing zone to induce directional freeze casting, as illustrated in Figure 2.7 (a). Freeze tape-casting is effective in fabricating aligned pore structures and the pore morphology can be tuned by controlling the freezing temperature. This technique has been used in both aqueous and non-aqueous ceramic suspensions such as yttria-stabilized zirconia/water, yttria-stabilized zirconia/tert-butyl alcohol [34], and TiO_2/water [35] to

produce ceramic sheets. Kim et al. have demonstrated that this technique can be adopted in polymeric systems including PVDF [36] and PVDF/TiO$_2$ (Figure 2.7 (b)) [37] to fabricate polymer and composite membranes with directional pores.

(a)
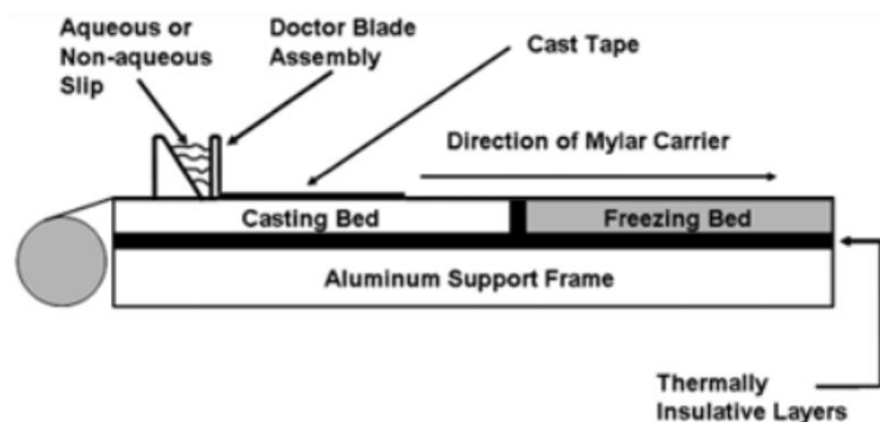
(b)
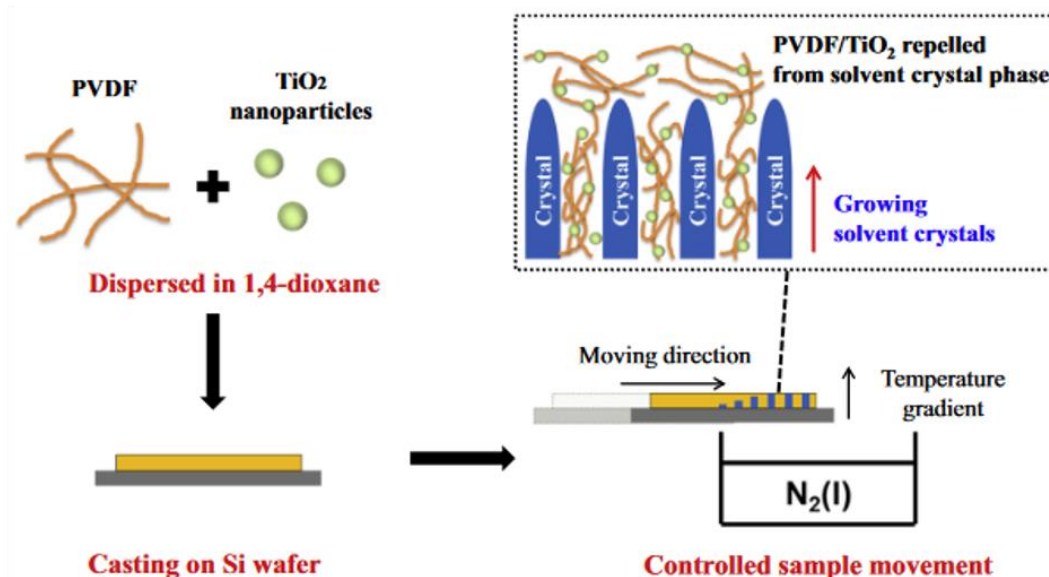
Figure 2.7 (a) Schematic of freeze tape-casting (Reprinted from [34] with permission from John Wiley and Sons, Inc.) (b) Fabrication process of PVDF/TiO$_2$ composite membranes with directional pores. (Reprinted from [37] with permission from Elsevier).

2.2 Polymer Solutions

2.2.1 Solubility Parameters

Given that polymer solutions are used throughout this thesis, this section aims to provide some background information about solubility parameters, an important and widely used concept for solvent selection for freeze-cast polymers. The use of solubility parameter to explore suitable solvents is based on the well-known chemistry rule of "like dissolves like": if the intermolecular forces between the molecules of a solvent are of similar strength to those between the molecules of a solute, the solvent is usually a good solvent for this solute. The intermolecular forces can be estimated by the total cohesive energy (E_t), which is a sum of individual contributions from the non-polar (dispersion) interactions (E_d), polar (dipole-dipole and dipole-induced dipole) interactions (E_p), and hydrogen bonding (including Lewis acid-base interactions) (E_h) [38],

$$E_t = E_d + E_p + E_h \tag{2.1}$$

By dividing each cohesive energy term by the molar volume (V), the total cohesive energy density can be expressed as the sum of individual cohesive energy density.

$$\frac{E_t}{V} = \frac{E_d}{V} + \frac{E_p}{V} + \frac{E_h}{V} \tag{2.2}$$

Solubility parameter is defined as the square root of the cohesive energy density, and therefore the square of the total solubility parameter is the sum of the squares of the dispersion-based, polar-based, and hydrogen bonding-based solubility parameters [39].

$$\delta_t^2 = \frac{E_t}{V} = \delta_d^2 + \delta_p^2 + \delta_h^2 \tag{2.3}$$

The distance between two molecules, a solute (i) and a solvent (j), in the 3D Hansen space is defined as R_a and can be calculated by their respective solubility parameters [40],

$$R_a = \sqrt{4(\delta_{d,i} - \delta_{d,j})^2 + (\delta_{p,i} - \delta_{p,j})^2 + (\delta_{h,i} - \delta_{h,j})^2} \tag{2.4}$$

For a particular solute, solvents experimentally tested for solute solubility are plotted in the 3D Hansen space to create the so-called solubility sphere. This sphere, with a radius known as the interaction radius, R_0, defines the region in the 3D Hansen space where a solution is formed by a solute-solvent pair. The ratio of R_a to R_0 is termed as the relative energy difference (RED), which serves as a reference for solubility of solute (i) in a solvent (j).

Consequently, good solvents are located in the interior of the sphere or at least on the sphere surface, corresponding to RED ≤ 1, while RED > 1 suggests low affinity between the solute and solvent, as illustrated in Figure 2.8 [41].
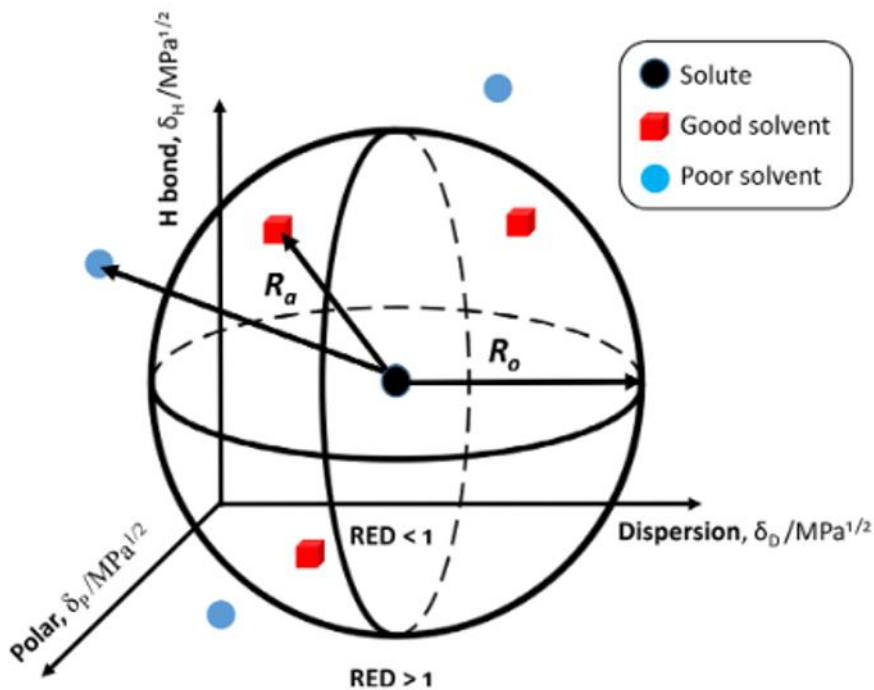
Figure 2.8 Solubility sphere with a radius R_0 in the 3D Hansen solubility space showing good solvents (red) located within the sphere with RED values smaller 1 and poor solvents (blue) located outside of the sphere with RED values greater than 1. Reprinted from [41] with permission from Elsevier.

2.2.2 Freezing in Polymer Solutions

Since the pore-forming mechanism of freeze casting is the freezing of the solvent, it is imperative to understand the fundamentals of freezing in polymeric casting solutions from the point of view of thermodynamics. Figure 2.9 shows a typical phase diagram of a polymer-solvent system [42] in which A, B, and T_c refer to the binodal curve, the spinodal curve, and the critical temperature, respectively, while C and D denote the solvent freezing point curves with T_f being the freezing point of the pure solvent. In the region between A and B, the

solution undergoes liquid-liquid phase separation (LLPS) by nucleation and growth. On the other hand, in the B region, a spontaneous liquid-liquid phase separation without the requirement of nucleation, also known as the spinodal decomposition, occurs in the solution. When the solution is cooled along the line indicated by arrows, the homogeneous solution phase separates by nucleation and growth as it enters the region between curves A and B. Further cooling of the solution leads to spinodal decomposition as the solution passes beyond curve B. Subsequently, the solvent in the solution freezes as temperature goes below the freezing point curve C.
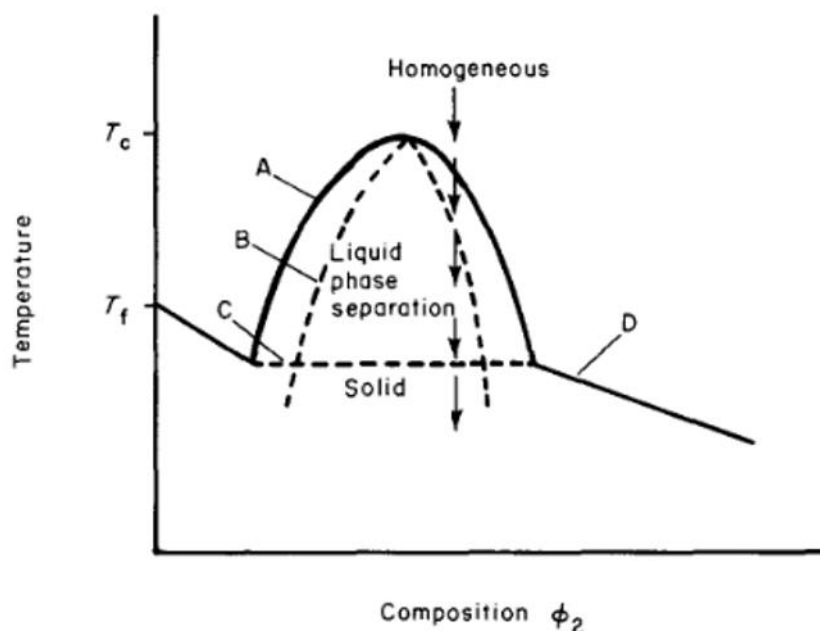
Figure 2.9 Typical phase diagram of a polymer-solvent system. Reprinted from [42] with permission from Elsevier.

Figure 2.10 (a) [42, 43] presents the schematic phase diagram of polystyrene and cyclohexane similar to that shown in Figure 2.9 along with the resultant polystyrene morphology. Due to the large difference between T_c and T_f, the solution undergoes liquid-liquid phase separation prior to the freezing of the solvent, evidenced by the observation of cloudiness formation in the solution before freezing. Given that the phase separation

precedes the freezing of the solvent, a polymeric foam with an isotropic pore morphology is observed. In contrast, Figure 2.10 (b) [42, 43] shows the representation of a phase diagram of polystyrene and benzene where the binodal and spinodal curves are far below the freezing point curve. In such systems, no cloudiness is observed in the solution prior to freezing, which indicates the absence of liquid-liquid phase separation before the solvent freezing. When the temperature of the solution is cooled below T_f, the solvent freezes along the thermal gradient and pushes the polymer aside. Therefore, the resultant morphology is determined by the growth of the frozen solvent crystals, leading to a more anisotropic microstructure as shown in Figure 2.10 (b). As a result, the resulting microstructure of the freeze-cast structure is greatly dictated by the relative positions of the phase separation curves and the freezing point curves.
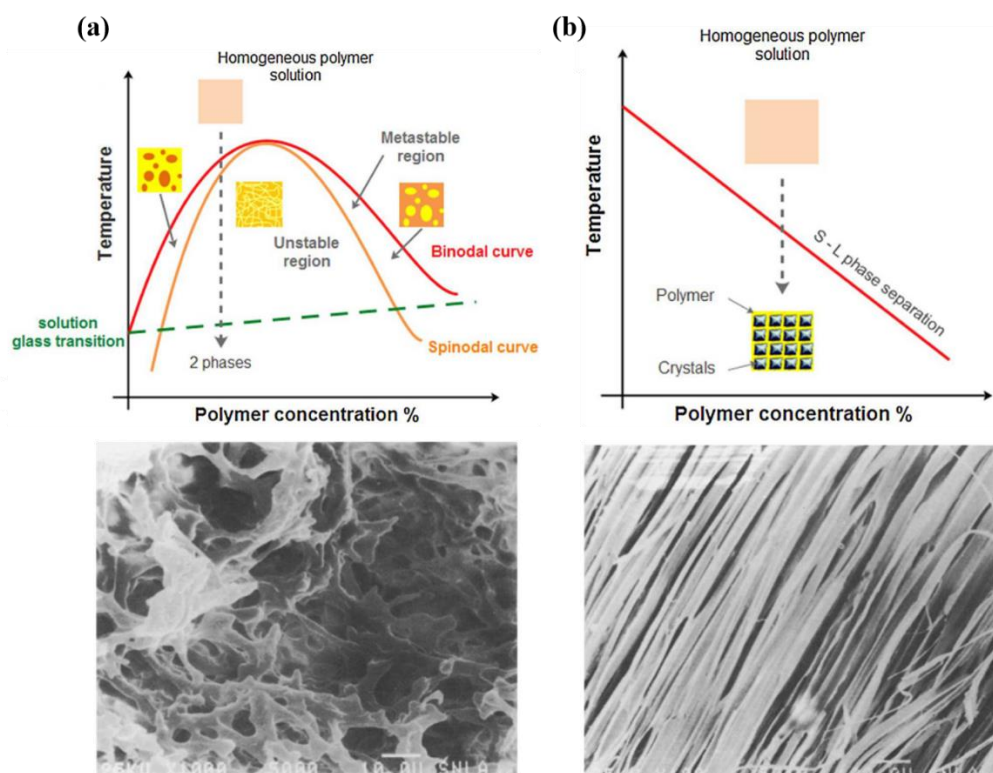
Figure 2.10 Schematic of phase diagram and resultant polymer morphology of (a) polystyrene and cyclohexane (b) polystyrene and benzene. Reprinted from [42, 43] with permission from Elsevier.

2.3 Applications of Freeze-cast Materials

Owing to the compatibility of freeze casting with a variety of material systems and its ability to tailor the resultant microstructures, freeze-cast materials have been employed in numerous applications, including thermal insulation [44,45], piezo-resistive sensors [46], sorption media for pollutant capture [47, 48], biomimetic scaffolds [49, 50], and energy conversion and storage [51, 52, 53]. This thesis will focus on applications in the field of energy storage, specifically in sodium ion batteries, and ceramic scaffolds.

2.3.1 Battery Separators

A battery separator, a thin porous membrane located between the electrodes as a physical barrier to prevent electrode contact and thus short circuit, must have no or very low chemical reactivity with other components of a battery. In addition, the thickness of a separator should be in the range of a few tens of micrometers; otherwise, the overall battery energy density will be compromised due to the reduced amount of active materials that can be placed in the restricted cell space in the presence of the separator [54]. A separator functions as an electrically insulating, electrolyte-infiltrated and ion-permeable membrane placed between the cathode and anode inside a battery. In order to facilitate the ion transport, a separator with a directionally aligned porous microstructure is highly sought-after. Freeze casting is advantageous in producing structures with directionally aligned pores due to its intrinsic thermal gradient. Besides the ability to create directionally aligned structures, freeze casting can also be integrated with tape casting to form the hybrid tape/freeze casting [34, 36], in which the final membrane thickness can be controlled during the tape casting step. Furthermore, tape/freeze casting is also a scalable processing technique which is advantageous for large-scale and continuous manufacturing. Polymer-based tape/freeze-cast separators will be discussed in detail in Chapters 3 and 4.

2.3.2 Ceramic Scaffolds

Scaffolds are structures that simultaneously provide mechanical support and transport characteristics. For freeze-cast ceramic scaffolds, the mechanical properties can be readily improved by reducing the porosity [2] or introducing reinforcements [55]. As for the transport properties, for example, permeability can be enhanced by increasing the pore size [2], further aligning the pore orientation [31], or transitioning to a more permeable pore morphology [2], as discussed in Chapter 5. Although mechanical properties and transport properties are two seemingly conflicting features, freeze casting offers the opportunity to increase mechanical properties without sacrificing much permeability [56].

Chapter 3

PVDF-HFP/AL$_2$O$_3$ COMPOSITE MEMBRANES

Material in this chapter is reproduced in part from "Tape/Freeze-cast PVDF-HFP/Al$_2$O$_3$ composite membranes for battery separators", C. Wu, X. Lin, A. Prabhakar, Z. Kelly, H. Liu, K.T. Faber; *Manuscript in preparation*. The work was done in collaboration with Xiaoping Lin, Abhinav Prabhakar, Zachary Kelly, Hansan Liu of Talos Tech LLC, and Katherine T. Faber. C. Wu fabricated and characterized PVDF-HFP/Al$_2$O$_3$ composite membranes using SEM and FTIR, their porosities, thermal stability, and mechanical properties, and wrote the manuscript. X. Lin, A. Prabhakar, and Z. Kelly measured contact angles and electrolyte uptake, and characterized electrochemical properties of the membranes. H. Liu and K.T. Faber supervised this work.

3.1 Introduction

As previously discussed in Section 2.3.1, the intrinsic thermal gradient involved in freeze casting makes it advantageous in producing directionally aligned pore structures, and thus freeze casting is a promising processing route to fabricate battery separators.

A critical portion of freeze casting is the freezing step which leads to the phase segregation between frozen solvent and rejected solute, since the resultant pore morphology is the replica of the frozen solvent. However, as mentioned in Section 2.2.2, in certain solutions, liquid-liquid phase separation (LLPS), phase separation of the solution into a polymer-rich phase and a polymer-lean phase, can take place before the freezing of the solvent when the temperature is lowered [42, 43]. In this case, the isotropic structure formed by the LLPS [42, 43] acts as a template for the subsequent freeze casting and determines the final microstructure, in contrast to the case in which the resultant structure is dominated by the directionally frozen solvent crystals. To verify that LLPS occurred prior to the freezing of the solvent, the freezing behavior of polymer solutions is visually inspected and attention is paid to whether cloudiness formation in solution, an indication of LLPS [42, 57], is observed.

Another important aspect of freeze casting is the nucleation of solvent crystals. During the freezing process in conventional unidirectional freeze casting, due to the absence of nucleation control, solvent crystal nuclei usually occur in a random manner. This leads to the formation of domains of crystals and the resulting pores with varied orientations [29], which severely hinders the fabrication of well-oriented structures on a large scale. As a result, the control over the nucleation process is of vital importance if highly oriented structures are envisioned [29, 58]. In this chapter, a bi-directional, air-wedge-assisted tape/freeze casting setup with dual thermal gradients as shown in Figure 3.1, is designed to control the nucleation process while producing membranes with directional pores.
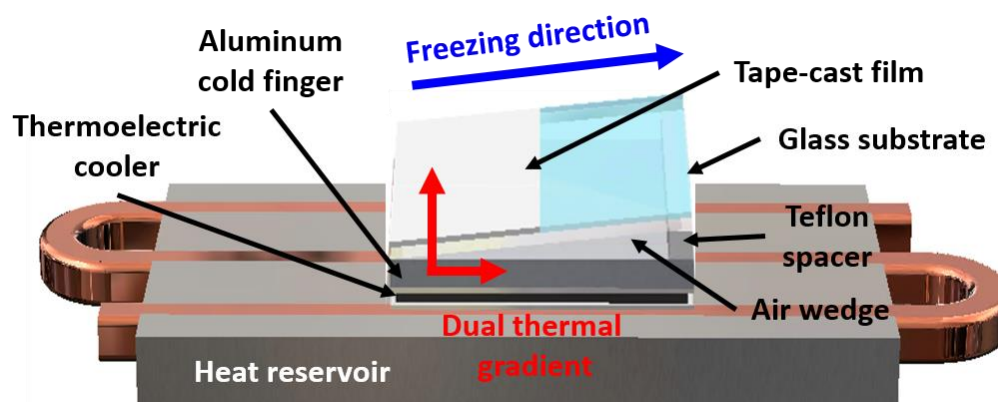
Figure 3.1 Schematic of experimental setup (not to scale) for bi-directional, air-wedge-assisted tape/freeze casting with dual thermal gradients.

Apart from the requirements of a separator provided in Section 2.3.1, other essential characteristics of a separator are compatibility with the electrolyte to reduce internal resistance, thermal stability to ensure cell safety, and sufficient mechanical robustness to withstand stresses during cell assembly and operation. In order to improve the abovementioned features of separators, reinforcements have been integrated into separators, including polymer blends [59, 60], cellulose [61, 62, 63, 64], and oxides [65, 66, 67, 68, 69]. Amongst the reinforcing elements, oxides are particularly attractive due to their enhanced chemical and thermal stability compared to the polymeric reinforcing elements. However,

the majority of studies on oxide-reinforced separators either adopt additional coating processes or chemical conversion reactions [65, 66, 67, 68, 69], which increase not only the separator thickness but also the complexity of processing. In contrast, in this chapter, alumina fillers are introduced through a facile ball milling procedure to form suspensions with the solvent prior to mixing with the polymer followed by tape/freeze casting. PVDF-HFP, known for its chemical inertness, is a candidate material to fabricate separators.

In this chapter, the freezing behavior of a PVDF-HFP/dioxane bulk solution is first examined to ensure the absence of liquid-liquid phase separation prior to the freezing of the solvent. The nature of dual thermal gradients in the bi-directional, air-wedge-assisted tape/freeze casting is realized by monitoring the temperature of different regions on the tape casting substrate. Subsequently, the freezing behavior of PVDF-HFP/dioxane solution and PVDF-HFP/dioxane/alumina suspension in thin films are explored to establish the relationship between the freezing behavior and the resultant microstructures. Further, the microstructure, phase composition, thermal stability, mechanical, and electrochemical properties of the tape/freeze-cast separators are appraised to establish the efficacy of composite membranes for separators in sodium ion batteries.

3.2 Experimental Methods

3.2.1 Materials

Poly(vinylidene fluoride-co-hexafluoropropylene) (PVDF-HFP, M_w = 400,000 g/mol, Sigma-Aldrich, St. Louis, MO, USA) and 1,4-dioxane (anhydrous, 99.8%, Sigma-Aldrich) were used to produce solutions for observation of the freezing behavior in thin films and fabrication of separators via tape/freeze casting. Dioxane was chosen as the solvent for PVDF-HFP according to the solubility parameters of dioxane and PVDF determined from the solubility tests performed by Bottino et al. [70]. In the 3D Hansen solubility space discussed in Chapter 2, dioxane was found to be located on the surface of the solubility sphere of PVDF, which indicates that dioxane is considered a good solvent for PVDF and a candidate solvent for PVDF-HFP. Nano-sized alumina powder (γ-phase, < 50nm, Sigma-Aldrich) was added to the above solutions to form suspensions and acted as ceramic filler

reinforcements to produce the composite membranes. Celgard separator (Celgard® 2500, Celgard LLC, Charlotte, NC, USA) and filter paper (Whatman® filter paper) were used as references for tape/freeze cast membranes. An organic electrolyte consisted of 1 M $NaClO_4$ (Sigma-Aldrich) in the mixture of propylene carbonate (Sigma-Aldrich) and ethylene carbonate (Sigma-Aldrich) (1:1, volume ratio). Ionic liquid electrolyte (Solvionic, Toulouse, France) was composed of NaFSI:PYR13 FSI (1:9, molar ratio). All chemicals were used without further purification or treatment.

A $Na_3V_2(PO_4)_3$/$NaTi_2(PO_4)_3$ full cell (NVP/NTP) was selected as the assessment model cell for the separators due to its favorable stability among all the SIB electrode couple [71, 72]. This SIB couple eliminates the concerns of solid electrolyte interphase (SEI) formation and electrolyte oxidization [73] and provides a more reliable comparison among separators. The $Na_3V_2(PO_4)_3$ and $NaTi_2(PO_4)_3$ electrode materials were laboratory-produced by solid-state sintering. The cathode and anode electrodes were prepared by a traditional doctor-blade casting process with a ratio of active material/carbon black/binder (PVDF) of 85:10:5 (wt%).

3.2.2 Freezing Point Measurement

The freezing points of pure dioxane and PVDF-HFP/dioxane solutions with different polymer concentrations were determined by visual inspection. Mixtures of 7, 15, 20 wt% PVDF-HFP with corresponding 73, 85, 80 wt% dioxane were heated in glass vials in a water bath at 70 °C under constant stirring with magnetic stir bars until clear and homogeneous solutions were obtained. A fixed volume of 20 μL of each polymer solution and pure dioxane was pipetted onto a freeze casting setup. This setup consisted of an Al cold finger on top of a thermoelectric plate which was placed on top of a heat reservoir connected to a circulating refrigerated silicone oil bath (FP50-ME, Julabo USA Inc., Allentown, PA, USA). The thermoelectric plate was connected to a PID controller which also recorded temperature profiles. Once the polymer solution and pure dioxane was placed on top of the Al cold finger, a microscope cover slip was immediately covered to minimize solvent evaporation and moisture absorption. A petri dish was placed over the setup to prevent condensation and reduce ambient air flow. The freezing point, T_f, was recorded as the temperature at which the

first observed nucleation, perceived by an abrupt increase in solution opacity, took place at a cooling rate of 1 °C/min. Five samples were tested for each solution and their average values with standard deviation were reported.

3.2.3 Freezing Behavior of Bulk Solutions

A mixture of 15 wt% PVDF-HFP with 85 wt% dioxane was heated in a glass vial in a water bath at 70 °C under continuous stirring with a magnetic stir bar until a clear and homogeneous solution was produced. The PVDF-HFP/dioxane solution was poured into a cylindrical glass mold (h = 20 mm, $\varnothing$ = 25 mm with 1.6 mm walls); the base of the mold was sealed with Mylar film and vacuum grease to prevent leakage. The glass mold was then placed on top of an Al cold finger whose temperature was programmed to decrease from room temperature to -25 °C at a ramp rate of 10 °C/min by a thermoelectric with a PID controller. The glass mold was capped with a glass plate to prevent solvent evaporation. The freezing behavior of the PVDF-HFP/dioxane solution was recorded using a camera.

3.2.4 Evaluation of Dual Thermal Gradients via Substrate Temperature Monitoring

Dual thermal gradients were confirmed by monitoring the temperature of different regions on the glass substrate used for tape casting without tape-cast solution films, as illustrated in Figure 3.2. Temperature was monitored using five type K thermocouples equally spaced at 9 mm intervals along the length of the top surface of a glass substrate (75 x 50 x 1 mm^3) from the leading edge of the substrate in the freezing direction (Figure 3.2 (a) and (b)). Once the temperature of the aluminum cold finger (50 x 50 mm^2) regulated by a thermoelectric with a PID controller reached -25 °C, a Teflon spacer (50 x 10 x 1 mm^3) was placed on the far end of the cold finger. The glass substrate monitored by the five thermocouples was positioned on the Teflon spacer, which created an air wedge below the glass substrate, as illustrated in Figure 3.2 (b). Besides the thermal gradient in the z direction, this air wedge was intended to produce a second thermal gradient in the x direction during freezing. Temperature recording at 1-s intervals was initiated as soon as the glass substrate made contact with the aluminum cold finger and the Teflon spacer.
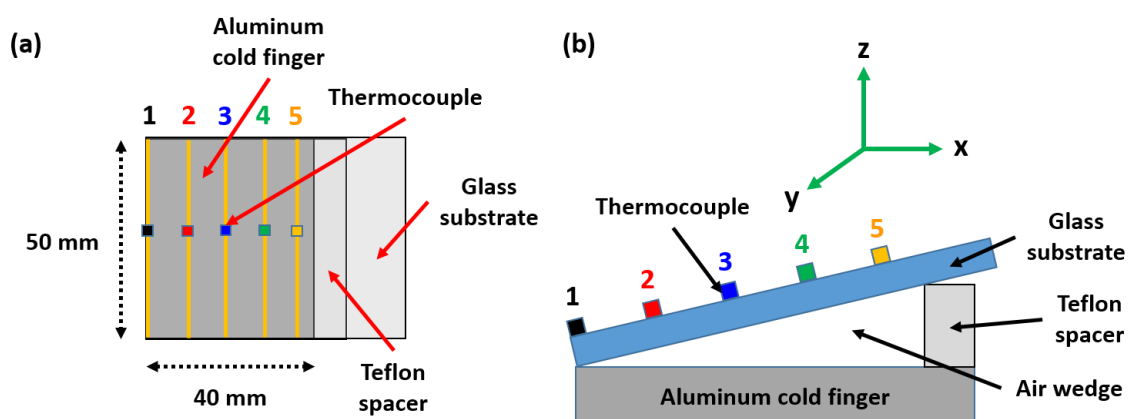
Figure 3.2 Schematic of (a) top view and (b) orthogonal view of experimental setup (not to scale) for temperature monitoring on glass substrate. Number indicates the thermocouple channel ID and colored squares indicate the tips of thermocouples on the top surface of the glass substrate.

3.2.5 Membrane Preparation and Freezing Behavior of Thin Films
3.2.5.1 PVDF-HFP/Dioxane Solution

A mixture of 15 wt% PVDF-HFP with 85 wt% dioxane was heated in a glass vial in a water bath at 70 ^{o}C under continuous stirring with a magnetic stir bar until a clear and homogeneous solution was produced. Approximately 3 to 4 mL of the solution was pipetted onto a glass substrate (75 x 50 x 1 mm^3) and then tape cast using a doctor blade with a clearance of 200 μm. The tape-cast film was transferred to the aluminum cold finger set at -25 ^{o}C on the freeze-casting apparatus shown schematically in Figure 3.1. As described above, two thermal gradients were present, as induced by the air wedge beneath the glass substrate due to the inserted spacer. A glass petri dish was placed over the glass substrate to minimize solvent evaporation. The freezing process of the tape-cast film was recorded by a camera and the freezing front velocities were determined by subsequent image analyses (ImageJ, National Institutes of Health). Once the tape-cast film was completely frozen, the frozen film atop the glass substrate was placed into a freeze dryer (VirTis AdVantage 2.0, SP Scientific,

Warminster, PA, USA) set at -40 ºC and 500 µbar for 48 h. After complete removal of dioxane, a dry and porous PVDF-HFP membrane was obtained.

3.2.5.2 PVDF-HFP/Dioxane/Alumina Suspensions

Suspensions composed of dioxane and alumina contents of 1.73, 2.58, and 3.41 wt% with respect to dioxane were prepared via ball milling for 24 h. Pre-determined amounts of PVDF-HFP were added to the above suspensions in order to obtain a fixed concentration of 15 wt% PVDF-HFP with respect to dioxane and alumina contents of 7, 10, and 15 wt%. The alumina/dioxane suspensions and PVDF-HFP were heated in vials in a water bath at 70 ºC under continuous stirring until all of the PVDF-HFP was dissolved and stable polymer-solvent-ceramic suspensions resulted. The tape/freeze casting steps for the PVDF-HFP/Al_2O_3 composite membranes were identical to the steps described in Section 3.2.4.1.

3.2.6 Membrane Physical Characterization
3.2.6.1 Microstructure and FTIR

Membranes were first examined by scanning electron microscopy (FESEM, ZEISS 1550 VP, Jena, Germany). SEM sample cross-section preparation required cryogenic fracture in a liquid nitrogen bath (below the glass transition temperature of PVDF-HFP) with a pre-chilled razor blade to avoid soft membrane deformation at ambient temperatures. The membranes were then coated with Pt prior to SEM examination. X-ray energy dispersive spectroscopy (EDS) was used to observe the distribution of added alumina in carbon-coated composite membranes. Attenuated total reflection Fourier-transform infrared spectroscopy (ATR-FTIR, Nicolet iS50, ThermoFisher Scientific, Waltham, MA, USA) was used to characterize the phase compositions of the membranes with a resolution of 4 cm^{-1} in a wavenumber range from 4000 to 400 cm^{-1}.

3.2.6.2 Porosity, Mechanical Properties and Thermal Stability

Membrane porosity was determined by the Archimedes' method, using ethanol as the immersion fluid [74]. Membranes were soaked in ethanol for 24 h before measuring the wet membrane weight. Each membrane was measured 5 times and the average value was

reported. Mechanical properties including tensile strength, Young's modulus and strain-to-failure of membranes were determined using a universal testing machine (Instron 5982, Norwood, MA, USA) following ASTM-D882 standards with a strain rate of 0.1 min^{-1}. Three membranes were tested for each condition and the average was reported. The thermal stability of membranes was assessed by the area change after placing 10 x 10 mm^2 membrane sections in aluminum weight boats inside a convection oven set at temperatures ranging from 75 to 135 ºC for 30 minutes.

3.2.6.3 Contact Angle and Electrolyte Uptake

The wettability of membranes in two electrolytes (organic electrolyte and ionic liquid) was evaluated in terms of contact angle and electrolyte uptake (EU). Contact angles were measured by a computer-controlled goniometer (Ossila, Sheffield, United Kingdom). The droplets were applied from a syringe with a fixed volume of 10 μL. The contact angle was defined as the angle between a droplet and the surface of a separator measured 5 seconds after the droplet reached the surface of the separator. Electrolyte uptake was established from the difference in weight before and after soaking the membrane in a specific electrolyte for 4 h, and values were normalized by the initial weight [75].

3.2.7 Electrochemical Performance Evaluation

3.2.7.1 Ionic Conductivity and MacMullin Number

Ionic conductivity was measured using electrochemical impedance spectroscopy (EIS) in a Solartron 1287 potentiostat and 1260 frequency response analyzer (AMETEK Inc., Berwyn, PA, USA). The separator was first soaked with 50 μL of electrolyte and placed between two stainless steel spacers and then sealed in a CR2032 coin cell. The ionic conductivity was calculated from

$$\text{Ionic conductivity (mS/cm)} = 1/\text{resistivity} = L / (Z \times A) \tag{3.1}$$

where L is the ion transfer path between the two stainless steel spacers, i.e., the separator thickness, A is the cross-sectional area, and Z is the measured resistance or impedance. The permeability of the separators was reported from the MacMullin number, defined as the ratio of ionic conductivity without a separator to that with a separator. The ionic conductivity of

pure electrolytes was measured using a testing configuration in which a PTFE O-ring was sandwiched between two stainless steel (SS) plates to hold the electrolyte in the void.

3.2.7.2 Cell Performance

CR2032 coin cells were used to assess the electrochemical performance of the membranes. The NTP anode capacity was designed to be 10% greater than the counterpart NVP cathode capacity such that the cell capacity was limited by the NVP cathode. Doctor-bladed cathode (NVP) and anode (NTP) were punched into discs, and a coin cell was assembled by sandwiching the electrolyte-soaked membrane between the cathode and anode. Rate performance tests were conducted at 0.5C, 1C, 2C, and 5C for 5 cycles for each C rate.

3.3 Results and Discussion

3.3.1 Freezing Point Measurement

The freezing points of PVDF-HFP/dioxane solutions as a function of polymer concentration are shown in Figure 3.3. A decreasing trend in solution freezing point with increasing polymer content, also known as freezing point depression, is observed. It is found that the solution with 15 wt% PVDF-HFP which is used to fabricate PVDF-HFP membranes shows a freezing point around -1.5 °C.
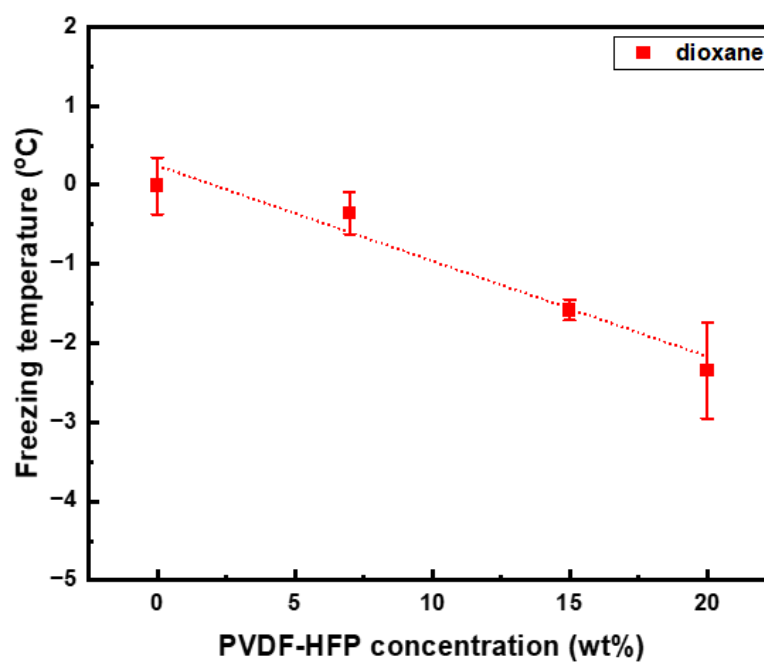
Figure 3.3 Freezing point of PVDF-HFP/dioxane solutions as a function of polymer concentration.

3.3.2 Freezing Behavior of Bulk Solution

Figure 3.4 shows photo images of the freezing behavior of PVDF-HFP/dioxane bulk solution. It is clear that no cloudiness formation is observed prior to the freezing of the solvent, which indicates that the liquid-liquid phase separation does not precede the freezing of dioxane. Therefore, the microstructure produced by this particular system can be attributed to the frozen dioxane crystals. The freezing behavior of PVDF-HFP/dioxane solution in the bulk form can be extended to that of the thin film form.
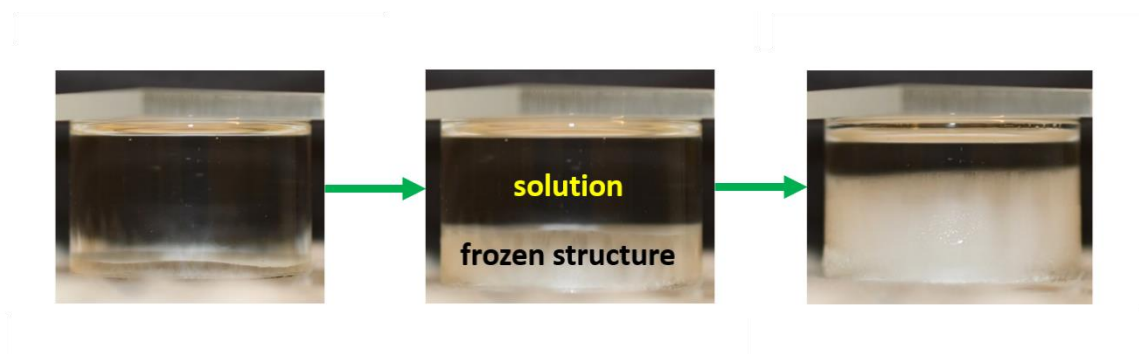
Figure 3.4 Photo images of freezing behavior of PVDF-HFP/dioxane solution showing growth of frozen solvent crystals. Arrows indicate the chronological order.

3.3.3 Dual Thermal Gradients in Bi-directional, Air-wedge-assisted Freezing

Before studying the freezing behavior of solutions and suspensions in thin films, it is crucial to understand the two thermal gradients associated with the experimental setup used to carry out the freeze-casting process (Figure 3.1). Due to the low temperature of the Al cold finger (-25 °C), a thermal gradient in the z direction is always present. The effectiveness of the insulating air wedge created by the Teflon spacer to produce a thermal gradient in the x direction is evidenced by the temperature evolution curves shown in Figure 3.5. First, the cooling rate is found to decrease when travelling from channel 1 (black) to channel 5 (orange) due to the increase in thickness of the air wedge. Second, because of the increasing insulating capacity with air wedge thickness, a rising steady-state temperature profile is seen when migrating from channel 1 (-18 °C) to channel 5 (-8 °C), establishing a thermal gradient in the x direction. The above results confirm the existence of dual thermal gradients in the

tape/freeze casting setup shown in Figure 3.1. Moreover, with the temperature evolution curves, the time required to reach the freezing point of the solution (-1.5 °C, for 15 wt% PVDF-HFP), at each position on the glass substrate can be estimated. These times are approximately 8, 18, 33, 51, and 57 seconds for the positions corresponding to thermocouple channels 1, 2, 3, 4, and 5, respectively, as indicated by the colored vertical dashed lines.
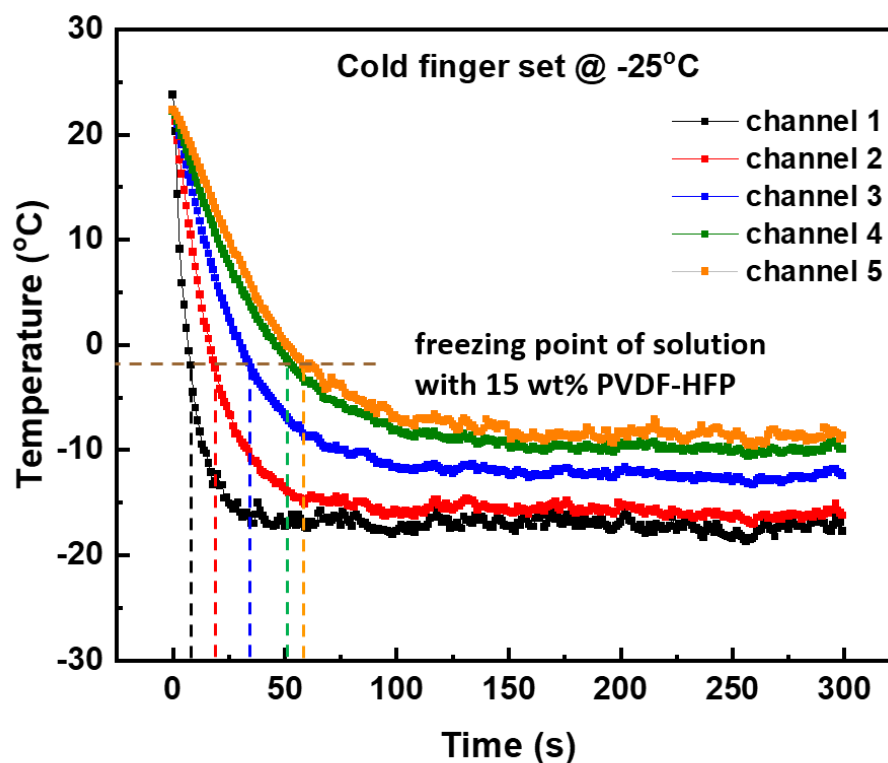
Figure 3.5 Temperature evolution with time along glass substrate measured following the experimental setup shown in Figure 3.2 (a) and (b). Colored, vertical dashed lines indicate the estimated time required for each thermocouple to reach the freezing point of the solution containing 15 wt% PVDF-HFP.

3.3.4 Effects of Alumina on Freezing Behavior of Solution in Thin Films and Membrane Microstructures

The air wedge is found to be effective in controlling the freezing of the tape-cast films. This is verified from the snapshots from the freezing video of 15 wt% PVDF-HFP/dioxane solution and 15 wt% PVDF-HFP/dioxane/alumina suspension given in Figure 3.6 (a) and (b). The freezing of the tape-cast film starts left-to-right where the glass substrate has direct contact with the aluminum cold finger, i.e., where the air wedge thickness = 0. This observation also reveals the insulating ability of the air wedge. As freezing progresses, not only are two flat freezing fronts observed but they are also found to travel at relatively constant velocities determined from a series of snapshots with results plotted in Figure 3.6 (c). The first freezing front is a direct result of the freezing of dioxane molecules in the solution, while the second has been hypothesized by Kim and Lee [76] to be associated with the crystallization of dioxane molecules occurring in the PVDF-HFP-rich phase (cryo-concentrated regions) that formed during the first freezing front. A higher degree of opacity in the tape-cast film is seen after the passage of the second freezing front. Furthermore, the estimated time at each thermocouple position to reach the -1.5 °C freezing point from Figure 3.5 can be translated to the freezing front velocity plot in Figure 3.6 (c). It is found that, except for the position of the first thermocouple, the first freezing front arrives at the positions of the other four thermocouples before the temperatures reach -1.5 °C. This is why multiple nucleation events across the glass substrate are not observed due to the presence of the air wedge.

While comparing the freezing process of the solution and alumina-containing suspension, despite its slightly higher freezing front velocities, likely due to the higher thermal conductivity of the dispersed alumina particles [77, 78], little or no difference in the freezing behavior and freezing front morphology is found. This indicates that the added alumina has a negligible effect on the freezing behavior of the solution.
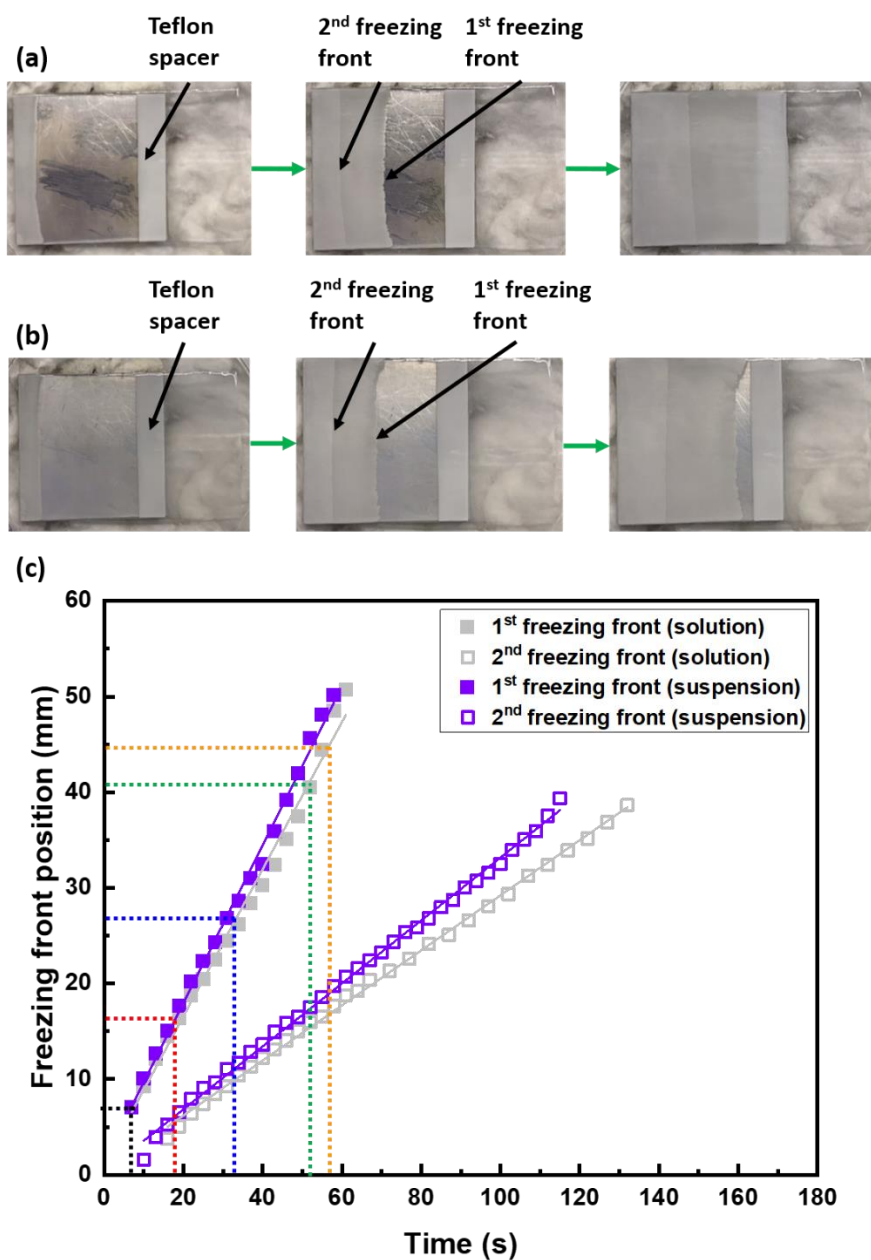
Figure 3.6 Snapshots of the freezing video of tape-cast film of (a) 15 wt% PVDF-HFP/dioxane solution (b) 15 wt% PVDF-HFP/dioxane/alumina suspension both showing two controlled freezing fronts from left to right (arrows indicate the chronological order during freezing). (c) freezing front velocities obtained from videos of (a) and (b). All four lines show r^2 values exceeding 0.99. Colored vertical dashed lines are translated from Figure 3.5, and the horizontal dashed lines indicate the corresponding freezing front positions.

Microstructures of the PVDF-HFP polymer membrane and PVDF-HFP/Al$_2$O$_3$ composite membranes are presented in Figure 3.7. Here, the cold face refers to the surface of the membrane that was closer to the cold finger and had direct contact with the glass substrate, while the hot face was exposed to the atmosphere. On the membranes' cold faces (Figure 3.7 (a), (d), (g), (j)), aligned dendritic pore structures are observed in all membranes, regardless of the alumina content. The dendritic pore structure arises from the crystallization of dioxane [36, 79]. The alignment of pore arrays is attributed to the horizontal thermal gradient due to the air wedge. On the hot faces of the membranes (Figure 3.7 (b), (e), (h), (k)), the alignment of pore arrays is also noted. The pore morphology difference between the cold face and the hot face lies in the fact that the pores on the cold face are caused by the dioxane nucleation while the pores on the hot face are a result of competitive growth of dioxane crystals through the thickness. It is also noteworthy that the pore size on the hot face is found to be larger than that on the cold face, as the freezing front velocity decreases with distance from the cold face.

The role of a separator is to not only prevent physical contact between the electrodes but also allow the transport of working ions, and thus the microstructure cross-section of a separator is a critical factor. Though-thickness cross-sections (Figure 3.7 (c), (f), (i), (l)) of all materials studied, regardless of the alumina content, demonstrate directionally aligned and dendritic pore structures. The alignment of pores in the thickness direction is a direct result of the vertical thermal gradient during the freeze casting process [36, 76]. The similarity in microstructures between the polymer and composite membranes provides another indicator that the alumina, regardless of amount, has negligible effects on the crystallization behavior of the dioxane molecules during freeze casting.
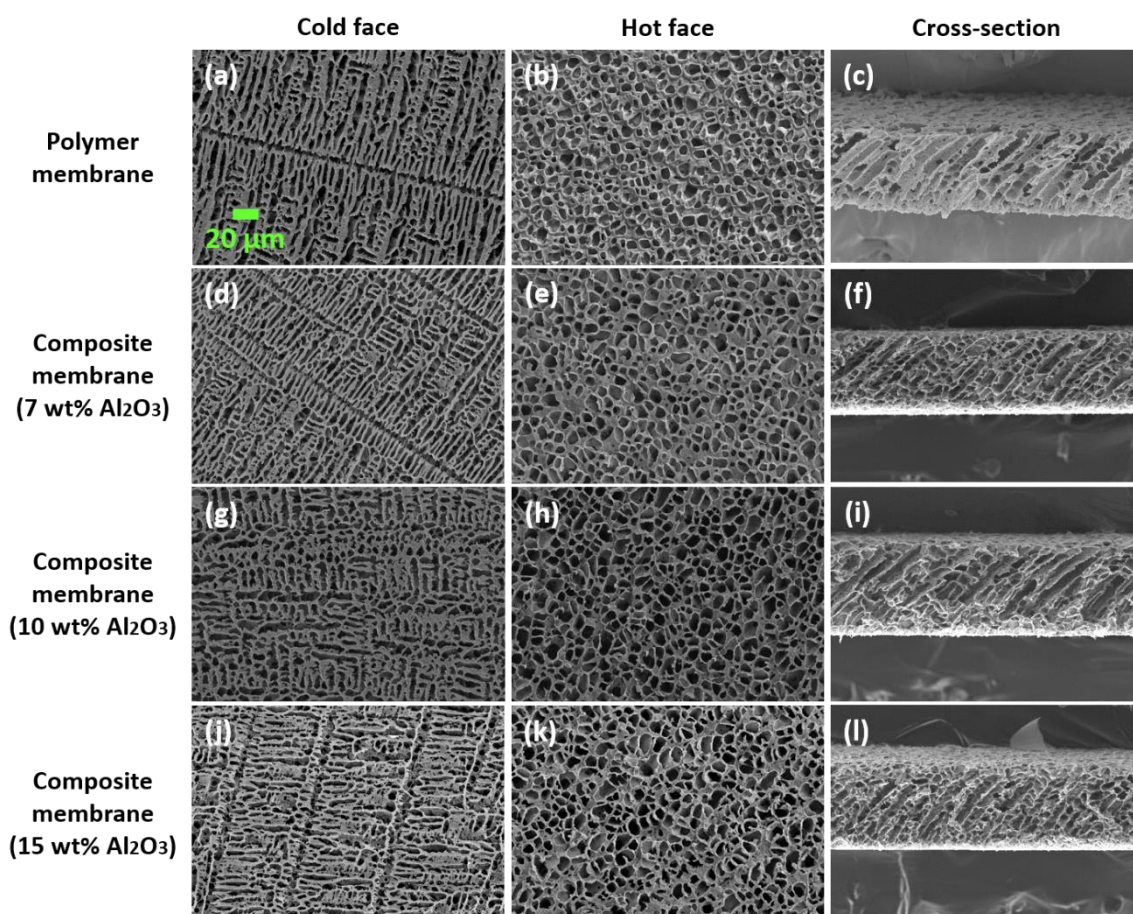
Figure 3.7 Micrographs of polymer membrane (a) cold face (b) hot face (c) cross-section; composite membrane with 7 wt% Al_2O_3 (d) cold face (e) hot face (f) cross-section; with 10 wt% Al_2O_3 (g) cold face (h) hot face (i) cross-section; with 15 wt% Al_2O_3 (j) cold face (k) hot face (l) cross-section (all micrographs share the same scale bar.)

To assess the distribution of alumina in the composite membranes, cross-sectional micrographs and corresponding aluminum EDS mapping of the composite membranes containing 7, 10, and 15 wt% Al_2O_3 are shown in Figure 3.8 (a) through Figure 3.8 (f). Although the Al EDS mapping results (Figure 3.8 (d), (e), and (f)) confirm the incorporation of Al_2O_3 into the PVDF-HFP membranes, the distribution of Al_2O_3 is non-uniform across the cross-sections with Al_2O_3 agglomerates detected as clusters in the mapping. Furthermore,

at higher magnifications, Al_2O_3 agglomerates are visible and highlighted by red circles on the cold face (Figure 3.8 (g)), the hot face (Figure 3.8 (h)), and the cross-section (Figure 3.8 (i)) of the composite membrane with 15 wt% Al_2O_3. The presence of Al_2O_3 agglomerates in the composite membranes indicates that agglomeration either occurs in the process of casting suspension preparation or forms during freezing. Due to the difference in timescale between suspension preparation (1 to 2 hours) and freezing (1 to 2 minutes), most of the Al_2O_3 agglomerates are more likely to form during the suspension preparation step.
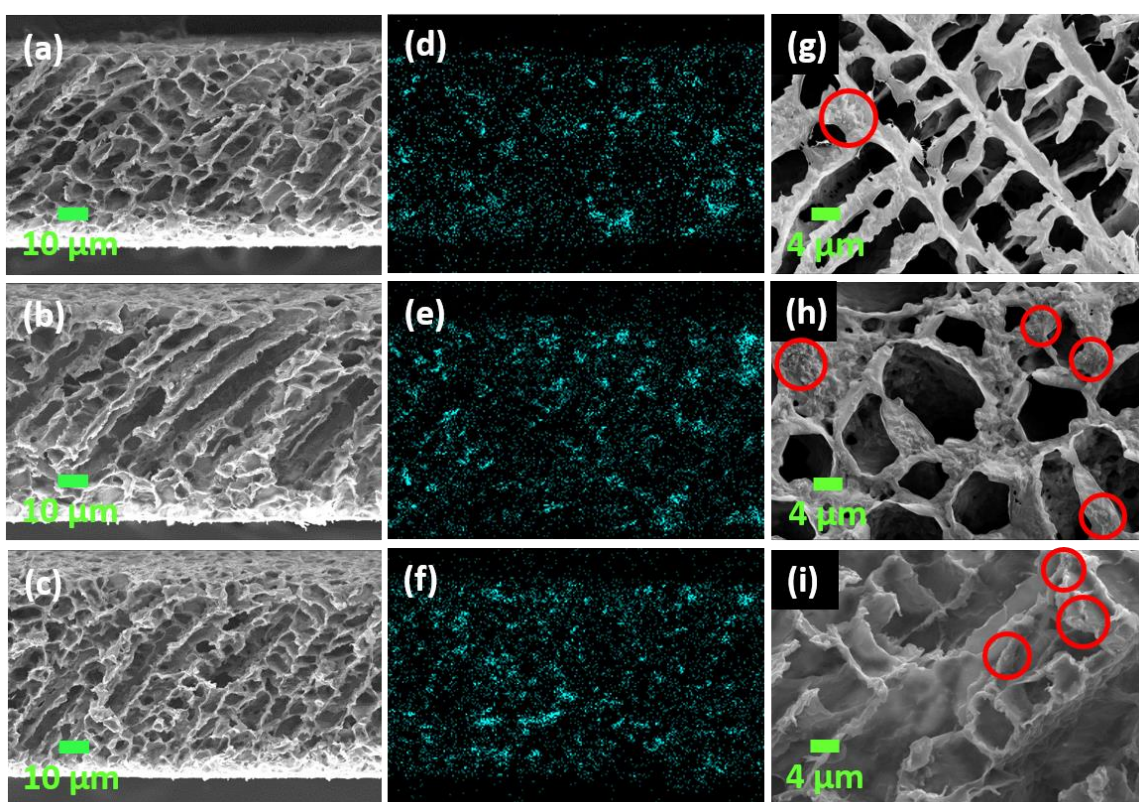
Figure 3.8 Cross-sectional micrographs and corresponding Al EDS mapping results of composite membranes with (a),(d) 7 wt% Al_2O_3 (b),(e) 10 wt% Al_2O_3 (c),(f) 15 wt% Al_2O_3; composite membrane with 15 wt% Al_2O_3 at higher magnifications showing Al_2O_3 agglomerates (highlighted by red circles) on (g) cold face (h) hot face (i) cross-section.

3.3.5 Physical Characterization of Polymer and Composite Membranes

3.3.5.1 Phase Composition from FTIR Spectra

FTIR spectra of the polymer and composite membranes on both cold and hot faces are shown in Figure 3.9 with the as-received PVDF-HFP solids as a reference. In the two upper figures, the absorption peak around 1617 cm^{-1} in all composite membranes and the broad absorption band around 3447 cm^{-1} in the composite membrane with 15 wt% Al_2O_3 are associated with the bending and stretching vibrations of the hydroxyl group of adsorbed water molecules [80, 81], respectively. The presence of these peaks indicates the incorporation of Al_2O_3 into the composite membranes, while these peaks are not observed in the polymer membrane or the as-received PVDF-HFP solids.

In the two lower figures, while comparing the as-received PVDF-HFP solids with the polymer membrane, a noteworthy difference is in the relative intensity of absorption bands. The bands around 840 and 1275 cm^{-1} associated with the β phase of the PVDF segment [82] are more prominent in the as-received solids than the membrane, while the band around 1209 cm^{-1} related to the α phase of the PVDF segment [82] is more prominent in the membrane than the as-received solids. According to Nishiyama et al. [83], the tendency to form the non-polar α phase (TGTG') of PVDF is observed when PVDF is dissolved in solvents with low dipole moments, such as dioxane (dipole moment = 2.55D) [84] in the current case. Owing to the interaction between dioxane and PVDF, the PVDF chains tend to form into the unexpanded conformation, which then results in the α phase.

While comparing the spectra collected from the two faces of all membranes, it is found that there is little difference in characteristic peaks, which indicates the uniformity in phases in each membrane. Moreover, it is noted that all three composite membranes along with the polymer membrane present characteristic peaks associated with the α and β phase of the PVDF segment around 614, 763, and 1275 cm^{-1} [82], respectively. More importantly, the resemblance between the spectra of the composite membranes and that of the polymer membrane indicates that the added alumina content has no significant effects on the PVDF-HHP phases present in the membranes.
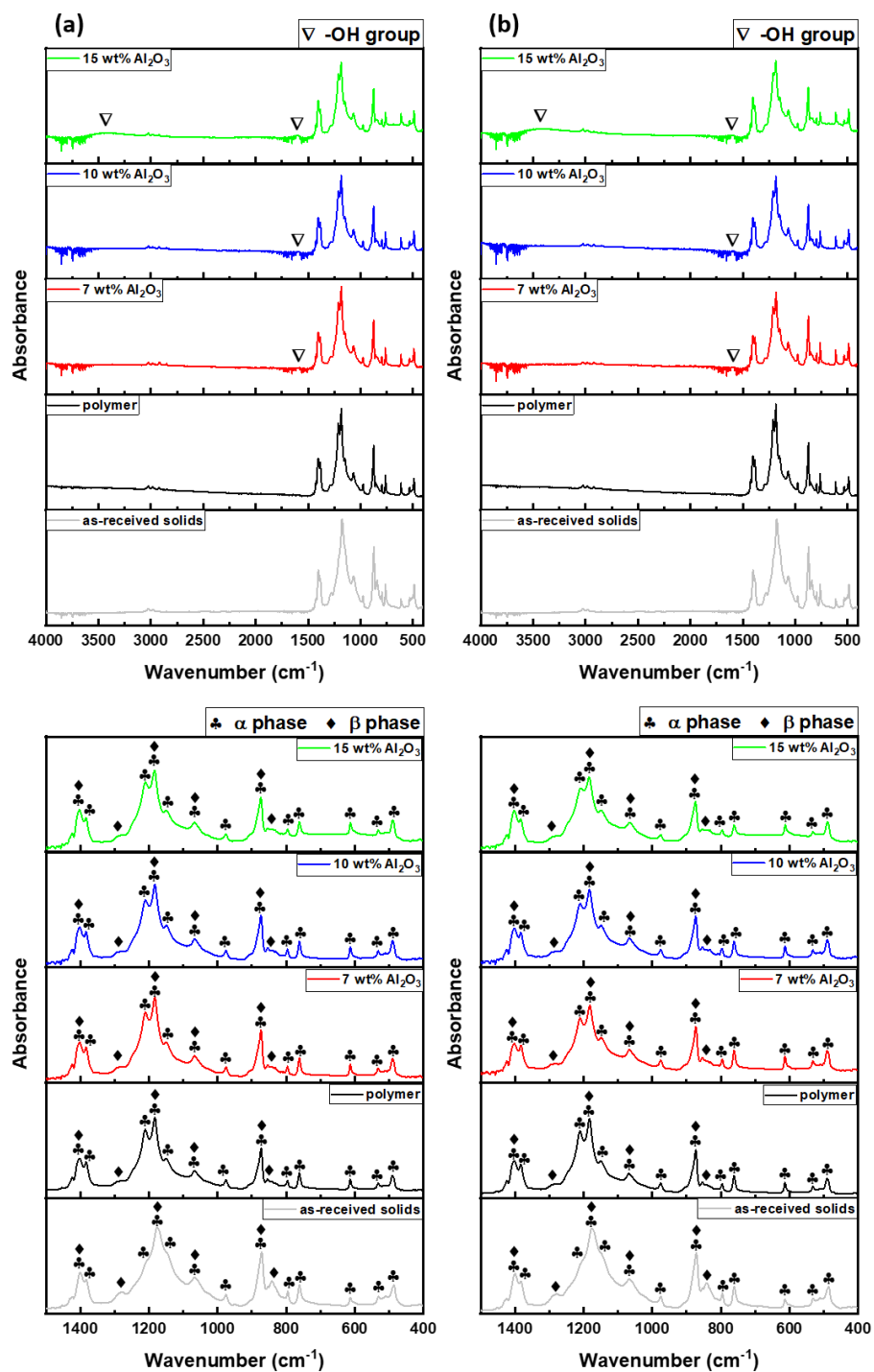
Figure 3.9 FTIR spectra of polymer and composite membranes on (a) cold face and (b) hot face (upper figures: full spectra range, lower figures: expanded view of the fingerprint region).

3.3.5.2 Porosity, Mechanical Properties and Thermal Stability

Porosity and mechanical properties including Young's modulus, tensile strength, and strain-to-failure of the polymer and composite membranes are tabulated in Table 3.1. For all of the membranes studied, the measured porosities are above 85% and in good agreement with the calculated porosities based upon the compositions of the casting solution and suspensions. This further confirms that the removal of dioxane is complete during the freeze-drying process.

In terms of mechanical properties, when alumina is introduced into the polymer membrane, a two-fold increase in Young's modulus is found (> 30 MPa vs. ~ 15 MPa). Given the similar porosities and microstructures between the polymer and composite membranes, the enhancement in Young's modulus is ascribed to the added alumina particles (Young's modulus ~ 400 GPa) which serve as stiffening inclusions [85, 86] in the PVDF-HFP matrix. By applying the general rule of mixture [87] to the Young's modulus while treating the polymer membrane as the reference, the calculated Young's modulus for the composite membranes containing 7, 10, and 15 wt% Al_2O_3 are 1.17, 1.65, and 2.49 GPa, respectively, which are two orders of magnitude greater than the measured values in Table 3.1. A proposed reason for such Young's modulus values is the agglomeration of alumina particles (micrographs in Figure 3.7 (g), (h), and (i)) which effectively reduces the reinforcement/matrix interfacial area through which the applied load can be transferred to the reinforcement agents [88]. In addition, agglomerates can lead to detachment of the reinforcement from the matrix, which also results in a decrease in reinforcement effects.

Although an increasing trend in tensile strength is observed with alumina content, with a 20% increase found while comparing the polymer membrane with the 15wt% Al_2O_3 composite membrane, this strengthening effect is not considered obvious since the alumina additions are too low to compensate for the high porosity of the membranes (> 85%). Another contributing factor to the low tensile strengths of all membranes is the direction in which the tensile loads are applied. The loads are applied in the direction perpendicular to the membrane thickness, a weaker direction given the through-thickness microstructures of

membranes observed in Figure 3.6 and 3.7. Kalnaus et al. [89] and Shen et al. [90] have shown that microstructure anisotropy in porous polymer membranes is an important factor responsible for lower tensile strengths in weaker directions such as the transverse direction. A reduction in strain-to-failure is observed with the addition of Al_2O_3 to the polymer membrane. Yan et al. [91] have suggested that this is due to the decline of membrane elasticity caused by the Al_2O_3 particles.

Table 3.1 Porosity, Young's modulus, tensile strength, and strain-to-failure of polymer and composite membranes. Porosity values in parentheses are calculated based on compositions of casting solution and suspensions.

Al_2O_3 content in membrane (wt %)	Porosity (%)	Young's modulus (MPa)	Tensile strength (MPa)	Strain-to-failure (%)
0 wt% (polymer)	88.77 (90.68)	15.52 ± 4.32	1.20 ± 0.03	63.32 ± 11.80
7 wt%	87.73 (89.21)	31.58 ± 5.66	1.35 ± 0.03	48.36 ± 10.04
10 wt%	87.20 (88.59)	33.57 ± 5.94	1.42 ± 0.07	46.02 ± 9.62
15 wt%	86.58 (88.49)	34.99 ± 5.19	1.45 ± 0.09	43.82 ± 12.15

Separators need to be dimensionally stable during battery operation to prevent contact between electrodes and ensure safety, and thus, an investigation of thermal stability of separators is imperative. Area change of a membrane after a heat treatment is used as an indicator of its thermal stability. The area changes of the polymer and composite membranes after a 30-minute heat treatment at temperatures ranging from 75 to 135 °C are plotted in Figure 3.10. Regardless of membrane type, the degree of thermal shrinkage of membranes is found to increase with increasing heat treatment temperature. The slightly positive values of area change found in the cases of composite membranes with 10 wt% and 15wt% Al_2O_3 are within the experimental measurement error. More importantly, it is noted that the composite membranes exhibit less thermal shrinkage compared to the polymer counterpart in the temperature range studied, from 75 to 135 °C. Among the composite membranes, the

membrane with 15 wt% Al_2O_3 exhibits the least shrinkage, less than 2%, in the high-temperature range from 105 to 135 ℃. Given that the porosities and pore morphologies of the polymer and composite membranes are similar, the enhanced thermal stability (less thermal shrinkage) is attributed to the interaction between the polymer chains and the heat-resistant Al_2O_3 particles which provide thermal stability to the PVDF-HFP matrix against thermal shrinkage [92].
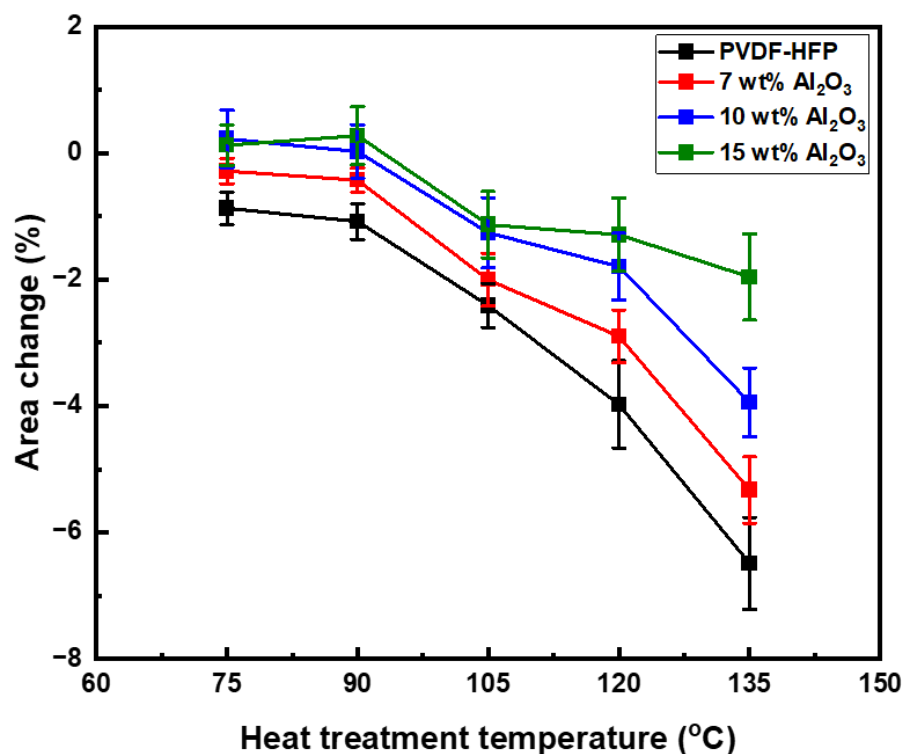
Figure 3.10 Area changes of polymer and composite membranes as a function of heat treatment temperature. Negative values indicate shrinkage.

3.3.5.3 Contact Angles and Electrolyte Uptake

Wettability of an electrolyte with a separator is a key factor that determines the performance of a battery, since a wetted separator offers better contact with the electrodes, and hence, leads to enhanced ionic conductivity. Contact angles of organic electrolyte and ionic liquid on the polymer and composite separators along with Celgard 2500 as a reference are shown in Figure 3.11. It is clear that both electrolytes show smaller contact angles on all of the tape/freeze-cast membranes compared to Celgard, which indicates greater wettability of electrolytes with PVDF-HFP-based membranes than with Celgard. The poor wettability of Celgard is due to its low porosity (~ 55%) and hydrophobic nature of polyolefin.

In both cases of organic electrolyte and ionic liquid, when alumina is introduced to the polymer membrane, no regular pattern in contact angle is observed. This irregularity may be caused by two reasons: (1) presence of Al_2O_3 agglomerates that reduce the effective interface between Al_2O_3 surface and electrolytes, and (2) uneven distribution of Al_2O_3 on membrane surfaces.

Separator / Electrolyte	Celgard 2500	PVDF-HFP	7 wt% Al_2O_3	10 wt% Al_2O_3	15 wt% Al_2O_3
Organic electrolyte	53°	26°	43°	34°	39°
Ionic liquid	73°	45°	53°	46°	51°
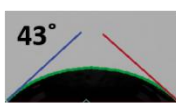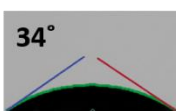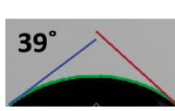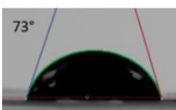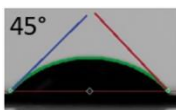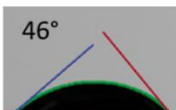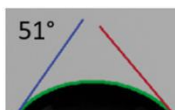
Figure 3.11 Contact angles of organic electrolyte and ionic liquid on polymer and composite membranes with Celgard 2500 as a reference.

Electrolyte uptake, a critical characteristic of a separator that markedly influences ionic conductivity and cell performance, is used to gauge the electrolyte retention capacity of a membrane. Electrolyte uptake values of the polymer and composite membranes in both organic electrolyte and ionic liquid with Celgard 2500 and filter paper as references are plotted in Figure 3.12. It is clear that all of the tape/freeze-cast membranes exhibit higher uptake values in both electrolytes in comparison with filter paper and Celgard. The low uptake values of Celgard in both electrolytes suggest low porosity (~ 55%) and poor wettability due to the polyolefin hydrophobic nature of Celgard. Therefore, Celgard is excluded from further electrochemical assessments.

It is noteworthy that with the introduction of alumina into the polymer membrane, an approximately 60% and 150% increase in uptake value is found in the case of the organic electrolyte and ionic liquid, respectively. Given the similar porosity values amongst all of the tape/freeze-cast membranes, it is reasonable to attribute the improvement in electrolyte uptake to the added alumina in the composite membranes. Despite Al_2O_3 agglomerates, the Al_2O_3 particles in the bulk of the composite membranes are known to increase the affinity between the electrolytes and membranes [93]. Another likely reason for the increase in electrolyte uptake seen in the composite membranes is due to the reduction in crystallinity in PVDF-HFP matrix caused by the added alumina [94], and thus more amorphous phase with higher electrolyte retention capacity is formed. The organization of polymer chains may be hindered by the interaction between the Lewis acid groups on the Al_2O_3 surface (–OH) and the polar CF_2 groups on the PVDF-HFP polymer chains [95], which leads to a decrease in the degree of crystallinity of polymer matrix. Even though the effect of added alumina is not obvious in terms of contact angles of electrolytes on the composite membranes, the added alumina proves to be beneficial in increasing the electrolyte uptake values in both organic electrolyte and ionic liquid.
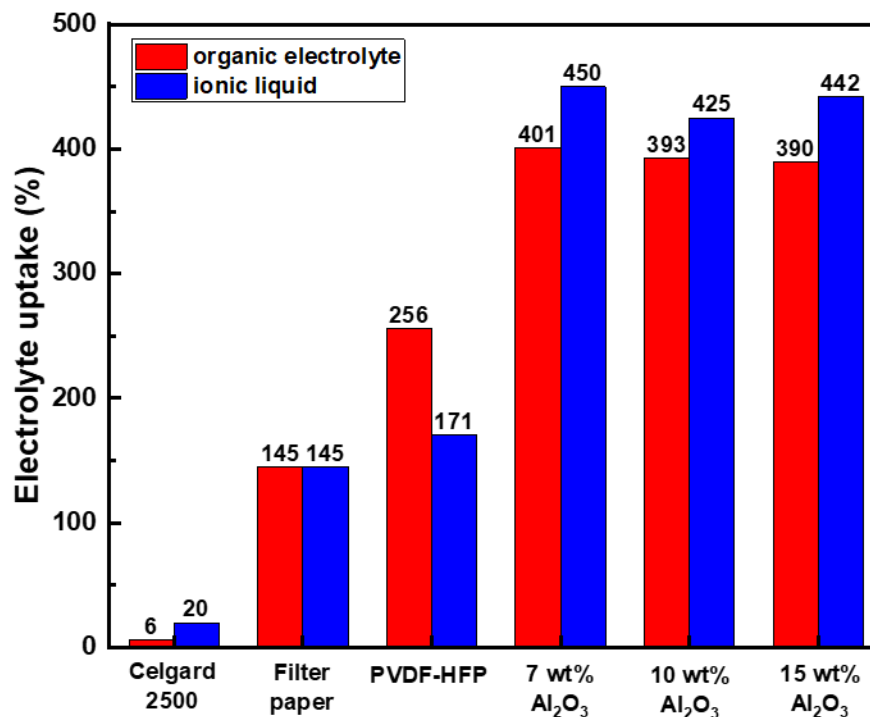
Figure 3.12 Electrolyte uptakes of polymer and composite membranes in organic electrolyte and ionic liquid with Celgard 2500 and filter paper as references.

3.3.6 Electrochemical Performance

3.3.6.1 Ionic Conductivity and MacMullin Number

It is well known that high ionic conductivity is a key factor to achieve high performance in batteries. Ionic conductivity values of the polymer and composite membranes in both the organic electrolyte and ionic liquid with filter paper as a reference are tabulated in Table 3.2. All of the tape/freeze-cast membranes exhibit higher ionic conductivities than the filter paper in both electrolytes, while the composite membranes show slightly higher ionic conductivities than their polymer counterpart. Specifically, the composite membrane with 7

wt% Al_2O_3 delivering the highest ionic conductivities of 1.6 mS/cm and 1.7 mS/cm in organic electrolyte and ionic liquid, respectively.

In comparison with filter paper, the higher ionic conductivities of the tape/freeze-cast membranes are attributed to greater electrolyte uptake reported in Figure 3.11. Apart from the higher degrees of electrolyte uptake, the promoted electrolyte dissociation caused by the Lewis acid-base interaction between the acidic Al_2O_3 surfaces (–OH) and the electrolyte anions [96, 97] is also responsible for the improved ionic conductivities in the composite membranes compared to their polymer counterpart. The absence of an increasing trend in ionic conductivity with added alumina content can be ascribed to the presence of alumina agglomerates which lowers the effective surface area.

The MacMullin number (N_m) is a figure of merit for battery separators which quantifies the decrease in the effective conductivity in the presence of a separator. MacMullin numbers of all of the PVDF-HFP-based membranes in both the organic electrolyte and ionic liquid with filter paper as a reference are also tabulated in Table 3.2. A desired inverted trend against ionic conductivity is observed in MacMullin number, with the lowest values of 6.1 and 3.8 found in the composite membrane with 7 wt% Al_2O_3 in the organic electrolyte and ionic liquid, respectively.

Table 3.2 Ionic conductivity and MacMullin number of polymer and composite membranes in organic electrolyte and ionic liquid with filter paper as a reference.

Al_2O_3 content in membrane (wt %)	Ionic conductivity in organic electrolyte (mS/cm)	Ionic conductivity in ionic liquid (mS/cm)	MacMullin number in organic electrolyte	MacMullin number in ionic liquid
Filter paper (reference)	0.7	0.6	14.9	10.3
0 wt% (polymer)	1.1	0.8	8.7	7.8
7 wt%	1.6	1.7	6.1	3.8
10 wt%	1.4	1.3	7.0	5.0
15 wt%	1.3	1.2	7.5	5.4

3.3.6.2 Charge-discharge Curves and Rate Performance in Coin Cells

Figure 3.13 displays the charge-discharge curves and rate performance of coin cells assembled with filter papers and tape/freeze-cast polymer membranes in both organic electrolyte and ionic liquid. In the case of the organic electrolyte (Figure 3.13 (a)), both cells show well-defined and stable charge-discharge plateaus, while the cell with tape/freeze-cast membrane (lower figure in Figure 3.13 (a)) exhibits better rate performance and lower capacity degradation per cycle than the cell with filter paper (upper figure in Figure 3.13 (a)). Furthermore, when charge rate is changed from 0.5C (black lines) to 5C (green lines), the cell with tape/freeze-cast polymer membrane shows a capacity retention of 81%, compared to a capacity retention of 72% in the filter paper-based cell. The superior rate performance of the PVDF-HFP membrane-based cell is attributed to the greater ionic conductivity due to the higher electrolyte uptake compared to the filter paper-based cell [98].

In the case of the ionic liquid (Figure 3.13 (b)), the cell with filter paper (upper figure in Figure 3.13 (b)) degrades rapidly every cycle and is not able to maintain stable cycling, which has been attributed to the reaction between the filter paper and ionic liquid by Salama et al. [99] and Fukaya et al. [100]. In contrast, the PVDF-HFP membrane-based cell (lower figure in Figure 3.13 (b)) is found to deliver improved rate performance and cycling stability, which is credited to the chemical inertness of PVDF-HFP with respect to the ionic liquid and the greater ionic conductivity of the PVDF-HFP membrane in contrast to filter paper. While comparing the two electrolytes, the higher viscosity and ionic resistivity of the ionic liquid than those of the organic electrolyte results in higher capacity retention in the organic electrolyte (Figure 3.13 (a)) than in the ionic liquid-based cells (Figure 3.13 (b)).
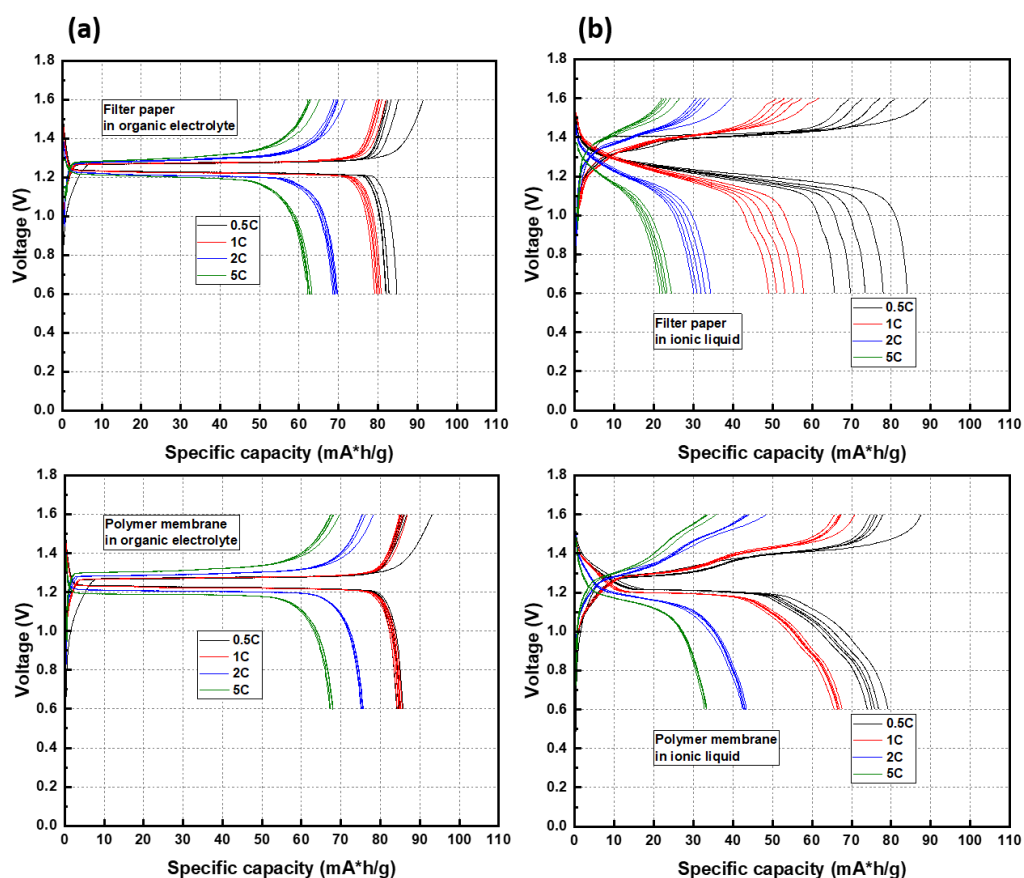
Figure 3.13 Charge-discharge curves and rate performance of coin cells using (a) organic electrolyte (b) ionic liquid. (upper figures: filter papers, lower figures: tape/freeze-cast polymer membranes).

The charge-discharge curves and rate performance of coin cells assembled with tape/freeze-cast composite membranes in both the organic electrolyte and ionic liquid are presented in Figure 3.14. In the case of the organic electrolyte, the cells assembled with the composite membranes (Figure 3.14 (a)) show higher initial capacities than the polymer membrane-based cell (lower figure in Figure 3.13 (a)), but little improvement is observed in capacity retention or rate performance. Some likely reasons associated with Al_2O_3 agglomerates are (1) uneven ion distribution on the separator, and (2) introduction of moisture to react with the electrolyte. On the other hand, when ionic liquid is used as the electrolyte (Figure 3.14

(b)), the cells with composite membranes deliver lower polarization, better rate performance and cycling stability than the polymer membrane-based cell (lower figure in Figure 3.13 (b)). Amongst the composite membrane-based cells, it is found that the cell assembled with the composite membrane with 7 wt% Al_2O_3 exhibits the best performance, in accordance with the highest ionic conductivity (Table 3.2) due to the greatest electrolyte uptake (Figure 3.12). The improved ionic conductivity due to the increased electrolyte uptake is thought to be responsible for the above enhancement in rate performance and cycling stability, which demonstrates the benefits of introducing Al_2O_3 fillers into polymer membranes.
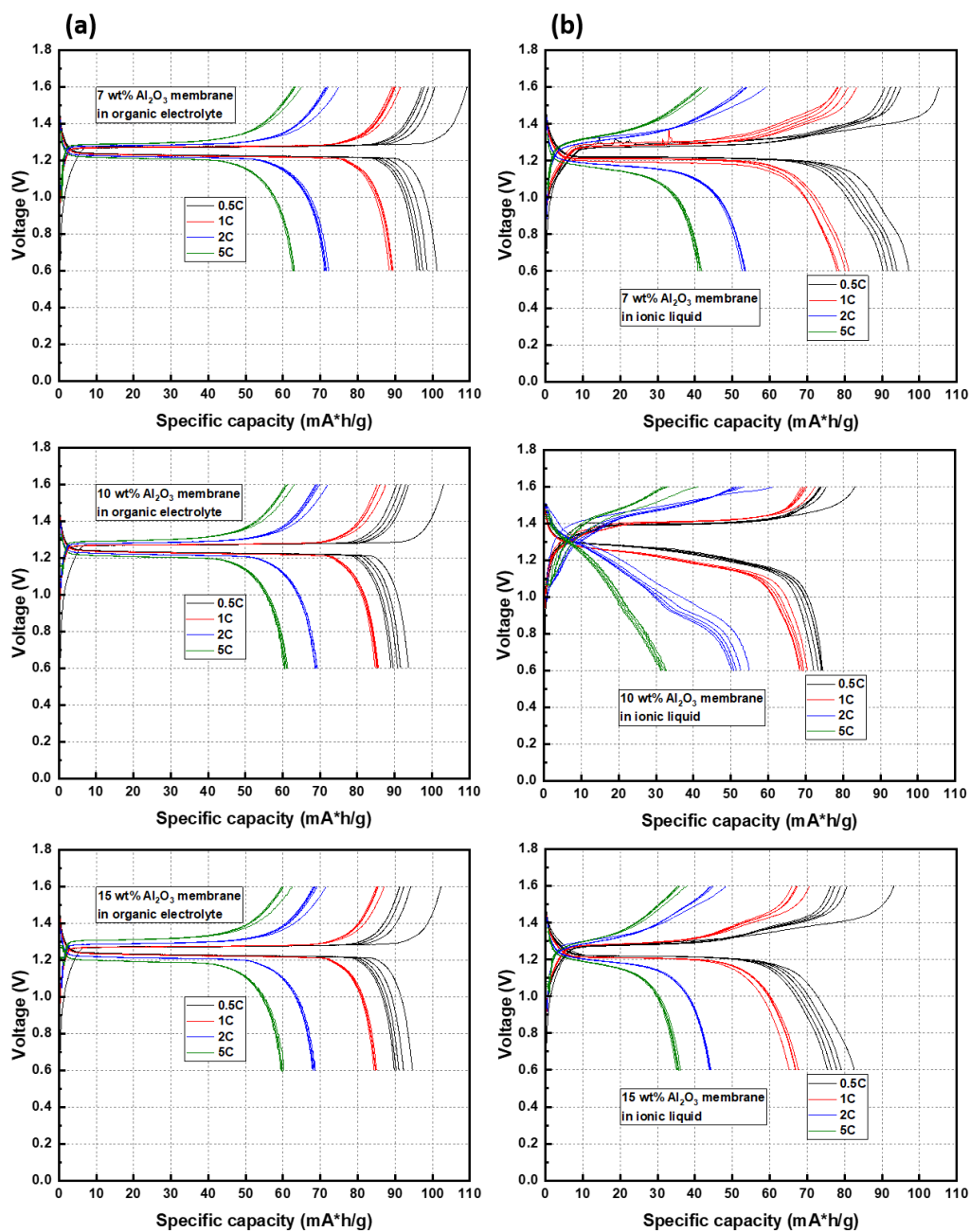
Figure 3.14 Charge-discharge curves and rate performance of coin cells using (a) organic electrolyte (b) ionic liquid. (upper figures: composite membranes with 7 wt% Al₂O₃, center figures: composite membranes 10wt% Al₂O₃, lower figures: composite membranes with 15 wt% Al₂O₃).

3.4 Conclusions

The effects of alumina on microstructure, phase composition, and thermal, mechanical and electrochemical properties of the tape/freeze-cast PVDF-HFP membranes have been studied. With the bi-directional, air-wedge-assisted freezing configuration, controlled freezing of dioxane is observed, and a through-thickness, directionally aligned, and dendritic porous structure is obtained. No significant difference is found in the freezing behavior with the introduction of alumina to form suspensions. With the addition of alumina confirmed by EDS, the porosity, microstructure, and phase composition of the tape/freeze-cast membranes remain largely unchanged, indicating that the amount of added alumina has insignificant impact on the crystallization of dioxane during freeze casting. Despite the presence of alumina agglomerates in the composite membranes, the enhancement in thermal stability, and improvement in elastic modulus as well as electrolyte uptake and ionic conductivity of the membranes can attributed to the incorporated alumina. In terms of electrochemical performance, cells with composite membranes as separators deliver better rate performance and cycling stability than those with membranes solely made of PVDF-HFP polymers and filter papers, providing a more promising class of separators than conventional polyolefin and filter paper separators for sodium-ion batteries.

C h a p t e r   4

PVDF-HFP/SIO$_2$ COMPOSITE MEMBRANES

Material in this chapter is reproduced in part from "PVDF-HFP/SiO$_2$ composite membranes for separators in Na-ion batteries", C. Wu, X. Lin, A. Prabhakar, Z. Kelly, H. Liu, K.T. Faber; *Manuscript in preparation*. The work was done in collaboration with Xiaoping Lin, Abhinav Prabhakar, Zachary Kelly, Hansan Liu of Talos Tech LLC, and Katherine T. Faber. C. Wu fabricated and characterized PVDF-HFP/SiO$_2$ composite membranes using SEM, FTIR, and TGA, their porosities and mechanical responses, and wrote the manuscript. X. Lin, A. Prabhakar, and Z. Kelly measured contact angles and electrolyte uptake, and characterized electrochemical properties of the membranes. H. Liu and K.T. Faber supervised this work.

4.1 Introduction

In Chapter 3, composite PVDF-HFP/Al$_2$O$_3$ membranes fabricated via tape/freeze casting were described and the added alumina was found to reinforce the polymer membranes in terms of thermal stability, elastic modulus, electrolyte uptake, and cell performance. However, in order to produce oxide-reinforced membranes with high uniformity via tape/freeze casting, preparation of stable and well-dispersed suspensions is a must.

While He et al. [101] and Li et al. [102] introduce SiO$_2$ and TiO$_2$ into PVDF-HFP separators with TEOS and Ti(OC$_4$H$_9$)$_4$ via *in-situ* sol-gel reactions, with a combined process of evaporation followed by phase inversion, the desirable aligned porous structure is not present in their separators. In contrast, in this chapter, PVDF-HFP separators are produced via freeze casting to create directionally aligned pore morphology.

In this chapter, PVDF-HFP/DMSO and PVDF-HFP/DMSO/TEOS solutions are used to fabricate pristine PVDF-HFP and composite PVDF-HFP/SiO$_2$ membranes via tape/freeze casting and ensuing sol-gel reaction. The effects of TEOS and the resulting silica on

microstructure, phase composition, thermal stability, mechanical properties, and electrolyte affinity of membranes are investigated. More importantly, the electrochemical properties of the membranes assembled in coin cells are evaluated to demonstrate the effectiveness of composite membranes as SIB separators.

4.2 Experimental Procedures

4.2.1 Materials

Poly(vinylidene fluoride-co-hexafluoropropylene) (PVDF-HFP, M_w = 400,000 g/mol, Sigma Aldrich, St. Louis, MO, USA) and dimethyl sulfoxide (DMSO, EMPLURA®, EMD Millipore Corporation, Billerica, MA, USA) were used to produce solutions and fabricate separators via tape/freeze casting. DMSO was selected as the solvent for PVDF-HFP according to their respective solubility parameters plotted in the 3D Hansen solubility space in Figure 4.1. As discussed in Chapter 2, solute-solvent compatibility can be assessed by the distance between the corresponding pair in the 3D Hansen solubility space. A shorter distance indicates greater compatibility between the solute and solvent and vice versa. It can be seen that the distance between PVDF-HFP and DMSO is shorter than that between PVDF-HFP and dioxane, suggesting DMSO has a greater compatibility with PVDF-HFP compared to dioxane. Tetraethoxysilane (TEOS, Sigma Aldrich) was selected as the co-solvent and the precursor of silica. Ethanol (Sigma Aldrich) and ammonium hydroxide solution (28 – 30 wt% $NH_3 \cdot H_2O$, Sigma Aldrich) were mixed to create the sol-gel bath for TEOS sol-gel reaction. Celgard separator (Celgard® 2500, Celgard LLC, Charlotte, NC, USA) and filter paper (Whatman® filter paper) were chosen as references for tape/freeze-cast separators. An organic electrolyte was comprised of 1 M $NaClO_4$ (Sigma-Aldrich) in the mixture of propylene carbonate (Sigma-Aldrich) and ethylene carbonate (Sigma-Aldrich) (1:1, vol/vol). Ionic liquid electrolyte (Solvionic, Toulouse, France) consisted of NaFSI:PYR13 FSI (1:9, molar ratio). All chemicals were used without further purification or treatment.
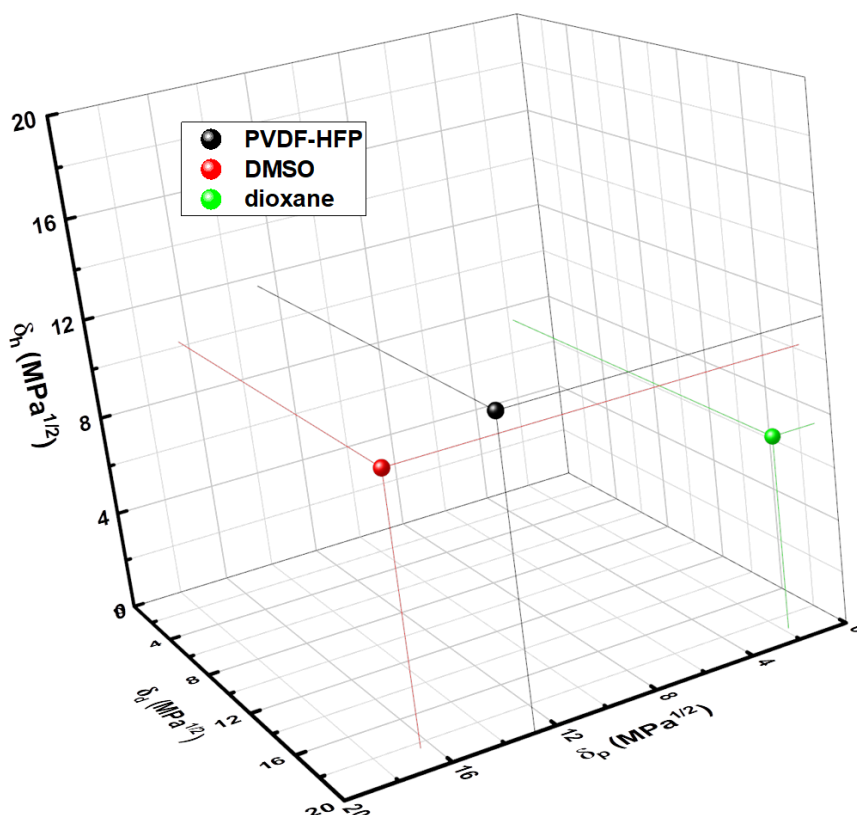
Figure 4.1 Solubility parameters of PVDF-HFP, DMSO, and dioxane plotted in the 3D Hansen solubility space.

A $Na_3V_2(PO_4)_3/NaTi_2(PO_4)_3$ full cell (NVP/NTP) was selected as the assessment model cell for the separators due to its excellent stability among all the SIB electrode couples [71, 72]. This SIB couple eliminates the concerns of solid electrolyte interphase (SEI) formation and electrolyte oxidization [73] and provides a reliable comparison among separators. The $Na_3V_2(PO_4)_3$ and $NaTi_2(PO_4)_3$ electrode materials were laboratory-produced by solid-state sintering. The cathode and anode electrodes were prepared by a traditional doctor-blade casting process with a ratio of active material/carbon black/binder (PVDF) of 85:10:5 (wt%).

4.2.2 Freezing Behavior in PVDF-HFP/DMSO & PVDF-HFP/DMSO/TEOS Solutions

Mixtures of 20 wt% PVDF-HFP with 80, 72, and 64 wt% DMSO were heated in glass vials in a 70 °C oil bath under constant stirring with magnetic stir bars until clear and homogeneous solutions resulted. Respective amounts of 8 and 16 wt% of TEOS were then added to the solutions with 72 and 64 wt% DMSO under continuous stirring until clear and homogeneous solutions were obtained. The three solutions with different DMSO/TEOS ratios were transferred to a cold room set at 4 °C and the freezing behavior of the three solutions was recorded using a camera.

4.2.3 Membrane Preparation

4.2.3.1 PVDF-HFP/DMSO Solution

A mixture of 20 wt% PVDF-HFP with 80 wt% DMSO was heated in a glass vial in an oil bath at 70 °C under constant stirring with a magnetic stir bar until a clear and homogeneous solution was produced. Approximately 3 to 4 mL of the solution was poured onto an Al substrate and then tape-cast using a doctor blade with a clearance with 200 μm. The Al substrate was then placed in contact with an Al stage pre-chilled with liquid nitrogen (LN_2). Once the tape-cast film was completely frozen, the frozen film with the Al substrate were immersed in a 4 °C-water bath for solvent extraction. After complete removal of DMSO, which was determined by full penetration of water into the film and detachment from the Al substrate, a wet, porous PVDF-HFP membrane was rinsed with deionized water and ethanol and dried at RT for 24 h.

4.2.3.2 PVDF-HFP/DMSO/TEOS Solutions

Mixtures of 20 wt% PVDF-HFP with 72 and 64 wt% DMSO were heated in glass vials in a 70 °C oil bath until clear and homogeneous solutions resulted. Respective amounts of 8 and 16 wt% of TEOS were then added to the above solutions under continuous stirring until clear and homogeneous solutions were obtained. The following steps including tape casting, freezing, and solvent extraction were identical to the previous section. Once DMSO was removed from the membranes, the wet, porous PVDF-HFP membranes were then soaked in

a sol-gel bath consisting of a mixture of ethanol and ammonium hydroxide (C_2H_5OH/$NH_3 \cdot H_2O$/TEOS = 40/2/1, vol/vol/vol) for 12 h to carry out the sol-gel reaction. This was followed by a deionized water and ethanol rinse to remove residual solvent and drying at RT for 24 h. For simplicity, the polymer membrane made without TEOS is denoted as PH20D80, while the composite membranes made with DMSO/TEOS ratios of 72/8 and 64/16 are denoted as PH20D72T8 and PH20D64T16, respectively.

4.2.4 Membrane Physical Characterization

4.2.4.1 Microstructure and FTIR

Microstructures of membranes were examined by scanning electron microscopy (FESEM, ZEISS 1550 VP, Jena, Germany). Sample cross-section preparation required cryogenic fracture in a liquid nitrogen bath (below the glass transition temperature of PVDF-HFP) with a pre-chilled razor blade to avoid soft membrane deformation at ambient temperatures. The membranes were then coated with Pt prior to SEM examination. X-ray energy dispersive spectroscopy (EDS) was used to observe the distribution of added silica in carbon-coated composite membranes. Attenuated total reflection Fourier-transform infrared spectroscopy (ATR-FTIR, Nicolet iS50, ThermoFisher Scientific, Waltham, MA, USA) was used to characterize the phase compositions of the membranes and assess the incorporation of silica in a wavenumber range from 4000 to 400 cm^{-1} with a resolution of 4 cm^{-1}.

4.2.4.2 Porosity, Mechanical Properties and Thermal Stability

Membrane porosity, the pore volume relative to the total volume of the membrane, was determined by the Archimedes' method using ethanol as the immersion fluid and following the equation below [74],

$$\varepsilon = \frac{\frac{W_w - W_d}{\rho_e}}{\frac{W_w - W_d}{\rho_e} + \frac{W_d}{\rho_p}} \tag{4.1}$$

where W_w and W_d are the weights of wet and dry membrane, and ρ_e and ρ_p are the densities of ethanol and polymer. Membranes were soaked in ethanol for 24 h before measuring the wet membrane weight. Each membrane was measured 5 times and the average value was reported. Mechanical properties including tensile strength, Young's modulus, and strain-to-

failure of membranes were determined using a universal testing machine (Instron 5982, Norwood, MA, USA) following ASTM-D882 with a strain rate set at 0.1 min^{-1}. Five membranes were tested for each condition and the average was reported. The thermal stability of membranes was assessed by thermogravimetric analysis (TGA, TGA 550, TA Instruments, New Castle, DE, USA) at a ramp rate of 5 ^{o}C/min from RT to 1000 ^{o}C under ambient atmosphere.

4.2.4.3 Contact Angle and Electrolyte Uptake

The affinity of membranes with the organic and ionic liquid electrolytes was evaluated by contact angle and electrolyte uptake (EU). Contact angles were measured by a computer-controlled goniometer (Ossila, Sheffield, United Kingdom). The droplets were applied from a syringe with a fixed volume of 10 μL. The contact angle was defined as the angle between a droplet and the surface of a separator measured 5 seconds after the droplet reached the surface of the separator. Electrolyte uptake (EU) was established from the difference in weight before and after soaking in a specific electrolyte for 4 h, and normalized by the initial weight following the equation below [75],

$$EU = \frac{M - M_0}{M_0} \tag{4.2}$$

where M and M_0 are the weights of membrane after and before soaking in electrolytes.

4.2.5 Electrochemical Performance Evaluation

4.2.5.1 Ionic Conductivity and MacMullin Number

Ionic conductivity was measured by electrochemical impedance spectroscopy (EIS) using GAMRY Interface 1010E (GAMRY Instruments, Philadelphia, PA, USA) in the frequency range from 100 to 2 x 10^6 Hz at an amplitude of 10 mV. The ionic conductivity of the pure electrolyte was measured in a cell with a configuration of an O-ring with electrolyte mounted between two stainless steel (SS) disks. For the ionic conductivity of the separator, the O-ring with electrolyte was replaced with the separator soaked in the electrolyte in the above configuration. The ionic conductivity was calculated from the equation below,

$$Ionic\ conductivity\ (mS/cm) = 1/resistivity = L\ /\ (Z\ x\ A) \tag{4.3}$$

where L is the ion transfer path between the two stainless steel spacers, i.e., the separator or O-ring thickness, A is the cross-sectional area, and Z is the measured resistance or impedance. The permeability of separators was characterized by the MacMullin number (N_m), which is calculated based upon the ratio of ionic conductivity of pure electrolyte to that of a separator soaked with electrolyte.

4.2.5.2 Cell Performance

CR2032 coin cells were used to evaluate the electrochemical performance of membranes. Doctor-bladed cathode (NVP) and anode (NTP) were punched into discs with a diameter of 20 mm, and a coin cell was assembled in the configuration of NVP/electrolyte-soaked membrane/NTP. Rate performance tests were conducted at 0.5C, 1C, and 5C for 5 cycles for each C rate. Cycling performance was assessed by cycling the coin cells at 1C at RT with a cutoff voltage range of 0.6 – 1.6V.

4.3 Results and Discussion

4.3.1 Freezing Behavior in Bulk Solutions

Figure 4.2 shows a series of photos of the freezing behavior of PVDF-HFP/DMSO/TEOS solutions with 20 wt% PVDF-HFP and DMSO/TEOS ratios of 80/0, 72/8, and 64/16 at 4 ^{o}C. In the cases of the solutions with DMSO/TEOS ratios of 80/0 (Figure 4.2 (a)) and 72/8 (Figure 4.2 (b)), neither shows signs of cloudiness before the freezing of the solvent, as evidenced by the observation of frozen crystals marked by the red circles. A striking difference is observed as the DMSO/TEOS ratio reaches 64/16 (Figure 4.2 (c)). Cloudiness formation is seen as marked by the yellow circle in the left-most figure in Figure 4.2 (c) and progresses to the entire vial prior to the freezing of the solvent. The fact that TEOS is considered a bad solvent for PVDF-HFP is responsible for the liquid-liquid phase separation to precede solvent freezing in the solution containing 16 wt% TEOS. In Figure 4.2 (d), it is clear that the distance between PVDF-HFP and TEOS is greater than that between PVDF-HFP and DMSO in the 3D Hansen solubility space, indicating the low compatibility between PVDF-HFP and TEOS.
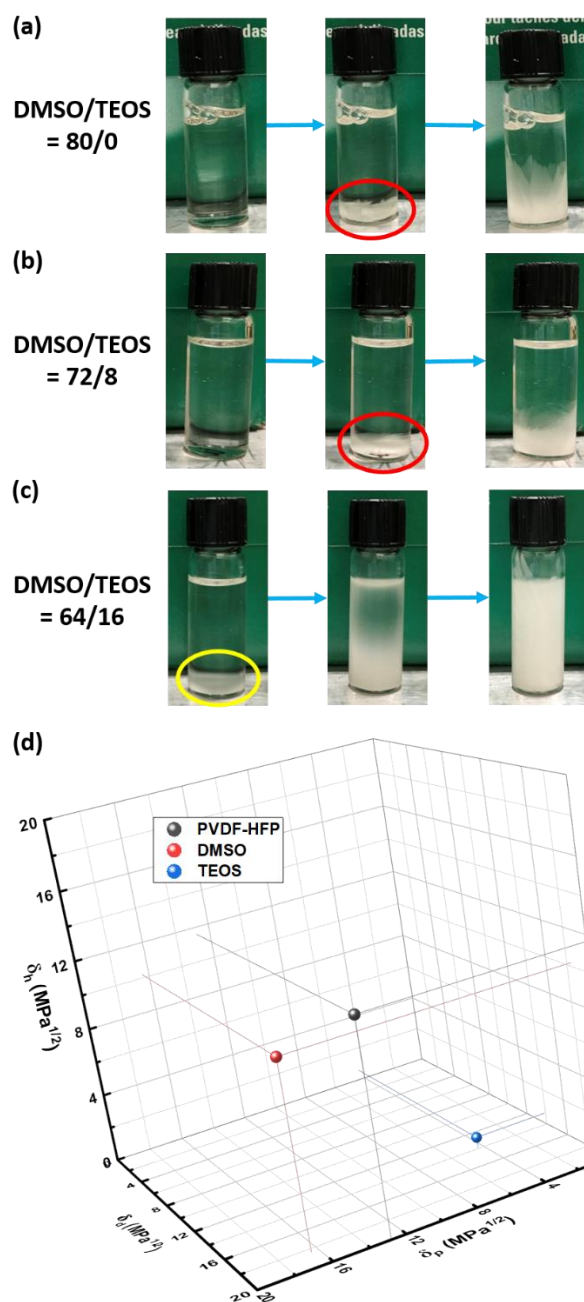
Figure 4.2 Photo images of freezing behavior of PVDF-HFP/DMSO/TEOS solutions with DMSO/TEOS ratios of (a) 80/0, (b) 72/8, and (c) 64/16 at 4 °C. Arrows indicate the chronological order while red and yellow circles highlight the frozen solvent crystals and cloudiness formation, respectively. (d) solubility parameters of PVDF-HFP, DMSO, and TEOS plotted in the 3D Hansen solubility space.

4.3.2 Effects of TEOS on Membrane Microstructures

Surface microstructures of PH20D80 (polymer membrane), PH20D72T8, and PH20D64T16 (composite membranes) are presented in Figure 4.3. Here, the cold face refers to the face of the membrane that was closer to the pre-chilled Al stage and had direct contact with the Al substrate, while the hot face was away from the Al stage and exposed to atmosphere. For PH20D80 and PH20D72T8, submicron pores are seen on the cold face (Figure 4.3 (a) and (b)), while pores of a few micrometers are found on the hot face (Figure 4.3 (d) and (e)). This difference in pore size is attributed to the difference in cooling rate on the two faces, where higher cooling rate on the cold face leads to smaller pore size while the lower cooling rate on the hot face produces larger pore size [103].

However, in the case of PH20D64T16, the pore size is larger on the cold face (Figure 4.3 (c)) than on the hot face (Figure 4.3 (f)), larger than those on the cold face of PH20D80 and PH20D72T8. The reason for this difference in pore size and distribution is due to the fact that the liquid-liquid phase separation (LLPS) of the solution precedes the freezing of solvent in the case of PH20D64T16, as evidenced in Figure 4.2 (c). After the solution is poured onto the Al substrate for tape casting, the portion of the solution that is in direct contact with the Al substrate starts to phase-separate into a polymer-rich (solvent-lean) and a polymer-lean (solvent-rich) phase. Tape casting then spreads this phase-separated layer across the Al substrate which later freezes and ultimately forms the cold face. The subsequent freezing step crystallizes the solvent in the polymer-lean phase and the frozen solvent crystals are then washed away during solvent extraction, thus leaving large, circular pores on the cold face.

PH20D80 **PH20D72T8** **PH20D64T16**
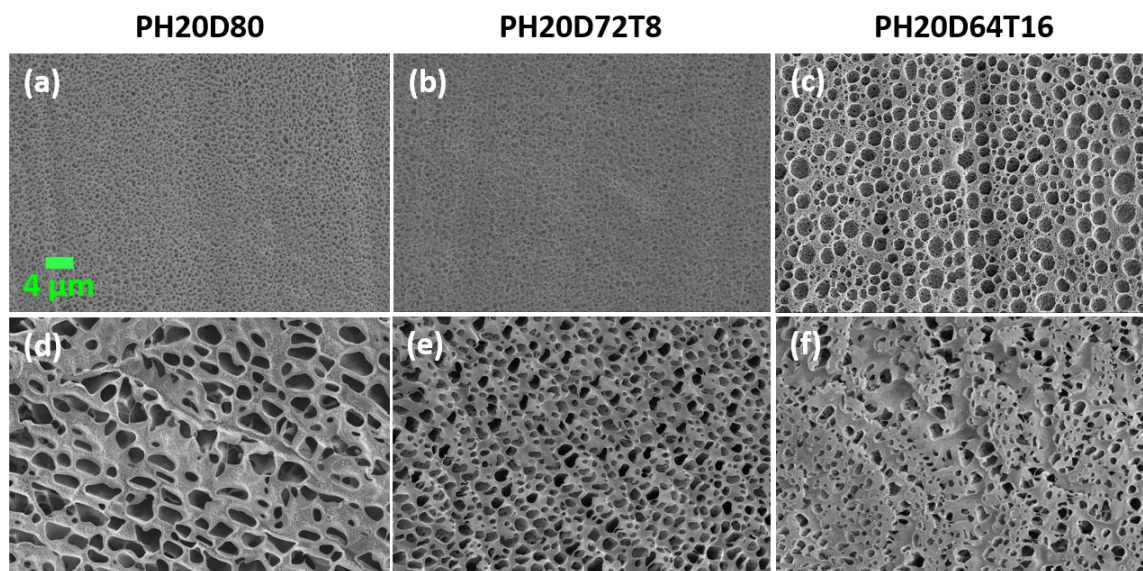
Figure 4.3 Surface micrographs on cold face of (a) PH20D80 (b) PH20D72T8 (c) PH20D64T16; surface micrographs on hot face of (d) PH20D80 (e) PH20D72T8 (f) PH20D64T16. All micrographs share the same scale bar.

Since working ions in a battery need to diffuse back and forth between the cathode and anode while passing through the separator during charging and discharging, the cross-section of a separator is of utmost importance. Shown in Figure 4.4 are the cross-sectional micrographs and corresponding Si EDS mapping results of PH20D80, PH20D72T8, and PH20D64T16. Cross-sectional images (Figure 4.4 (a), (b), and (c)) of all membranes studied, regardless of the TEOS content, exhibit through-thickness and directionally aligned porous structures. Therefore, all three membranes are considered legitimate candidates to be used as battery separators. The alignment of pores in the thickness direction is a direct result of the thermal gradient in the vertical direction along which solvent crystals grow during the freeze casting process [104].

According to the corresponding Si EDS mapping results, negligible signal is detected in P20D80 (Figure 4.4 (d)), while the Si signal is enhanced with the addition of TEOS, in PH20D72T8 (Figure 4.4 (e)) and increasing in PH20D64T16 (Figure 4.4 (f)), consistent with

increasing amount of TEOS. The EDS mapping also confirms the uniform distribution of silica across the cross-sections of membranes. When observing the cross-sections at a higher magnification, a hierarchical pore morphology with circular pores on the aligned pore walls is found in PH20D72T8 (Figure 4.4 (h)) and PH20D64T16 (Figure 4.4 (i)), while such features are not present in the membrane containing no TEOS (PH20DE80 (Figure 4.4 (g))). The formation of circular pores in pore walls is attributed to the added TEOS which is expelled by the frozen DMSO crystals and entrapped in the PVDF-HFP matrix during freezing and subsequently consumed by the sol-gel reaction [23] or washed away during the rinsing step.
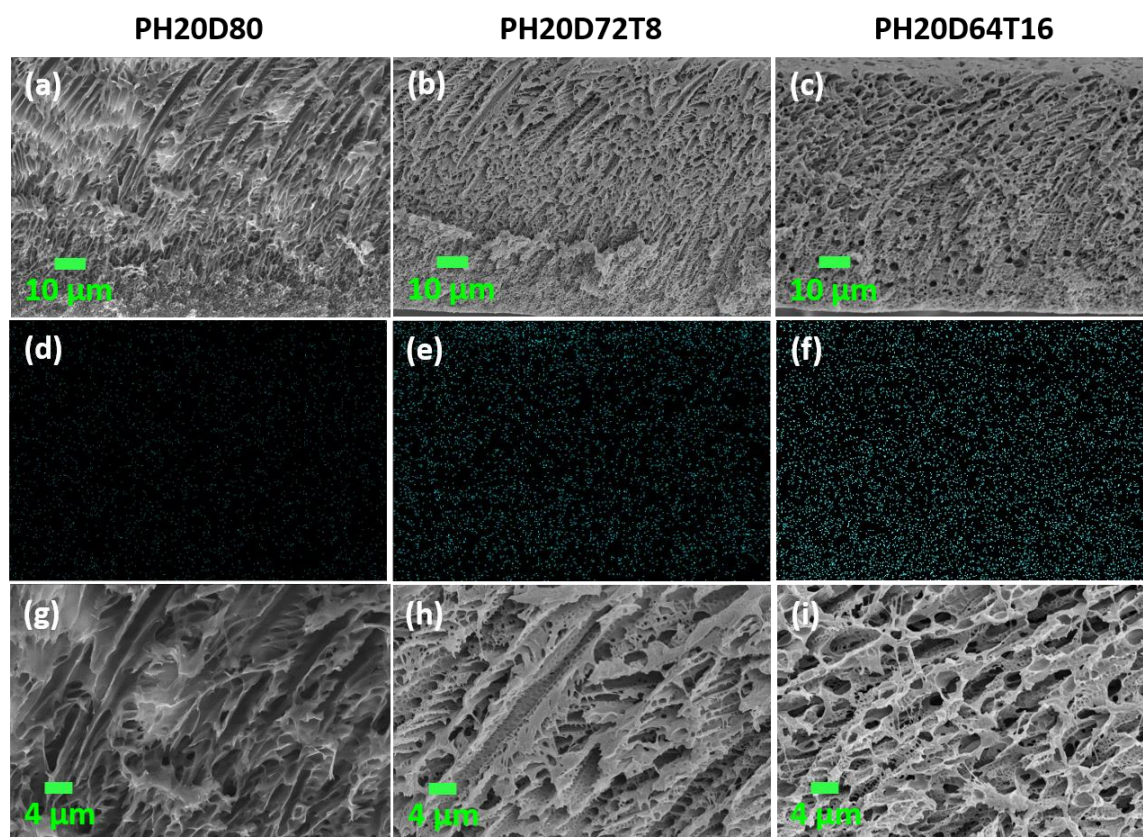
Figure 4.4 Cross-sectional micrographs and corresponding Si EDS mapping results of (a)(d) PH20D80 (b)(e) PH20D72T8 (c)(f) PH20D64T16; (g)(h)(i) cross-sectional micrographs of (a)(b)(c) at higher magnifications.

4.3.3 Physical Characterization of Polymer and Composite Membranes

4.3.3.1 Phase Composition from FTIR Spectra

FTIR spectra of PH20D80, PH20D72T8, and PH20D64T16 collected on both cold and hot faces are shown in Figure 4.5. The wavenumber range presented here spans from 1500 to 400 cm^{-1}, the range in which most of the characteristic peaks of PVDF-HFP fall. While comparing the spectra collected from both faces of each membrane, little difference in absorption peaks is found, which suggests the uniformity in phase composition in each membrane. It is clear that all three membranes share a highly similar spectrum in which the exclusively characteristic peaks of β and γ phase of the PVDF segment around 1275 and 1234 cm $^{-1}$ are present, suggesting all three membranes are composed of a mixture of β and γ phases [82]. The β (TTTT conformation) and γ (TTTGTTTG' conformation) phases, two polar polymorphs of PVDF, have been reported to form in the presence of solvents with high dipole moments [83, 105], and consistent with the current case, DMSO (dipole moment = 3.96 D) [106]. The thermal energy during solution preparation (70 $^{\circ}$C) in conjunction with the polar moieties of DMSO facilitates the rotation of CF$_2$ groups in PVDF-HFP, resulting in a cooperative motion of neighboring CF$_2$ groups, and hence, align the polymer chains in both β and γ phases [107, 108]. One striking difference in the spectra between the polymer (black) and composite membranes (red and blue) is the additional absorption band associated with the Si-O-Si groups (highlighted by green inverted triangles) around 1100 cm^{-1} [23] observed in the composite membranes, consistent with the EDS results.
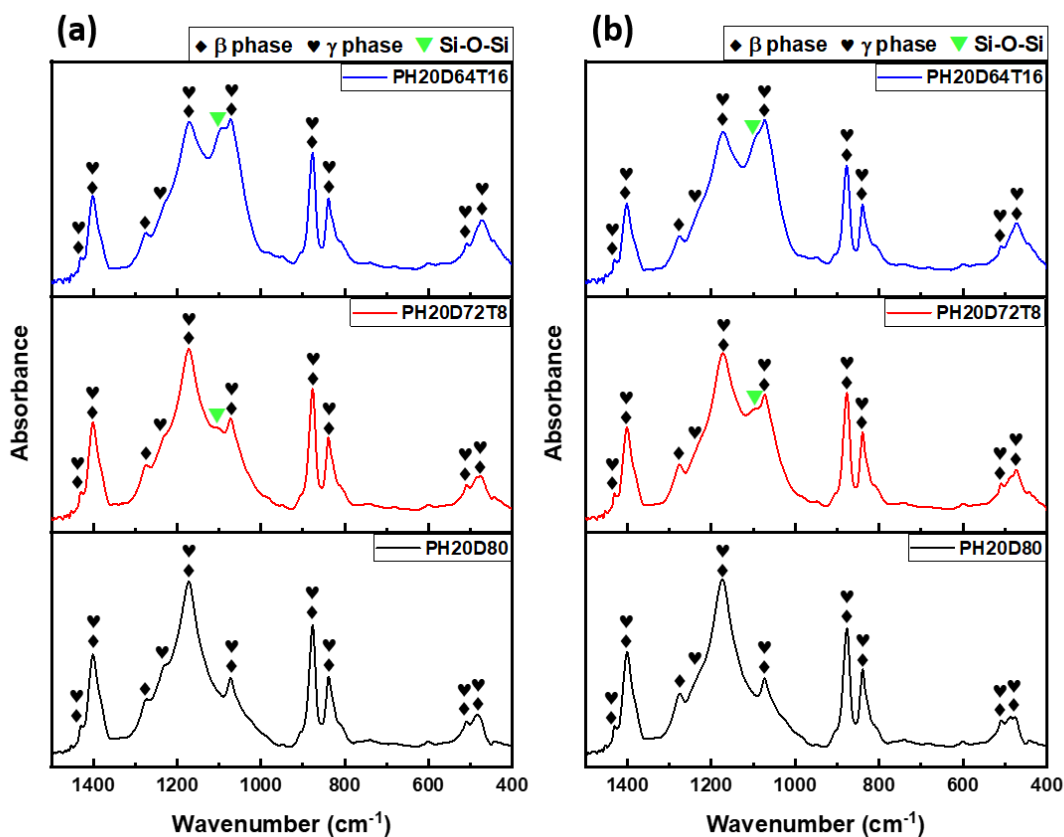
Figure 4.5 FTIR spectra of PH20D80, PH20D72T8, and PH20D64T16 on (a) cold face and (b) hot face. (Green inverted triangles denote the peaks form Si-O-Si bonds.)

4.3.3.2 Porosity, Mechanical Properties and Thermal Stability

Porosity values and mechanical properties including Young's modulus, tensile strength, and strain-to-failure as well as the corresponding p values determined from analysis of variance (ANOVA) of PH20D80, PH20D72T8, and PH20D64T16 are tabulated in Table 4.1. Despite the addition of TEOS in the cases of PH20D72T8 and PH20D64T16, all three membranes exhibit similar porosity values around 80%.

In terms of stiffness, PH20D72T8 (~ 70 MPa) and PH20D64T16 (~ 88 MPa) exhibit an approximately 40% and 75% increase in Young's modulus, respectively, in comparison with PH20D80 (~ 50 MPa). Given the similarity in porosity and microstructure amongst the three membranes, the improvement in Young's modulus is attributed to the added silica particles that act as stiffening inclusions. The fact that the corresponding p value from ANOVA is found to be smaller than 10^{-4} suggests that the stiffening effect of silica particles is significant. In contrast, the p value associated with tensile strength is found to be much greater than 0.05, which indicates that the strengthening effect of silica particles is insignificant. Three likely reasons for the insignificant strengthening effect are (1) the amount of added silica is too low to compensate for the high degree of porosity ($> 80\%$) of the membranes, (2) the pores in the aligned pore walls of the hierarchical pore structures of PH20D72T8 and PH20D64T16 (Figure 4.4 (h) and (i)), and (3) the large, circular pores on the cold face of PH20D64T16 (Figure 4.3 (c)) serve as flaws and counteract any strengthening effect. As would be expected, the increase in Young's modulus with silica addition is accompanied with a decrease in strain-to-failure.

Table 4.1 Porosity, Young's modulus, tensile strength, strain-to-failure, and corresponding p values determined from analysis of variance (ANOVA) of PH20D80, PH20D72T8, and PH20D64T16.

Membrane ID	Porosity (%)	Young's modulus (MPa)	Tensile strength (MPa)	Strain-to-failure (%)
PH20D80	81.25 ± 0.83	50.37 ± 6.60	2.78 ± 0.31	181.21 ± 32.01
PH20D72T8	80.49 ± 0.78	70.67 ± 6.61	2.93 ± 0.23	149.54 ± 8.96
PH20D64T16	80.72 ± 0.56	87.81 ± 9.60	3.07 ± 0.44	149.51 ± 13.89
P value (ANOVA)		< 0.0001	0.4291	0.051

Thermal stability of a separator is critical due to its role as the physical barrier between the electrodes during battery operation. Therefore, TGA was used to assess the thermal stability of PVDF-HFP-based membranes. Figure 4.6 shows the TGA thermograms of PH20D80, PH20D72T8, and PH20D64T16 in terms of weight loss and derivative of weight loss as a function of temperature. The temperature range presented here spans 300 to 600 $^{\circ}$C, since most thermal degradation of interest falls into this range. In Figure 4.6 (a), it is clear that all three membranes exhibit a single-step thermal decomposition due to the degradation of PVDF-HFP backbone units [108]. Upon closer examination in the temperature range from 425 to 475 $^{\circ}$C, a shift in breakdown temperature (the segment with the greatest slope) towards higher temperatures is found with increasing silica. This shift towards higher temperatures is an indication of higher thermal stability of the composite membranes (PH20D72T8 and PH20D64T16) compared to their polymer counterpart (PH20D80). The enhanced thermal stability is ascribed to the strong interaction between dispersed silica and polymer chains, and hence, higher energy is required for PVDF-HFP chain degradation [109], rendering an increase in breakdown temperature. A more obvious shift towards higher temperatures can be seen in Figure 4.6 (b) where the derivatives of weight loss with respect to temperature are plotted against temperature. The breakdown temperature shifts from 455 $^{\circ}$C for PH20D80 to 462 $^{\circ}$C for PH20D72T8 and to 470 $^{\circ}$C for PH20D64T16, as another suggestion of minimally greater thermal stability.
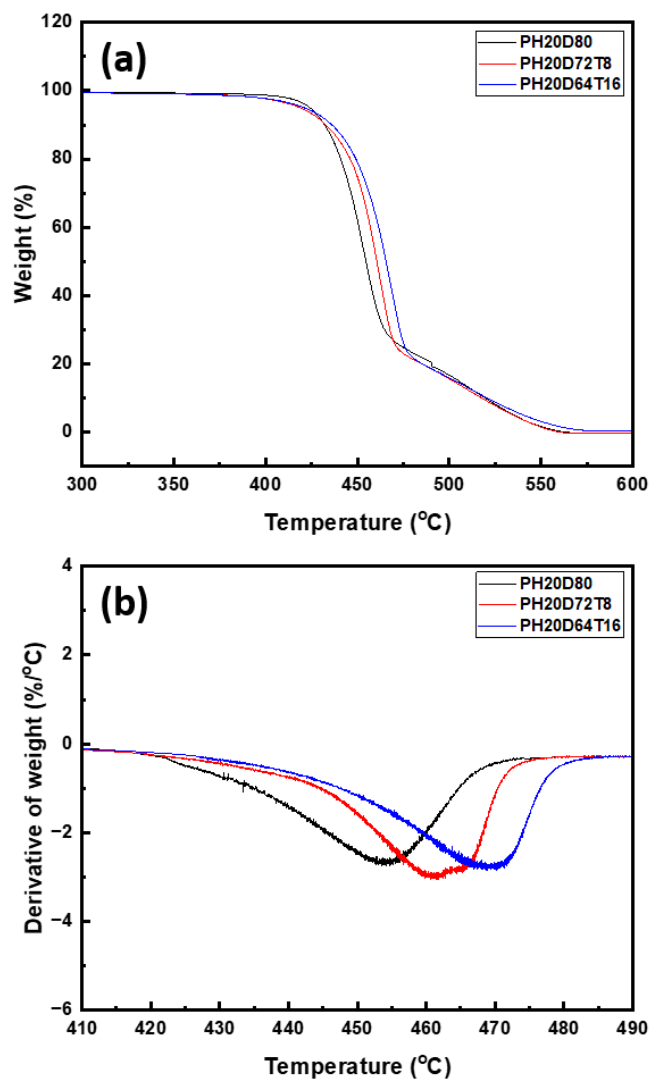
Figure 4.6 TGA thermograms of PH20D80, PH20D72T8, and PH20D64T16 showing (a) weight loss and (b) the derivative of weight loss as a function of temperature.

4.3.3.3 Contact Angles and Electrolyte Uptake

Wettability (electrolyte affinity), mostly evaluated by contact angle measurement, is an important factor that greatly affects the battery performance. A wetted separator by the electrolyte provides better contact with the electrodes as well as improved ionic conductivity.

Contact angles of the organic electrolyte and the ionic liquid on PH20D80, PH20D72T8, and PH20D64T16 along with the reference Celgard 2500 are plotted in Figure 4.7. It can be seen that both electrolytes show smaller contact angles on all three membranes compared to Celgard, which is an indication of greater electrolyte affinity with PVDF-HFP-based membranes than Celgard. The poor electrolyte affinity of Celgard is attributed to its hydrophobic surface [66] and low porosity (~ 55%).

While comparing the three PVDF-HFP-based membranes, contact angles of both electrolytes are found to decrease with increasing amount of silica, with PH20D64T16 showing 14° and 19° of contact angles with the organic electrolyte and ionic liquid, respectively. These indicate an improvement in electrolyte affinity with silica addition to the polymer membrane. Given similar porosity among the three membranes, this enhancement in electrolyte affinity is closely related to the increased hydrophilicity due to the hydroxyl group attached to the surface of dispersed silica particles [110].
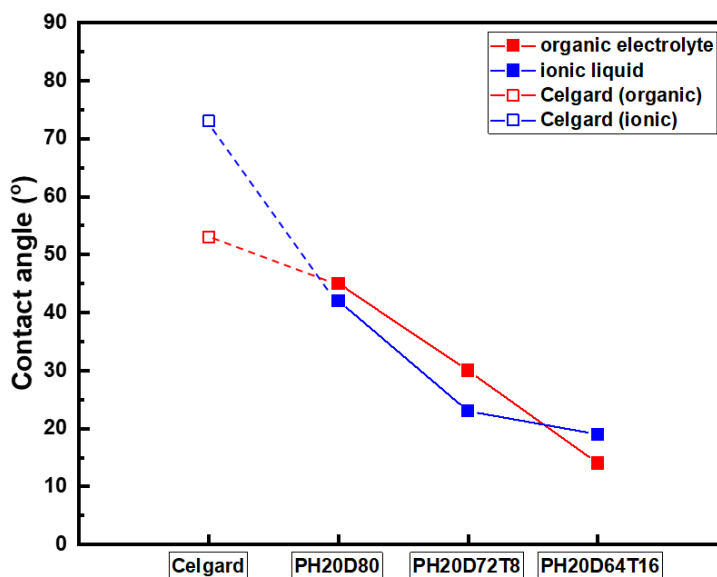
Figure 4.7 Contact angles of organic electrolyte and ionic liquid on PH20D80, PH20D72T8, and PH20D64T16 with Celgard 2500 as a reference.

Electrolyte uptake, the electrolyte retention capacity of a separator, is directly related to the ionic conductivity and cell performance [111]. Figure 4.8 shows the electrolyte uptake values of PH20D80, PH20D72T8 and PH20D64T16 in the organic electrolyte and the ionic liquid with both Celgard 2500 and filter paper as references. Compared with the two references, all three PVDF-HFP-based membranes exhibit higher uptake values in both electrolytes. Given the low uptake values of Celgard, due to the low porosity (~ 55%) and poor affinity with both electrolytes, Celgard is excluded from electrochemical performance evaluations.

Amongst the three PVDF-HFP-based membranes, it is found that PH20D72T8 and PH20D64T16 show higher uptake values in both electrolytes than PH20D80. Given similar porosities among the three membranes, this enhancement in electrolyte uptake can be attributed to two factors. First, the added silica in the composite membranes improves their electrolyte affinity [64]. Second, TEOS inhibits the crystallization of PVDF-HFP in the cryo-concentrated regions (pore walls) that consist of PVDF-HFP and TEOS rejected by the frozen DMSO during freeze casting. This leads to an increase in amorphous PVDF-HFP phase with higher electrolyte retention capacity [111]. The circular pores in the directional pore walls as a result of the TEOS addition in the composite membranes (Figure 4.4 (h) and (i)) also contribute to higher uptake values due to the increased pore surface area [112]. Combining the results of contact angle (Figure 4.7) and electrolyte uptake (Figure 4.8), it is confirmed that the addition of silica to the polymer membrane improves the affinity with both the organic electrolyte and the ionic liquid.
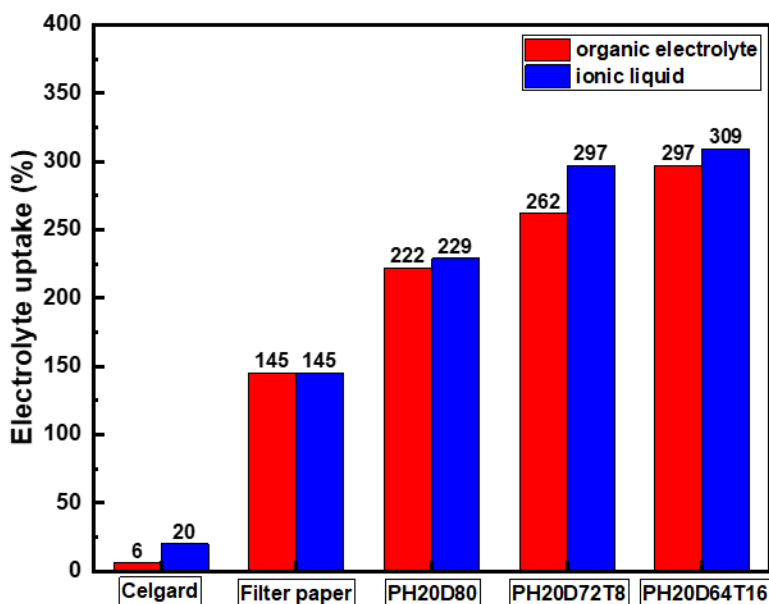
Figure 4.8 Electrolyte uptakes of PH20D80, PH20D72T8, and PH20D64T16 in organic electrolyte and ionic liquid with Celgard 2500 and filter paper as references.

4.3.4 Electrochemical Performance

4.3.4.1 Ionic Conductivity and MacMullin Number

Ionic conductivity is a key measurement of charge transport between the electrodes, and therefore is of great significance in determining the battery performance. Ionic conductivity and MacMullin numbers of PH20D80, PH20D72T8, and PH20D64T16 in both the organic electrolyte and the ionic liquid with the filter paper as a reference are tabulated in Table 4.2. In both electrolytes, it is clear that all of the PVDF-HFP-based membranes show at least a two-fold increase in ionic conductivity than the filter paper. Generally, the ionic conductivity of a separator saturated with an electrolyte is a function of the separator porosity, pore tortuosity, and electrolyte wettability [113]. Not surprising then, when compared with the filter paper, the enhanced ionic conductivity of the PVDF-HFP-based membranes noted in

Table 2 is can be credited to the aligned pore morphology (Figure 4.4) and greater electrolyte uptake. Amongst the PVDF-HFP-based membranes, an increasing trend in ionic conductivity is further found with increasing silica content, with PH20D64T16 exhibiting the highest ionic conductivity of 2.0 mS/cm in the organic electrolyte and 1.8 mS/cm in the ionic liquid. This trend in ionic conductivity with added silica can be attributed to three effects: (1) the greater electrolyte uptake due to higher electrolyte affinity and hierarchical pore structure [114], (2) the circular pores located on the cold face of PH20D64T16 (Figure 4.3 (c)) to facilitate ionic transport, and (3) the improved electrolyte dissociation caused by the Lewis acid-base interaction between the acidic silica and the anions of electrolyte leading to more active ions for transport [115].

A reverse trend in MacMullin number, the ratio of ionic conductivity of pure electrolyte to that of a separator soaked with electrolyte, is expected. Indeed, all three PVDF-HFP-based membranes exhibit lower MacMullin numbers than filter paper while a decreasing trend is found with increasing amount of silica, with PH20D64T16 exhibiting the lowest MacMullin numbers of 5.0 in the organic electrolyte and 3.7 in the ionic liquid. Given that the MacMullin number is a figure of merit for battery separators, the composite membranes are considered better separators than the polymer counterpart and filter paper.

Table 4.2 Ionic conductivity and MacMullin number of polymer and composite membranes in organic electrolyte and ionic liquid with filter paper as a reference.

Membrane ID	Ionic conductivity in organic electrolyte (mS/cm)	Ionic conductivity in ionic liquid (mS/cm)	MacMullin number in organic electrolyte	MacMullin number in ionic liquid
Filter paper (reference)	0.7	0.6	14.9	10.3
PH20D80	1.4	1.2	7.1	5.6
PH20D72T8	1.6	1.2	6.2	5.6
PH20D64T16	2.0	1.8	5.0	3.7

4.3.4.2 Rate Performance and Cycling Performance in Coin Cells

In order to evaluate the efficacy of PVDF-HFP-based membranes as SIB separators, rate performance and cycling performance of NVP/NTP coin cells assembled with such membranes have been conducted. Figure 4.9 summarizes the capacity retention (0.5C vs. 5C) of NVP/NTP coin cells assembled with filter paper, PH20D80, PH20D72T8 and PH20D64T16 as separators in both the organic electrolyte and the ionic liquid. While comparing the two electrolytes, it is clear that all of the organic electrolyte-based cells exhibit higher capacity retention than the ionic liquid-based cells. The higher viscosity and ionic resistivity of the ionic liquid are responsible for the lower capacity retention values obtained from the ionic liquid-based cells.

In the case of the organic electrolyte, the coin cells with the composite separators (PH20D72T8 and PH20D64T16) show higher capacity retention than those with the polymer separator (PH20D80) and filter paper, with the highest value of 72% obtained from the cell assembled with PH20D64T16. Similarly, amongst the ionic liquid-based coin cells, higher capacity retention values are obtained in the coin cells with the composite separators, with the highest retention of 52% obtained from the cell assembled with PH20D64T16. Compared with the cells assembled with filter papers, the greater capacity retention of cells with PVDF-HFP-based separators is ascribed to the higher ionic conductivity [116] and greater electrolyte uptake. Amongst the cells assembled with PVDF-HFP-based separators, the improved capacity retention with added silica content is in accordance with ionic conductivity and electrolyte uptake, which benefits the rate performance [117].
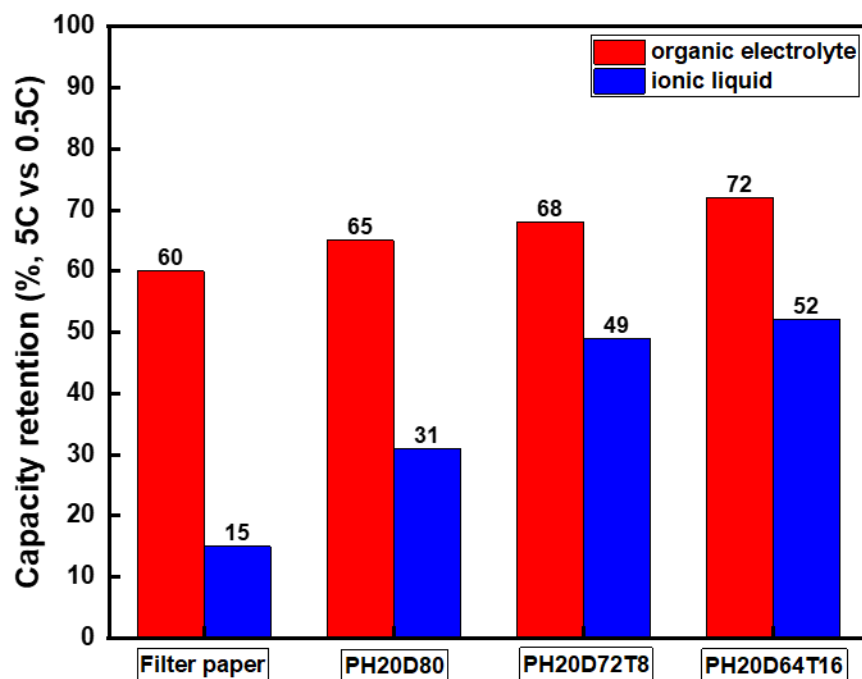
Figure 4.9 Rate performance (capacity retention at 5C vs. 0.5C) of coin cells with PH20D80, PH20D72T8, and PH20D64T16 in organic electrolyte and ionic liquid.

Figure 4.10 compares the cycling performance of NVP/NTP coin cells made with the filter paper and PH20D64T16 in both the organic electrolyte and the ionic liquid. In the case of the organic electrolyte (Figure 4.10 (a)), it is clear that the cell assembled with PH20D64T16 outperforms the cell assembled with the filter paper in terms of capacity retention and cycle number. This is not surprising given that the cell assembled with PH20D64T16 delivers the best performance in terms of contact angle, electrolyte uptake, ionic conductivity, and capacity retention. The cell with PH20D64T16 delivers an 80% capacity retention around 175 cycles, while the same retention is observed only at the 15th cycle in the case of the filter paper-based cell. Additionally, the cell with PH20D64T16 exhibits a capacity retention of 60% at 500 cycles, while the filter paper-based cell delivers the same retention around 80

cycles and stops around 115 cycles due to either cell degradation caused by increase in impedance or cell failure as a result of short circuit.

In the case of the ionic liquid (Figure 4.10 (b)), the filter paper-based cell is not stable even at initial cycles and can no longer operate beyond 200 cycles. In striking contrast, the composite separator-based cell exhibits significant improvement in cycling performance with an approximately 75% of capacity retention after 800 cycles. The advanced capacity retention and cycling stability of the cells assembled with PH20D64T16 can be attributed to greater ionic conductivity and electrolyte uptake to retain electrolyte during repeated cycling [118, 119]. Given the noteworthy results of rate and cycling performance, composite PVDF-HFP/SiO$_2$ membranes are considered promising alternative separators to filter papers.
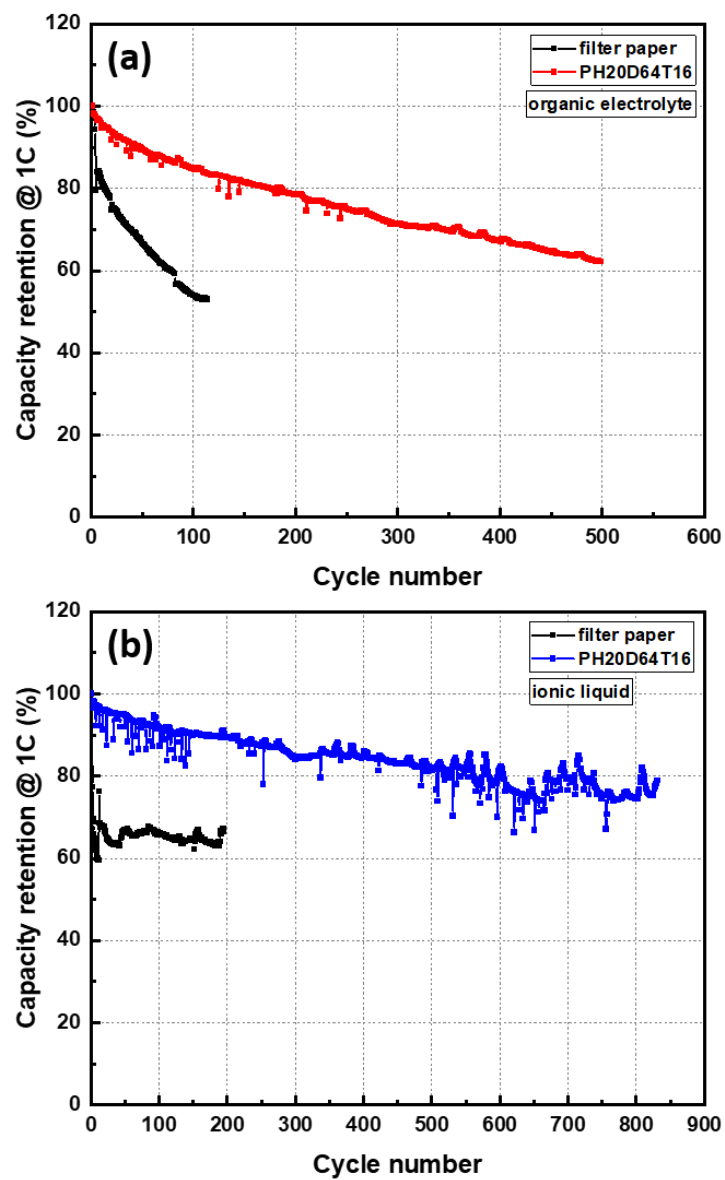
Figure 4.10 Cycling performance (@ 1C) of coin cells using filter paper and PH20D64T16 in (a) organic electrolyte and (b) ionic liquid.

4.4 Conclusions

In this chapter, the effects of TEOS and the resulting silica reinforcements from a sol-gel reaction of TEOS in tape/freeze-cast PVDF-HFP membranes on microstructure, phase composition, thermal stability, mechanical and electrochemical properties have been studied. Liquid-liquid phase separation is found to precede the freezing of DMSO when the co-solvent ratio of DMSO/TEOS reaches 64/16. A through-thickness, directionally aligned porous structure is obtained in PVDF-HFP membranes fabricated via freeze casting with DMSO as the solvent, while a hierarchical pore morphology with circular pores on the aligned pore walls is observed with TEOS added as a co-solvent. With the incorporation of silica confirmed by EDS and FTIR, little change is found in the porosity and phase composition of the tape/freeze-cast membranes. However, the improvement in thermal stability and elastic modulus along with electrolyte affinity and ionic conductivity of the membranes is attributed to the added silica. More importantly, in terms of electrochemical performance, the NVP/NTP coin cells with composite membranes as separators deliver better rate performance and cycling stability than those with polymer membranes and filter papers in both organic electrolytes and ionic liquids. The improved electrochemical properties are ascribed to the greater electrolyte uptake and enhanced ionic conductivity due to the added silica. As a consequence, the tape/freeze-cast composite membranes are considered more promising separators than conventional filter papers for sodium-ion batteries.

C h a p t e r   5

PERMEABLE SIOC SCAFFOLDS

Material in this chapter is reproduced in part from "Directionally aligned macroporous SiOC via modified freeze casting of polysiloxane/tert-butyl alcohol solution", C. Wu, K.T. Faber; *Manuscript in preparation*. The work was done in collaboration with Katherine T. Faber. C. Wu fabricated and characterized SiOC samples using SEM and MIP and their permeabilities, and wrote the manuscript. K.T. Faber supervised this work.

5.1 Introduction

Chapters 3 and 4 explored the capability and versatility of freeze casting for producing oxide-reinforced PVDF-HFP membranes with Al_2O_3 and SiO_2 introduced via ball milling and the co-solvent method, respectively. The composite membranes were evaluated in terms of electrolyte affinity, mechanical, thermal, and electrochemical properties and were found to be promising separators for Na-ion batteries.

Apart from membranes used as separators in the battery field, freeze casting is also a favorable processing technique to fabricate ceramic scaffolds due to its tailorability in pore structures [2, 120, 121]. Permeability, one of the critical characteristics of ceramic scaffolds, is strongly dependent on the pore alignment and morphology of scaffolds, which are highly tunable in freeze casting [2]. For example, in terms of pore alignment, the inherent thermal gradient of directional freeze casting along which solvent molecules freeze and crystallize facilitates the alignment in the resultant pore structures [16]. In addition, external aids such as grain selection templates [31] and magnetic fields [32] also improve the pore alignment. In terms of pore morphology which can be controlled by choice of solvent [2] and by freezing parameters (the freezing front velocity and the thermal gradient [25, 26]) prismatic and lamellar pore structures are found to deliver excellent permeability amongst various types of pore morphologies. However, lamellar structures exhibit poor mechanical response due to

the susceptibility to failure from shear fracture caused by insufficient inter-lamellar connections [122]. Therefore, prismatic pore structures are chosen as the case of study.

Freeze casting systems for ceramic scaffold fabrication can generally be divided into two categories: suspension and solution systems. In comparison with suspension-based freeze casting, solution-based freeze casting with preceramic polymers offers advantages including simpler processing without suspension preparation and direct observation of freezing due to the transparency of solutions.

In this chapter, a binary system of polymethylsiloxane preceramic polymer (MK) and tert-butyl alcohol (TBA) which forms prismatic crystals upon freezing, was selected to fabricate permeable silicon oxycarbide (SiOC) scaffolds. Arai et al. [26] have recently reported that the two thermoelectric plates used in a double-sided, gradient-controlled freeze casting setup allow for independent control of the freezing front velocity and the thermal gradient. The effects of different freeze casting configurations including the single-sided (SS, Figure 5.1 (a)), double-sided (DS, Figure 5.1 (b)), and template-assisted double-sided (TDS, Figure 5.1 (c) and (d)) on freezing behaviors of MK-TBA solutions and resultant pore structures were investigated. The significant difference in freezing behavior of solutions between the SS and the DS and TDS configurations had been earlier explained by supercooling theory [26, 103]. Moreover, water permeability was used to assess the pore alignment within the scaffolds fabricated by the DS and TDS configurations.
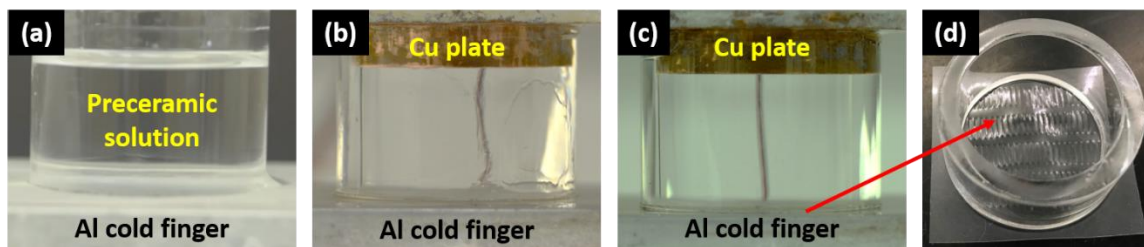
Figure 5.1 Freeze casting configuration of (a) single-sided (SS) (b) double-sided (DS) (c) template-assisted double-sided (TDS) and (d) templated Mylar film substrate used in (c).

5.2 Experimental Methods

5.2.1 Materials

Polymethylsiloxane preceramic polymer (CH_3-$SiO_{1.5}$, Silres® MK Powder, Wacker Chemie, Munich, Germany) and tert-butyl alcohol (TBA, Sigma Aldrich, St. Louis, MO, USA) were used to produce polymer solutions for phase diagram construction and freeze casting. N-(2-Aminoethyl)-3-aminopropyltrimethoxysilane (Geniosil® GF 91, Wacker Chemie) was added to polymer solutions as a cross-linking agent.

5.2.2 Preceramic Polymer Solutions

Given that the melting point of TBA (25-26 ℃) is close to room temperature, TBA was first heated at 40 ℃ until fully melted prior to mixing with the preceramic polymer. Mixtures of 10, 20, 30, 40 wt% preceramic polymer with corresponding 90, 80, 70, 60 wt% TBA were heated in glass vials in a water bath at 40 ℃ under constant stirring with magnetic stir bars until clear and homogeneous solutions were produced. The cross-linking agent was added at a concentration of 1 wt% to each polymer solution and stirred for 5 min to partially cross-link the polymer chains. The polymer solutions were degassed for 10 min to remove air bubbles.

5.2.3 Construction of Phase Diagram of Polymer Solutions

The polymethylsiloxane preceramic polymer-TBA phase diagram was constructed by visual inspection. A fixed volume of 20 μL of each polymer solution and pure TBA was pipetted onto the freeze casting setup. This setup consisted of an Al cold finger on top of a thermoelectric plate which was placed on top of a heat reservoir connected to a circulating refrigerated silicone oil bath (FP50-ME, Julabo USA Inc., Allentown, PA, USA). The thermoelectric plate was connected to a PID controller which also recorded temperature profiles. Once the polymer solution and pure TBA was placed on top of the Al cold finger, a microscope cover slip was immediately covered to minimize solvent evaporation and moisture absorption. A petri dish was placed over the setup to prevent condensation and reduce ambient air flow. The freezing point, T_f, was recorded as the temperature at which the first observed nucleation, perceived by an abrupt change in solution opacity, took place at a

cooling rate of 1 ^{o}C/min. The liquidus temperature, T_L, was determined by first freezing the solution at a cooling rate of 1 ^{o}C/s and then heating at a rate of 1 ^{o}C/min. Solutions turn opaque as they solidify, while solutions turn transparent as the temperature approaches T_L. T_L was recorded as the temperature at which the last opaque section turns transparent. Five samples were tested for each solution and their average values with standard deviation were reported.

5.2.4 Freeze Casting

The mixture of 20 wt% preceramic polymer with 80 wt% TBA was poured into a glass mold (h = 20 mm, $\varnothing$ = 25 mm) whose base was sealed with a Mylar film substrate and vacuum grease to prevent leakage. For the single-sided freeze (SS) casting configuration, the mold was placed onto the freeze casting setup described in the previous section to carry out the freeze casting process. Naviroj [2] has reported that certain solvents including cyclooctane, cyclohexane, dioxane, and dimethyl carbonate produced flat and trackable freezing fronts, while solvents such as tert-butyl alcohol, camphene, and p-xylene displayed untraceable freezing fronts.

For the double-sided (DS) freeze casting configuration, besides the Al cold finger on which the mold was placed, a Cu plate attached to another PID-controlled thermoelectric plate whose temperature was set at 40 ^{o}C was placed on top of the mold to impose a larger thermal gradient in the solution. Due to the shrinkage accompanied by solidification, the copper plate was designed to be inserted 5 mm into the glass mold to ensure constant contact between the solution and the Cu plate over the course of freezing.

For the template-assisted double-sided (TDS) freeze casting configuration, the procedure was identical to the double-sided freeze casting setup, with the addition of a templated Mylar film substrate instead of a regular, smooth Mylar film substrate. The templated Mylar film substrate was made by pressing a pair of locking tongs with serrated jaw against a smooth Mylar film substrate to create a ridged surface, as shown in Figure 5.1 (d). The freezing front velocities of DS and TDS configurations were determined from the images taken by a camera

with an intervalometer at an interval of 10 s using ImageJ (National Institutes of Health) for image analysis. After complete freezing, frozen samples were placed into a freeze dryer (VirTis AdVantage 2.0, SP Scientific, Warminster, PA, USA) set at -40 °C and 500 μbar until the solvent was fully sublimated. The freeze-dried green bodies were pyrolyzed at 1100 °C in argon for 4 hours with a ramp rate of 2 °C/min to convert polymethylsiloxane into silicon oxycarbide (SiOC).

5.2.5 Characterization

For characterization made on SiOC scaffolds fabricated by DS and TDS configurations, samples were obtained from the part with constant freezing front velocities (4 mm to 9 mm from the base). In the case of SiOC scaffold produced by SS configuration, samples were obtained from the corresponding position in terms of height.

5.2.5.1 Porosity and Pore Size Distribution

Sample porosity was determined using the Archimedes method with deionized water as the immersion fluid following ASTM C373. Three samples of each condition were measured and the average value was reported with standard deviation. Pore size distribution of porous SiOC samples was collected using a mercury intrusion porosimeter (MIP, Auto Pore IV 9500, Micromeritics Instrument Corp., Norcross, GA, USA). MIP relies on the non-wetting nature of mercury and measures the volume of mercury infiltrated into pores as a function of applied pressure according to the Washburn equation [123]:

$$d = \frac{-4\gamma \cos\theta}{P} \qquad (5.1)$$

where d is the pore size, γ is the surface tension, θ is the contact angle between the mercury and the sample, and P is the applied pressure.

5.2.5.2 Microstructure

Microstructures of porous SiOC were examined by scanning electron microscopy (FESEM, ZEISS 1550 VP, Carl Zeiss Microscopy GmbH, Jena, Germany) with an accelerating voltage of 10 kV. Each SiOC sample was sectioned in both longitudinal (parallel to the freezing direction) and transverse (perpendicular to the freezing direction) directions with a diamond saw. The sectioned samples were then coated with Pt prior to SEM examination.

5.2.5.3 Permeability

Permeability measurements were performed on samples prepared by the DS and TDS configurations by measuring the flow rate of water under various pressure differences with a setup shown in Figure 5.2. This setup consisted of a water reservoir, a voltage-controlled pump, a pressure sensor (Omega PX409 pressure transducer, Omega Engineering, Stamford, CT, USA) and a balance. SiOC samples were machined with a core drill to a final diameter of 13 mm followed by cleaning by sonication in water. In order to prevent leakage from the sides of the samples during measurements, the perimeters of samples were enclosed by a low-shrinkage mounting compound (VariDur 3003, Buehler, Lake Bluff, IL, USA). After 24 hours of curing, the samples were then sectioned at 4.5 mm and 8.5 mm from the base, resulting in test samples with an approximate thickness of 4 mm. The samples were inserted and clamped inside a tube by a hose clamp to ensure no circumferential leakage. Once the pump was turned on and the pressure reached equilibrium, the mass change and flow rate were recorded. The pressure was gradually increased and a minimum of ten different pressures were applied, ranging from 5 to 85 kPa. The permeability was established from the Darcy-Forchheimer equation [124]:

$$\frac{\Delta P}{L} = \frac{\mu}{k_1} v + \frac{\rho}{k_2} v^2 \tag{5.2}$$

where ΔP is the pressure difference across the sample, L is the height of the sample, μ, v and ρ are the dynamic viscosity, flow velocity, and density of water, respectively, and k_1 and k_2 refer to the intrinsic and inertial permeability, respectively. Given the linearity of the collected data, k_2, which is associated with the non-linear portion of permeability and usually

observed only in gas flow, is omitted [56]. Three samples were tested for each condition and the average values with standard deviation were reported.
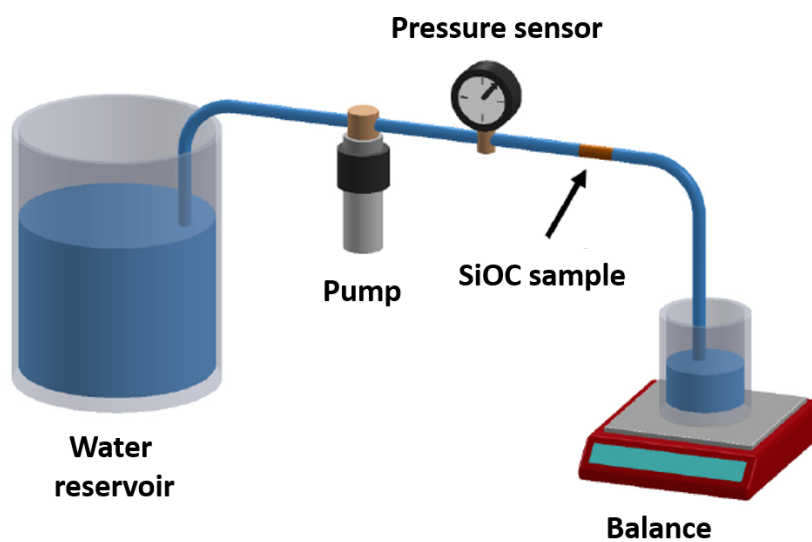
Figure 5.2 Schematic of the experimental setup used to measure permeability. Adapted from [2].

5.3 Results and Discussion

5.3.1 Effects of Freeze Casting Configuration on Freezing Behaviors of Solutions

Photo images showing freezing front profile of 20 wt% MK-TBA solutions with the three freeze casting configurations are presented in Figure 5.3. In Figure 5.3 (a), when the single-sided configuration is used to freeze the preceramic solution, uncontrolled crystal growth of TBA is observed, which results in an ill-defined freezing front. In contrast, in Figure 5.3 (b), a flat and well-defined freezing front that can be readily tracked is observed when the double-sided (DS) configuration is implemented. A similar freezing behavior is also found in the case of template-assisted double-sided (TDS) configuration, as shown in Figure 5.3 (c).
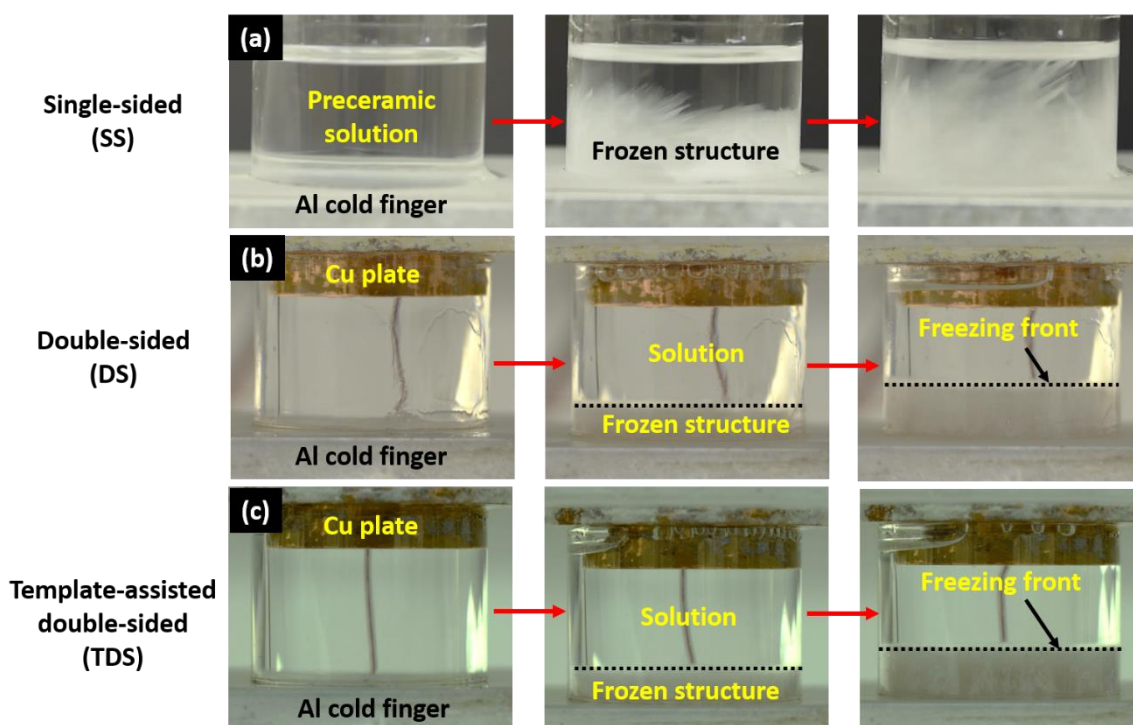
Figure 5.3 Photo images showing freezing front morphologies of MK-TBA solutions with (a) single-sided, (b) double-sided, and (c) template-assisted double-sided freeze casting configuration. Red arrows and black dotted lines indicate chronological order in freezing and flat, well-defined freezing fronts, respectively.

The freezing front in the case of SS freeze casting configuration is ill-defined, while the freezing front position in both cases of DS and TDS configurations is easily tracked. The latter are plotted as a function of freezing time in Figure 5.4. Both freezing fronts travel advance at a constant velocity of approximately 4.2 μm/s, which indicates that the templated substrate has little effect on freezing front velocity.
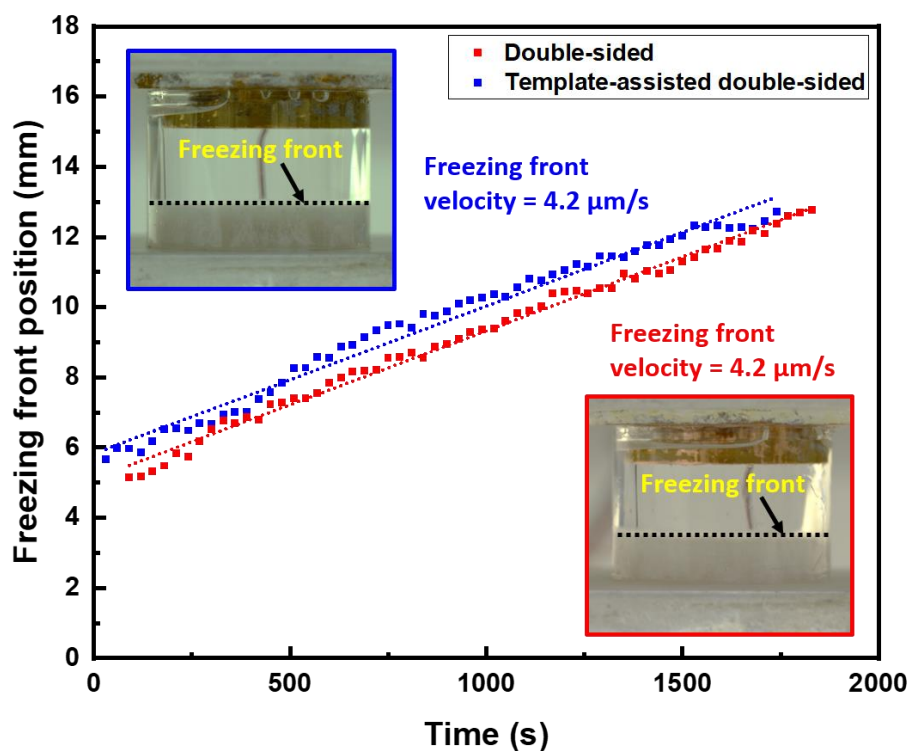
Figure 5.4 Freezing front position from the 20 wt% MK-TBA solution as a function of time obtained from images in Figure 5.3 (b) for double-sided configuration and images in Figure 5.3 (c) for template-assisted double-sided configuration. Associated R^2 values for both data sets exceed 0.99.

Figure 5.5 (a) shows a partial phase diagram of MK-TBA in which both the liquidus temperature (T_L) and freezing point (T_f) decrease with increasing preceramic polymer concentration. The freezing point of the solutions decreases at a higher rate than the liquidus temperature, which causes the disparity between T_L and T_f to become larger as preceramic polymer content increases. The great difference between T_L and T_f allows MK-TBA solutions to be cooled to a temperature T far below T_L without forming TBA crystals. The temperature difference between T_L and T is known as the supercooling [103]. It is this appreciable amount of supercooling in the 20 wt% MK-TBA solution ($> 10\ ^oC$) that gives rise to the uncontrolled freezing behavior seen in the SS configuration [2]. Once nucleation occurs, TBA crystals can quickly grow into the supercooled region, which leads to the ill-defined freezing front observed in Figure 5.3 (a).

The substantial change from an ill-defined freezing front in the SS configuration (Figure 5.3 (a)) to one that is well-defined in both DS and TDS configurations (Figure 5.3 (b) and (c)) can be explained by the reduced amount of supercooling due to the increased thermal gradient as a result of the heating Cu plate, as illustrated in Figure 5.5 (b). In Figure 5.5 (b), T(x) denotes the temperature of the solution as a function of position and T_L refers to the liquidus temperature of the solution. Supercooling is associated with the shaded region that lies between T_L and T(x). When there is no externally imposed thermal gradient in the solution (left figure in Figure 5.5 (b)), large supercooled region can form in the solution, as indicated by the shaded area. In contrast, with the additional heating of the Cu plate on top of the mold in both DS and TDS configurations, the thermal gradient along the mold height is increased, and hence the supercooled region is diminished (right figure in Figure 5.5 (b)) [26].
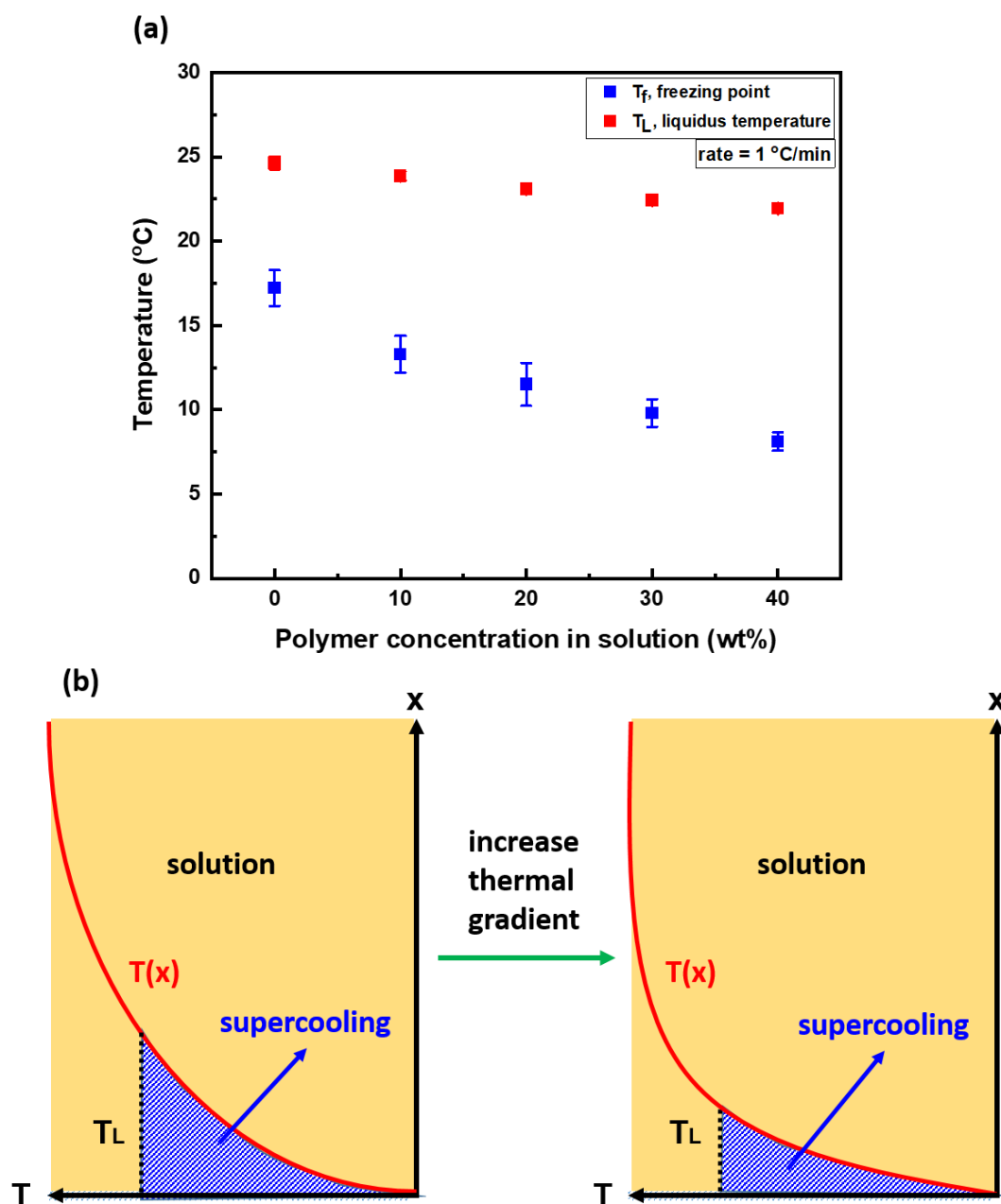
Figure 5.5 (a) Partial phase diagram of MK-TBA and (b) schematic showing diminished supercooling in the casting solution with increasing thermal gradient. $T(x)$ and T_L refer to the temperature of the solution as a function of position in the solution and liquidus temperature of the solution, respectively.

5.3.2 Effects of Freeze Casting Configuration on Pore Structures and Permeability

The porosity values of SiOC scaffolds fabricated by single-sided, double-sided, and template-assisted double-sided freeze casting configurations are tabulated in Table 5.1. All SiOC scaffolds show a porosity around 80%, which indicates that the freeze casting configuration has little effect on the porosity.

Table 5.1 Porosity values of SiOC scaffolds fabricated by single-sided, double-sided, and template-assisted double-sided freeze casting configurations.

Sample ID	Single-sided (SS)	Double-sided (DS)	Template-assisted double-sided (TDS)
Porosity (%)	81.4 ± 0.2	80.8 ± 0.5	81.4 ± 0.1

Figure 5.6 summarizes the longitudinal (parallel to the freezing direction) and transverse (perpendicular to the freezing direction) cross-sectional micrographs of SiOC scaffolds fabricated by single-sided, double-sided, and template-assisted double-sided freeze casting configurations. In the case of SS configuration (Figure 5.6 (a) and (b)), due to the uncontrolled crystal growth of TBA seen in Figure 5.3 (a), little pore alignment is observed and several large pores exceeding 200 μm are visible. A contrasting pore structure with better pore alignment is noted in the case of the DS configuration (Figure 5.6 (c) and (d)). From the longitudinal cross-section (Figure 5.6 (c)), in spite of the existence of pore domains with different pore orientations highlighted by the yellow dotted lines, improvement in pore alignment along the freezing direction is clearly observed. These images highlight pore alignment in each of the domains, but pore openings can be noted both in the longitudinal and transverse views (Figure 5.6 (c) and (d)). The enhancement in pore alignment from SS to DS configuration is ascribed to the increased thermal gradient provided by the upper heating Cu plate. The increased thermal gradient suppresses the uncontrolled TBA growth by reducing the supercooling in the solution, and hence, TBA freezes in a more controlled

fashion as observed in Figure 5.3 (b) and Figure 5.4. In addition, the increased thermal gradient from the Cu plate further guides the crystal growth along the direction of thermal gradient [16].

When the TDS configuration is implemented (Figure 5.6 (e) and (f)), further improvement in pore alignment is realized. From the longitudinal cross-section (Figure 5.6 (e)), vertical prismatic pores aligned with the freezing direction are observed without off-axis pore domains. Additionally, the improved pore alignment is manifested by the visibility of pore openings with no perception of off-axis pore domains from the transverse cross-section (Figure 5.6 (f)). This improvement in pore alignment from DS to TDS configuration is attributed to the templated Mylar film substrate which facilitates the crystal alignment during freezing by promoting multiple nucleation sites on the substrate. With multiple nucleation sites on the substrate, mutual impingement from neighboring nuclei promotes the nuclei to grow in the vertical direction by restricting their growth in the horizontal plane [125].
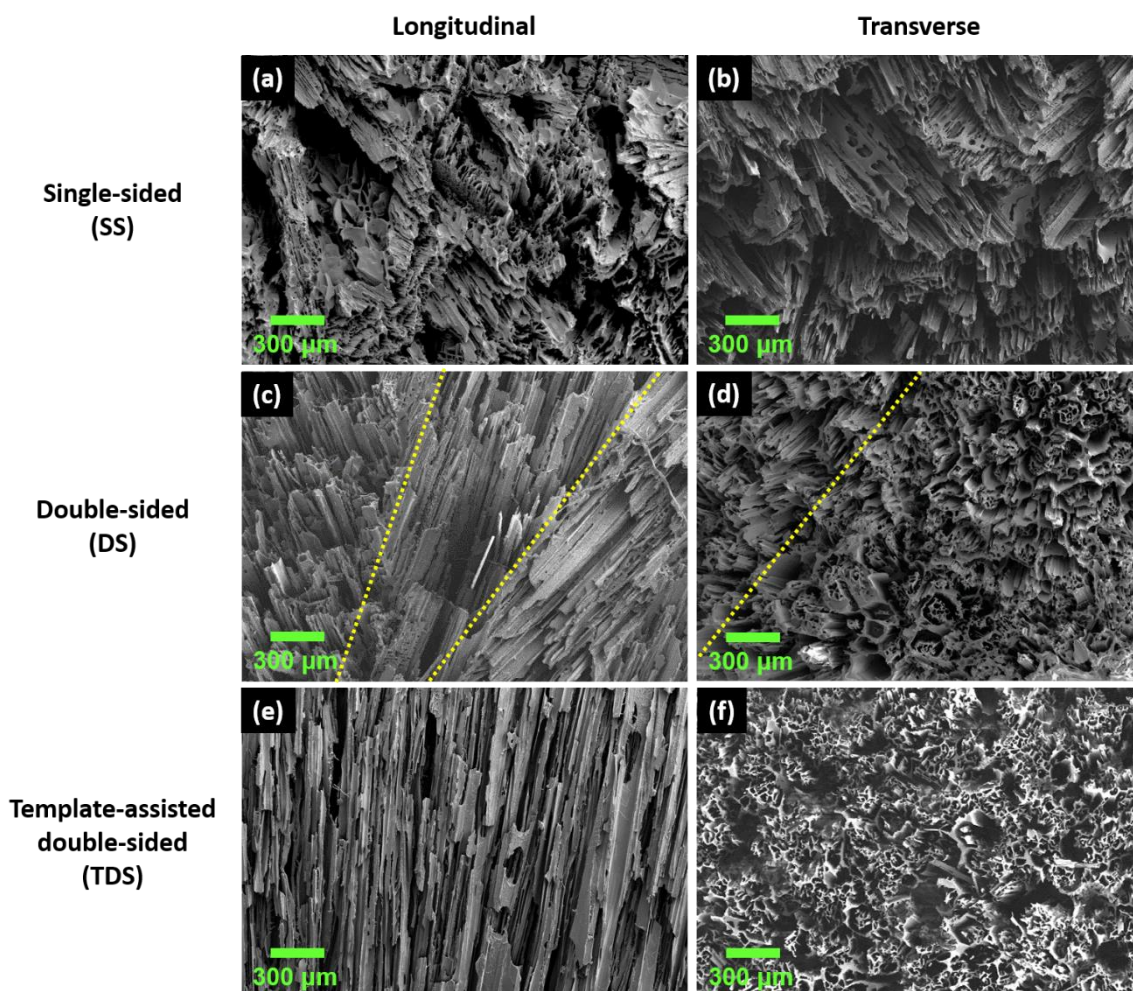
Figure 5.6 Longitudinal and transverse cross-sectional micrographs of SiOC scaffolds fabricated by (a)(b) single-sided, (c)(d) double-sided, and (e)(f) template-assisted double-sided freeze casting configurations. Yellow dotted lines denote the boundaries between pore domains with different orientations.

Figure 5.7 shows the pore size distribution obtained from mercury intrusion porosimetry of SiOC scaffolds produced by single-sided, double-sided, and template-assisted double-sided freeze casting configurations. It can be seen that the majority of pore diameters ranges from 20 to 40 μm in all three scaffolds. The scaffold fabricated by the SS configuration is found to contain some pores that exceed 200 μm, which is caused by uncontrolled TBA growth;

this is consistent with the micrographs shown in Figure 5.6 (a) and (b). In contrast, the percentage of pores greater than ~90 µm is found to decrease in the scaffolds made using the DS and TDS configurations. The reduction in large pore percentage is owing to the more controlled growth of TBA, which is attributed to the thermal gradient control in both DS and TDS configurations. Moreover, a further reduction in percentage of such pores is seen while comparing the scaffolds fabricated by the DS and TDS configurations. This further decline of the large pore population can also be attributable to crystal impingement caused by multiple nucleation sites due to the templated substrate. Crystal impingement restricts in-plane growth which not only promotes crystal alignment in the perpendicular orientation but also reduces the possibility of formation in these processing conditions of > 100 µm crystals, and hence, > 100 µm pores [125].
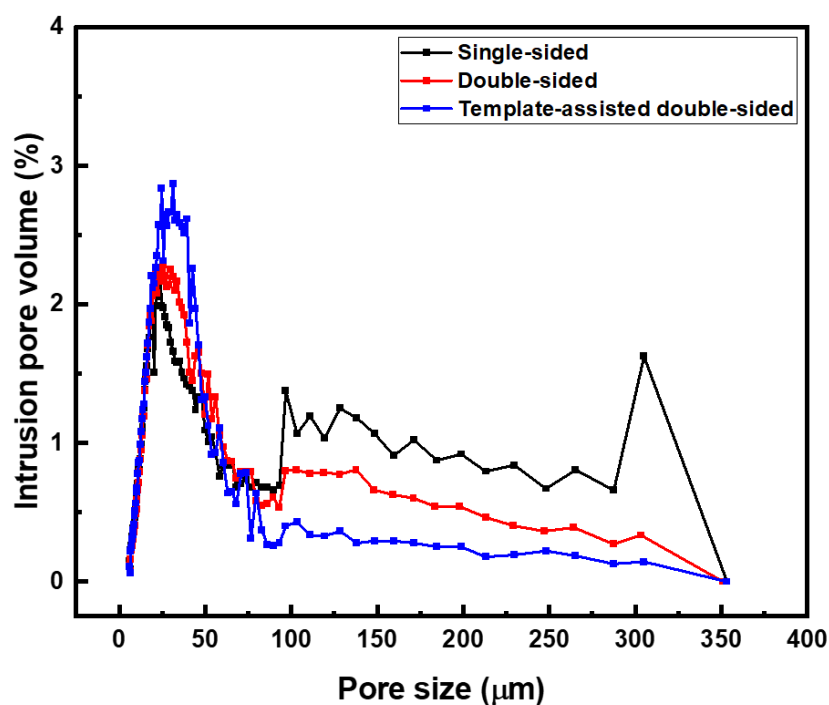
Figure 5.7 Pore size distribution obtained from mercury intrusion porosimeter of SiOC scaffolds fabricated by single-sided, double-sided, and template-assisted double-sided freeze casting configurations.

Given the size of pores present in the SiOC scaffold produced by single-sided freeze casting configuration and their lack of directionality, scaffolds made by the SS configuration are excluded from the permeability tests. Figure 5.8 presents water flow rate against pressure drop across a sample length of L from permeability measurements performed on SiOC scaffolds fabricated by double-sided and template-assisted double-sided freeze casting configurations. It is clear that the scaffolds fabricated by the TDS configuration are more permeable to water flow than those fabricated by the DS configuration. Furthermore, the linearity of the data sets confirms that the non-linear term for permeability in Equation 5.2, k_2, can be neglected.

Combining the pressure drop data in Figure 5.8 with dimensions of each permeability sample, the permeability constant, k_1, is calculated according to Equation 5.2 and shown in the inset of Figure 5.8. Although the scaffold fabricated by the DS configuration exhibits a higher percentage of large pores than that fabricated by the TDS configuration as shown in Figure 5.7, the latter shows more than eight-fold increase in permeability constant compared to the former (4.74×10^{-11} vs. 5.72×10^{-12} m^2). Given the similar porosity between the two scaffolds, this significant enhancement in permeability constant is attributed to the improvement in pore alignment observed in Figure 5.6, which provides shorter transport paths for water flow.
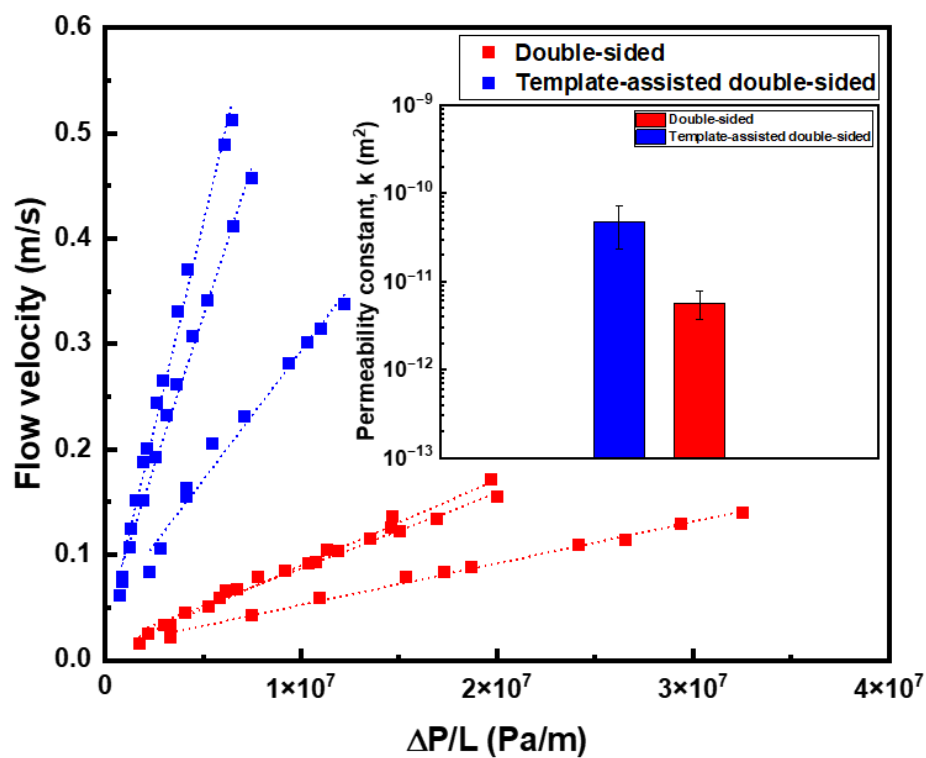
Figure 5.8 Water flow rate as a function of pressure drop for SiOC scaffolds fabricated by double-sided and template-assisted double-sided freeze casting configurations with corresponding permeability constants shown in the inset.

5.4 Conclusions

In this chapter, permeable SiOC scaffolds have been successfully fabricated by freeze casting a binary system of polymethylsiloxane preceramic polymer and tert-butyl alcohol (TBA) solvent. The effects of freeze casting configurations including single-sided (SS), double-sided (DS), and template-assisted double-sided (TDS) on the freezing behavior of polymethylsiloxane-TBA solutions and the resultant freeze-cast pore structures have been revealed. The uncontrolled growth of TBA in the case of SS configuration is a result of considerable supercooling in the solution, which leads to an ill-defined freezing front. While in the case of DS and TDS configuration, due to the increased thermal gradient caused by control of the thermal gradient with the heating Cu plate, the supercooling in the solutions is diminished, resulting in freezing in a more controlled manner, and hence, well-defined and trackable freezing fronts. Improvement in pore alignment of the resultant SiOC scaffolds is accompanied by the controlled freezing of TBA with the DS configuration. Moreover, pore alignment is further enhanced by templating the surface upon which crystallization begins, thus providing multiple nucleation sites. In addition, an eight-fold increase in water permeability is observed when the Mylar film substrate is templated. The application of DS configuration allows us to control the freezing of TBA and thus determine the freezing front velocity, an important processing parameter. The ability to regulate both thermal gradient and freezing front velocity opens up a new avenue to explore different pore structures in solutions with solvents that freeze in an uncontrolled fashion under the conventional single-sided freeze casting.

Chapter 6

SUMMARY, CONCLUSIONS, AND SUGGESTIONS FOR FUTURE WORK

6.1 Summary and Conclusions

This work has successfully demonstrated the versatility of freeze casting in fabricating porous materials used in distinct fields, ranging from polymer and composite separators in sodium ion batteries (SIBs) to permeable ceramic scaffolds.

Poly(vinylidene fluoride-co-hexafluoropropylene) (PVDF-HFP) was selected as the material for SIB separator fabrication due to its chemical inertness in the battery environment. Dioxane and dimethyl sulfoxide (DMSO) were chosen as the solvents for PVDF-HFP owing to their solubility of PVDF-HFP and the absence of liquid-liquid phase separation (LLPS) prior to the freezing of the solvents, which ensures that the freeze-cast pore morphology is produced by the directionally frozen solvent crystals. The tape/freeze-cast PVDF-HFP membranes were reinforced by Al_2O_3 and SiO_2 via suspension formation and a co-solvent method, respectively.

Apart from porosity and aligned pore structures to provide sufficient electrolyte uptake and non-tortuous ion transport paths, battery separators benefit from enhanced electrolyte affinity to reduce internal resistance, thermal stability and mechanical robustness to ensure cell safety. Therefore, an Al_2O_3 reinforcing agent was introduced through the formation of dioxane/Al_2O_3 suspensions via ball milling prior to mixing the suspensions with PVDF-HFP to form the PVDF-HFP/dioxane/Al_2O_3 casting suspensions. Although Al_2O_3 agglomeration was observed in the composite PVDF-HFP/Al_2O_3 membranes, the amount of added Al_2O_3 was found to have little effect on the freezing behavior of dioxane, and hence, the resultant pore morphology. The Al_2O_3 reinforcements resulted in a two-fold increase in the elastic modulus of the composite membranes (> 30 MPa vs. ~ 15 MPa) and improvement against thermal shrinkage compared to the pristine polymer membrane. Despite no obvious

enhancement in contact angles with added Al_2O_3, the composite membranes exhibited a nearly 60% (organic electrolyte) and 150% (ionic liquid) increase in electrolyte uptake along with higher ionic conductivities in both electrolytes than their polymer counterpart. This was attributed to the enhanced electrolyte affinity and higher amorphous polymer content with greater electrolyte retention capacity.

While the incorporation of oxide fillers as reinforcement can be achieved through suspension preparation via ball milling, stable and well-dispersed suspensions play a key role in producing composite membranes with high uniformity. As a result, a SiO_2 reinforcing agent was introduced through a co-solvent method in which tetraethoxysilane (TEOS) served as a co-solvent in conjunction with DMSO as well as the precursor of SiO_2 which forms via an ensuing sol-gel reaction of TEOS. Although the addition of TEOS caused liquid-liquid phase separation (LLPS) of the solution to occur before the freezing of DMSO when the co-solvent ratio of DMSO/TEOS $\geq$ 64/16, all of the membranes studied exhibited through-thickness and directionally aligned pore structures. The added SiO_2 particles functioned as stiffening inclusions to increase the elastic modulus of the PVDF-HFP/SiO_2 composite membranes (70~88 MPa vs. 50 MPa) and heat-resistant reinforcements for better thermal stability than the polymer membrane. Increased wettability in terms of contact angles and electrolyte uptake of both organic electrolyte and ionic liquid were a result of SiO_2 integration in the composite membranes. More importantly, enhancement in ionic conductivities in both electrolytes due to the introduced SiO_2 was accompanied by better rate performance in coin cells over its polymer counterpart.

Given that both the dioxane-based membranes (Chapter 3) and the DMSO-based membranes (Chapter 4) are considered promising SIBs separators as alternatives for filter papers, it is useful to compare the two systems in terms of their structures and properties.

Figure 6.1 compares the cross-sectional micrographs of the dioxane-based membranes (pure polymer membrane and composite membrane with 7 wt% Al_2O_3) and the DMSO-based membranes (PH20D80 and PH20D64T16) and the corresponding EDS maps of the two oxide-reinforced membranes (7 wt% Al_2O_3 and PH20D64T16). Although directionally-aligned pores are observed in all four membranes (Figure 6.1 (a), (b), (d), and (e)), it is clear that the pores are much smaller in the DMSO-based membranes (~ 2 to 4 μm in Figure 6.1 (d) and (e)) than the dioxane-based membranes (~ 10 μm in Figure 6.1 (a) and (b)). The pore size difference can be explained by (1) the lower processing temperature of the DMSO-based membranes with liquid nitrogen as the coolant compared to that of the dioxane-based membranes with a thermoelectric plate ~ -25 °C as the cooling source (2) Al substrates with higher thermal conductivity for the DMSO-based membranes in comparison with glass substrates with lower thermal conductivity for the dioxane-based membranes and (3) the thermally insulating air wedge introduced in the fabrication process of the dioxane-based membranes.

In terms of the distribution of the reinforcing oxides, Al_2O_3 agglomeration and non-uniform Al_2O_3 distribution are observed in the Al_2O_3-reinforced membrane prepared with the suspension method (Figure 6.1 (c)), while the co-solvent method with TEOS offers a more uniform distribution of SiO_2 across the PH20D64T16 membrane without perceptible agglomeration (Figure 6.1 (f)). Despite the extended ball milling procedure in the processing of the Al_2O_3-reinforced membranes, the presence of Al_2O_3 agglomeration is likely a result of the lack of effective anti-agglomeration mechanisms to prevent the re-agglomeration of nano-sized Al_2O_3 particles in the suspensions.

PVDF-HFP **PVDF-HFP with 7 wt% Al_2O_3** **PVDF-HFP with 7 wt% Al_2O_3**

(a) 10 μm (b) (c) Al signal

PH20D80 **PH20D64T16** **PH20D64T16**

(d) (e) (f) Si signal
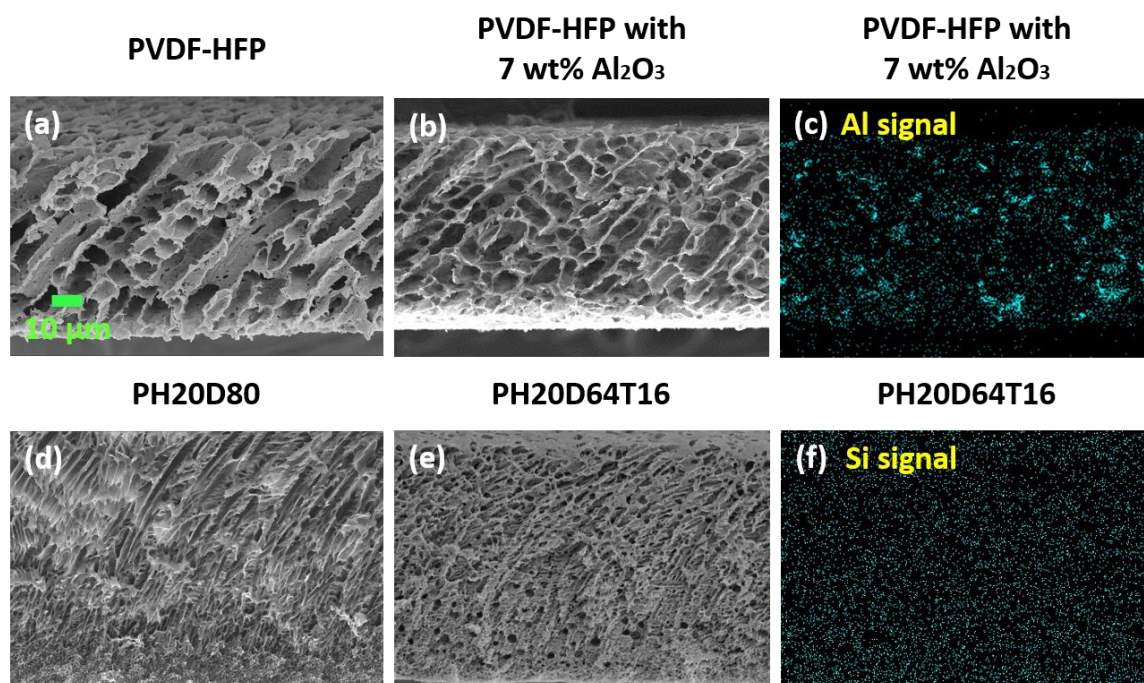
Figure 6.1 Cross-sectional micrographs of dioxane-based (a) polymer membrane (b) composite membrane with 7 wt% Al_2O_3 and (c) Al EDS mapping of (b); cross-sectional micrographs of DMSO-based (d) PH20D80 (e) PH20D64T16 and (f) Si EDS mapping of (e). All micrographs share the same scale bar.

Shown in Figure 6.2 is a comparison of mechanical properties including Young's modulus and tensile strength between the dioxane-based membranes and the DMSO-based membranes. The DMSO-based membranes exhibit greater stiffness and tensile strength compared to the dioxane-based counterparts. The main contributing factor to this difference in mechanical behavior is the porosity difference between the dioxane-based membranes (~ 87% porosity) and the DMSO-based membranes (~ 80% porosity) resulting from the different starting concentrations. Although the Al_2O_3 reinforcement in the dioxane-based membranes is four times stiffer than the SiO_2 reinforcement in the DMSO-based membranes [126, 127], the stiffening efficacy is not obvious in the Al_2O_3-reinforced membranes due to the existence of Al_2O_3 agglomerates. In addition, according to Zuo et al. [128], pore size is

also a contributing factor to tensile strengths of polymer membranes. As a result, the larger pore size in the dioxane-based membranes (Figure 6.1 (a) and (b)) compared to the smaller pore size in the DMSO-based membranes (Figure 6.1 (d) and (e)) is also responsible for such disparity in tensile strengths.
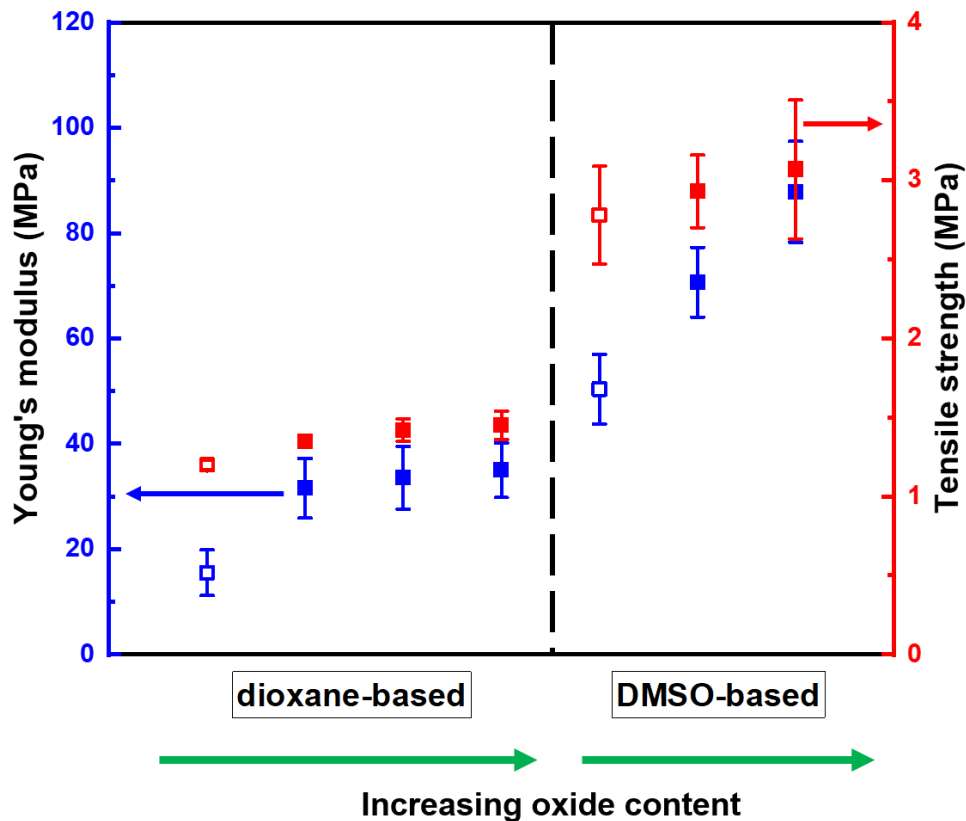
Figure 6.2 Comparison of Young's modulus and tensile strength between the dioxane-based membranes and the DMSO-based membranes. Solid legends represent the Al_2O_3-reinforced membranes in the dioxane-based membranes and the SiO_2-reinforced membranes in the DMSO-based membranes, while empty legends refer to the polymer membranes.

Figure 6.3 compares the electrolyte uptake and ionic conductivity between the dioxane-based membranes and the DMSO-based membranes in both organic electrolyte and ionic liquid. Due to the higher porosity of the dioxane-based membranes, they exhibit greater electrolyte uptake values compared to the DMSO-based membranes in both electrolytes. Generally speaking, the ionic conductivity of an electrolyte-infiltrated separator depends on the separator porosity, pore tortuosity, and wettability with the electrolyte. However, despite the higher amount of electrolyte retained in the dioxane-based membranes, especially in the Al_2O_3-reinforced membranes, no corresponding improvement in ionic conductivity is found in comparison with the DMSO-based membranes, let alone the SiO_2-reinforced membranes. It is hypothesized that Al_2O_3 agglomeration in the Al_2O_3-reinforced membranes fails to effectively enhance the wettability with the electrolyte in contrast to the evenly distributed SiO_2 particles in the SiO_2-reinforced membranes. The trend in reduced ionic conductivity with increased Al_2O_3 content is consistent with this hypothesis. In contrast, due to the uniformly distributed SiO_2, an increasing pattern of ionic conductivity with increasing SiO_2 content is found in the DMSO-based membranes.
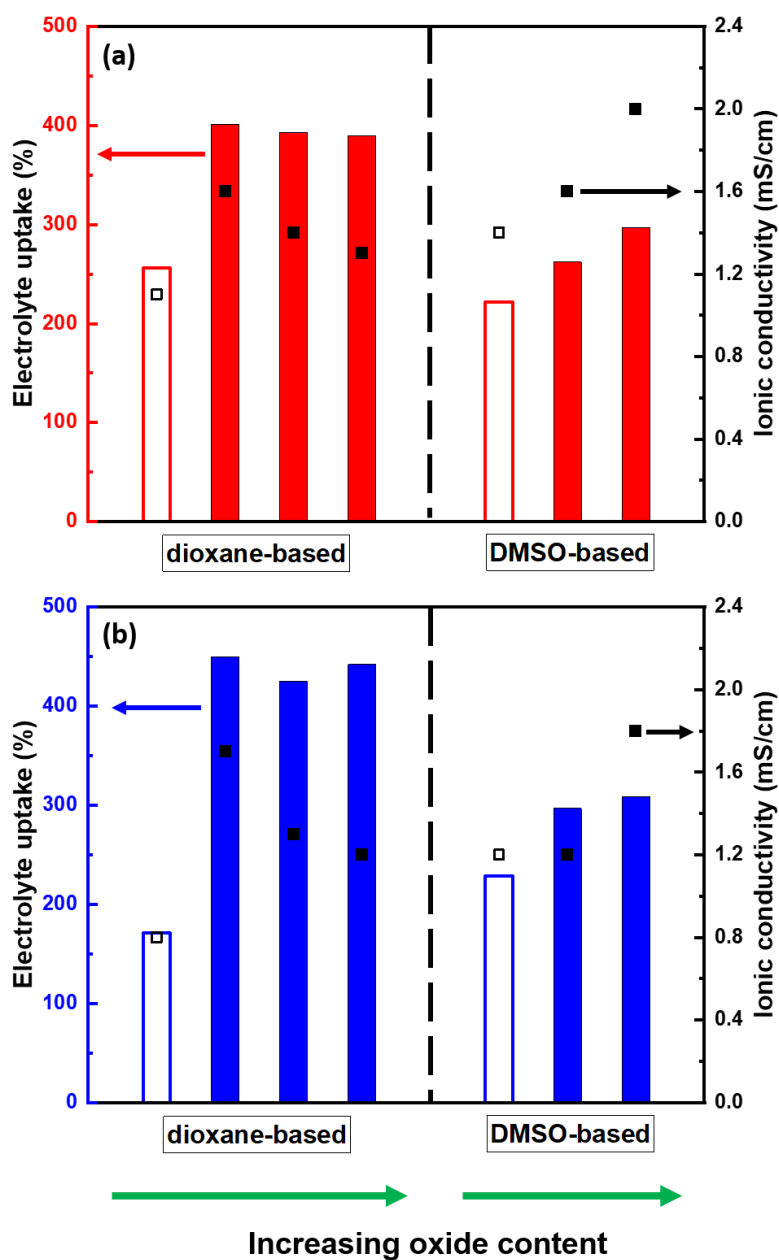
Figure 6.3 Comparison of electrolyte uptake and ionic conductivity between the dioxane-based membranes and the DMSO-based membranes in (a) organic electrolyte and (b) ionic liquid. Solid legends represent the Al_2O_3-reinforced membranes in the dioxane-based membranes and the SiO_2-reinforced membranes in the DMSO-based membranes, while empty legends refer to the un-reinforced polymer membranes.

Permeable silicon oxycarbide (SiOC) scaffolds were produced by freeze-casting solutions of polymethylsiloxane preceramic polymer (MK) and tert-butyl alcohol (TBA), since TBA is known to crystallize into prismatic crystals which result in prismatic pores with relatively high permeability. The conventional single-sided freeze casting configuration gave rise to the uncontrolled growth of TBA along with an ill-defined freezing front (Figure 6.4 (a)) due to considerable supercooling in the solution. Not surprisingly, the TBA crystals formed in this uncontrolled manner led to SiOC scaffolds with poor pore alignment (Figure 6.4 (d)). By increasing the thermal gradient in the solution with an additional heating Cu plate on top, a double-sided freeze casting configuration was constructed to diminish supercooling in the solution, which resulted in more controlled TBA growth and hence well-defined, trackable freezing fronts (Figure 6.4 (b)) and SiOC scaffolds with better pore alignment (Figure 6.4 (e)). In the template-assisted double-sided freeze casting configuration (Figure 6.4 (c)), further improvement in pore alignment (Figure 6.4 (f)) and an eight-fold increase in water permeability were achieved by using templated substrates that induced multiple nucleation sites and crystal impingement.

Single-sided   **Double-sided**   **Template-assisted double-sided**
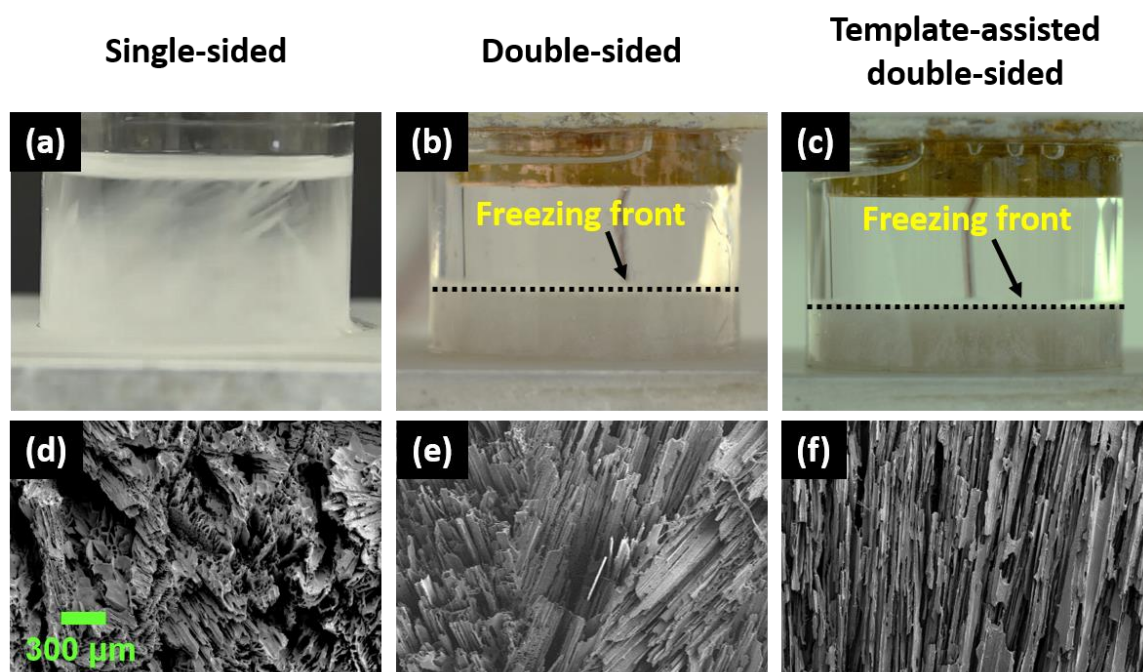
Figure 6.4 Comparison of freezing behavior of preceramic polymer-TBA solutions and corresponding SiOC scaffold pore morphology fabricated with (a)(d) single-sided (b)(e) double-sided (c)(f) template-assisted double-sided freeze casting configuration. All micrographs share the same scale bar.

6.2 Suggestions for Future Work

In Chapter 3, the presence of Al_2O_3 agglomerates in the Al_2O_3-reinforced composite membranes is likely due to the poor dispersion in the casting suspensions. From the perspective of oxide-reinforced membranes, an even and uniform distribution of oxide fillers across the membrane is of great importance; otherwise, the membrane properties would not be homogeneous. In order to produce oxide-reinforced membranes with high uniformity from suspensions, preparation of stable and well-dispersed suspensions is critical. Apart from the addition of a suitable dispersant and the usage of a high-energy sonication probe, surface modification of oxide particles [129, 130] is also found to be effective in creating well-dispersed suspensions. With stable suspensions, fabrication of oxide-reinforced membranes

with high uniformity via tape/freeze casting is feasible [37]. Besides direct observation through microscopy, contact angle measurements can also be utilized as an indicator of membrane homogeneity. In membranes with evenly distributed oxide reinforcements, a decreasing trend in contact angle with electrolytes with increasing oxide content should be observed due to the increase in effective hydrophilic area and hydroxyl group number as a result of the hydrophilic oxide particles [131]. While membranes with non-uniform oxide distributions or oxide agglomerates tend to show irregular patterns of contact angles with oxide content. Additionally, taking the rule of mixtures as a reference, well-distributed oxide reinforcements should provide greater stiffening efficacy to the membranes compared to the agglomerated oxides, since more oxide/polymer interfacial area which allows the applied loads to be transferred to the reinforcing oxide particles is present in the well-distributed case in contrast to the agglomerated case. Investigations should focus on the contact angle measurements.

The mechanical testing performed on the membranes in Chapter 3 and 4 provides us with the knowledge of their mechanical responses, including tensile strength, Young's modulus and strain-to-failure. However, these tests were conducted on dry and electrolyte-free membranes, which do not fully reflect the behavior of hydrated-membranes when they are soaked with electrolytes. Given that separators are infiltrated with electrolytes when used in batteries, understanding the mechanical responses of electrolyte-filled membranes is of great practical influence, and should be assessed. Chen et al. [132] and Kundu et al. [133] have shown that electrolytes have adverse effects on the mechanical properties of membrane separators such as Young's modulus and yield strength. In order to evaluate the mechanical performance of electrolyte-filled membranes, dry membranes would first be immersed in specific electrolytes to obtain electrolyte-infiltrated membranes, and the electrolyte-filled membranes would then be tested following the same mechanical testing procedure as dry membranes.

In Chapter 3 and 4, one of the reasons why the oxide-reinforced composite membranes exhibit greater electrolyte uptake compared to their polymer counterpart is the higher amount of amorphous polymer phase in the composite membranes. Due to the larger free volume of

the amorphous phase than the crystalline phase, the amorphous phase shows higher electrolyte retention capacity [134, 135]. Crystallinity of a polymer membrane can be obtained experimentally by performing differential scanning calorimetry (DSC). The degree of crystallinity in a membrane sample can be acquired by calculating the ratio of the enthalpy of melting of the membrane sample to the enthalpy of melting of a pure crystalline reference sample [135]. In addition to electrolyte retention capacity, the crystallinity of a polymer membrane also affects its mechanical properties, where a crystalline phase is known to exhibit higher strength and elastic modulus while an amorphous phase shows the opposite [134, 135]. With the knowledge of crystallinity in both the polymer and oxide-reinforced composite membranes, the effects of reinforcing oxide fillers on the membrane mechanical properties can be assessed more accurately.

For ceramic scaffolds discussed in Chapter 5, it was demonstrated that by manipulating the thermal gradient in the solutions of preceramic polymer and tert-butyl alcohol (TBA) with a double-sided freeze casting configuration, the freezing of TBA can be controlled such that the freezing front velocity is stable across the casting. With the ability to regulate both thermal gradient and freezing front velocity, the two dominant processing factors in the microstructure selection map, Arai et al. [26] have shown that different pore structures can be realized from the same preceramic polymer/cyclohexane solution system. The use of a double-sided freeze casting configuration opens a new avenue to explore different pore structures using solvents such as TBA, camphene and p-xylene that freeze in an uncontrolled manner under the conventional single-sided freeze casting [2].

Preliminary results of post-freeze-casting infiltration process, high-temperature freeze casting, and cellulose-based and polyimide membranes can be found in the appendices.

REFERENCES

[1] Maninput Naviroj, Peter W. Voorhees, and Katherine T. Faber. Suspension- and solution-based freeze casting for porous ceramics. Journal of Materials Research, 32(17):3372-3382, 2017. ISSN 0884-2914. doi: 10.1557/jmr.2017.133.

[2] Maninput Naviroj. Silicon-based porous ceramics via freeze-casting of preceramic polymers. PhD thesis, Northwestern University, 2017.

[3] Leiming Yan, Jisi Wu, Lei Zhang, Xinli Liu, Kechao Zhou, and Bo Su. Pore structures and mechanical properties of porous titanium scaffolds by bidirectional freeze casting. Materials Science and Engineering C, 75:335-340, 2017. ISSN 0928-4931. doi:10.1016/j.msec.2016.12.044.

[4] Yasumasa Chino and David C. Dunand. Directionally freeze-cast titanium foam with aligned, elongated pores. Acta Materialia, 56(1):105-113, 2008. ISSN 1359-6454. doi:10.1016/j.actamat.2007.09.002.

[5] Ranier Sepulveda, Amelia A. Plunk, and David C. Dunand. Microstructures of Fe_2O_3 scaffolds created by freeze-casting and sintering. Materials Letters, 142:56-59, 2015. ISSN 0167-577X. doi:10.1016/j.matlet.2014.11.155.

[6] Hyungyung Jo, Min Jeong Kim, Hyelim Choi, Yung-Eun Sung, Heenam Choe, and David C. Dunand. Morphological study of directionally freeze-cast nickel foams. Metallurgical and Materials Transactions E, 3(1):46-54, 2016. doi:10.1007/s40553-016-0068-y.

[7] Haifei Zhang, Irshad Hussain, Mathias Brust, Michael F. Butler, Steven P. Rannard, and Andrew I. Cooper. Aligned two- and three-dimensional structures by directional freezing of polymers and nanoparticles. Nature Materials, 4(10):787-793, 2005. doi:10.1038/nmat1487.

[8] Jin-Woong Kim, Kentaro Taki, Shinsuke Nagamine, and Masahiro Ohshima. Preparation of porous poly(L-lactic acid) honeycomb monolith structure by phase separation and unidirectional freezing. Langmuir, 25(9):5304-5312, 2009. doi:10.1021/la804057e.

[9] Yan Zhang, Chris R. Bowen, and Sylvain Deville. Ice-templated poly(vinylidene fluoride) ferroelectrets. Soft Matter, 15:825-832, 2019. ISSN 1744-6848. doi:10.1039/c8sm02160k.

[10] Jihoon Lee and Yulin Deng. The morphology and mechanical properties of layer structured cellulose microfibril foams from ice-templating methods. Soft Matter, 7:6034-6040, 2011. ISSN 1744-6848. doi:10.1039/c1sm05388d.

[11] Hehao Chen, Xiaofeng Wang, Fengdan Xue, Yujuan Huang, Kechao Zhou, and Dou Zhang. 3D printing of SiC ceramic: direct ink writing with a solution of preceramic polymers. Journal of the European Ceramic Society, 38(16):5294-5300, 2018. ISSN 0955-2219. doi:10.1016/j.jeurceramsoc.2018.08.009.

[12] Jun Yoshikawa, Jennifer A. Lewis, and Byong-Wa Chun. Comb polymer architecture, ionic strength, and particle size effects on the $BaTiO_3$ suspension stability. Journal of the American Ceramic Society, 92(S1):S42-S49, 2009. ISSN 0002-7820. doi:10.1111/j.1551-2916.2008.02647.x.

[13] Sylvain Deville. Freeze-casting of porous ceramics: a review of current achievements and issues. Advanced Engineering Materials, 10(3):155-169, 2008. ISSN 1438-1656. doi:10.1002/adem.200700270.

[14] Issac Nelson and Steven E. Naleway. Intrinsic and extrinsic control of freeze casting. Journal of Materials Research and Technology, 8(2):2372-2385, 2019. ISSN 2238-7854. doi:10.1016/j.jmrt.2018.11.011.

[15] K.A. Jackson, D.R. Uhlmann, and J.D. Hunt. On the nature of crystal growth from the melt. Journal of Crystal Growth, 1(1):1-36, 1967. doi:10.1016/0022-0248(67)90003-6.

[16] Sylvain Deville, Eduardo Saiz, and Antoni P. Tomsia. Ice-templated porous alumina structures. Acta Materialia, 55(6):1965-1974, 2007. ISSN 1359-6454. doi:10.1016/j.actamat.2006.11.003.

[17] Etienne Munch, Eduardo Saiz, Antoni P. Tomsia, and Sylvain Deville. Architectural control of freeze-cast ceramics through additives and templating. Journal of the American Ceramic Society, 92(7):1534-1539, 2009. ISSN 0002-7820. doi:10.1111/j.1551-2916.2009.03087.x.

[18] Michael M. Porter, Russ Imperio, Matthew Wen, Marc A. Meyers, and Joanna McKittrick. Bioinspired scaffolds with varying pore architectures and mechanical properties. Advanced Functional Materials, 24:1978-1987, 2014. ISSN 1616-301X. doi:10.1002/adfm.201302958.

[19] Yan Zhang, Kechao Zhou, Yinxiang Bao, and Dou Zhang. Effects of rheological properties on ice-templated porous hydroxyapatite ceramics. Materials Science and Engineering C, 33:340-346, 2013. ISSN 0928-4931. doi:10.1016/j.msec.2012.08.048.

[20] Kai Hui Zuo, Yu-Ping Zeng, and Dongliang Jiang. Effect of polyvinyl alcohol additive on the pore structure and morphology of the freeze-cast hydroxyapatite ceramics. Materials Science and Engineering C, 30:283-287, 2010, ISSN 0928-4931. doi:10.1016/j.msec.2009.11.003.

[21] Min Kyung Lee and Jonghwi Lee. Mimicking permafrost formation for the preparation of porous polymer membranes. Polymer, 74:176-181, 2015. ISSN 0032-3861. doi:10.1016/j.polymer.2015.08.014.

[22] Byoung Soo Kim and Jonghwi Lee. Pore size reduction in directional crystallization processing of porous polymeric membranes. Journal of Nanoscience and Nanotechnology, 13(3):2276-2283, 2013. doi:10.1166/jnn.2013.7096.

[23] Hong-Qing Liang, Qing-Yun Wu, Ling-Shu Wan, Xiao-Jun Huang, and Zhi-Kang Xu. Thermally induced phase separation followed by in situ sol-gel process: a novel method for $PVDF/SiO_2$ hybrid membranes. Journal of Membrane Science, 465:56-67, 2014. ISSN 0376-7388. doi:10.1016/j.memsci.2014.3.068.

[24] Sindo Kou. Welding Metallurgy. Wiley, Hoboken, NJ, USA, 2002. ISBN 0471434914. doi:10.1002/0471434027.

[25] Xiaomei Zeng, Noriaki Arai, and Katherine T. Faber. Robust cellular shape-memory ceramics via gradient-controlled freeze casting. Advanced engineering Materials, 21(12):1900398, 2019. ISSN 1438-1656. doi:10.1002/adem.201900398.

[26] Noriaki Arai and Katherine T. Faber. Gradient-controlled freeze casting of preceramic polymers. Journal of the European Ceramic Society, 43(5):1904-1911, 2023. ISSN 0955-2219. doi:10.1016/j.jeurceramsoc.2022.12.016.

[27] Thomas Waschkies, Rainer Oberacker, and Michael J. Hoffmann. Control of lamellae spacing during freeze casting of ceramics using double-sided cooling as a novel processing route. Journal of the American Ceramic Society, 92(S1):S79-S84, 2009. ISSN 0002-7820. doi:10.1111/j.1551-2916.2008.02673.x.

[28] Frances Y. Su, Joyce R. Mok, and Joanna McKittrick. Radial-concentric freeze casting inspired by porcupine fish spines. Ceramics, 2(1):161-179, 2019. doi:10.3390/ceramics2010015.

[29] Hao Bai, Yuan Chen, Benjamin Delattre, Antoni P. Tomsia, and Robert O. Ritchie. Bioinspired large-scale aligned porous materials assembled with dual

temperature gradients. <u>Science Advances</u>, 1(11):e1500849, 2015. eISSN 2375-2548. doi:10.1126/sciadv.1500849.

[30] Jiecai Han, Luyang Hu, Yumin Zhang, and Yufeng Zhou. Fabrication of ceramics with complex porous structures by the impregnate-freeze-casting process. <u>Journal of the American Ceramic Society</u>, 92(9):2165-2167, 2009. ISSN 0002-7820. doi:10.1111/j.1551-2916.2009.03168.x.

[31] Maninpat Naviroj, Melody M. Wang, Matthew T. Johnson, and Katherine T. Faber. Nucleation-controlled freeze casting of preceramic polymers for uniaxial pores in Si-based ceramics. <u>Scripta Materialia</u>, 130(15):32-36, 2017. ISSN 1359-6462. doi:10.1016/j.scriptamat.2016.10.038.

[32] Michael M. Porter, Michael Yeh, James Strawson, Thomas Goehring, Samuel Lujan, Philip Siripasopsotorn, Marc A. Meyers, and Joanna McKittrick. Magnetic freeze casting inspired by nature. <u>Materials Science and Engineering: A</u>, 556(30):741-750, 2012. ISSN 0921-5093. doi:10.1016/j.msea.2012.07.058.

[33] Yumin Zhang, Luyang Hu, and Jiecai Han. Preparation of a dense/porous bilayered ceramic by applying an electric field during freeze casting. <u>Journal of the American Ceramic Society</u>, 92(8):1874-1876, 2009. ISSN 0002-7820. doi:10.1111/j.1551-2916.2009.03110.x.

[34] Stephen W. Sofie. Fabrication of functionally graded and aligned porosity in thin ceramic substrates with the novel freeze-tape-casting process. <u>Journal of the American Ceramic Society</u>, 90(7):2024-2031, 2007. ISSN 0002-7820. doi:10.1111/j.1551-2916.2007.01720.x.

[35] Linlin Ren, Yu-Ping Zeng, and Dongliang Jiang. Fabrication of gradient pore TiO$_2$ sheets by a novel freeze-tape-casting process. <u>Journal of the American Ceramic Society</u>, 90(9):3001-3004, 2007. ISSN 0002-7820. doi:10.1111/j.1551-2916.2007.01833.x.

[36] Byoung Soo Kim, Min Kyung Lee, and Jonghwi Lee. Large-area PVDF membranes with through-thickness porosity prepared by uni-directional freezing. <u>Macromolecular Research</u>, 21(2):194-201, 2013. ISSN 1598-5032. doi:10.1007/s13233-013-1020-y.

[37] Byoung Soo Kim and Jonghwi Lee. Macroporous PVDF/TiO$_2$ membranes with three-dimensionally interconnected pore structures produced by directional melt crystallization. <u>Chemical Engineering Journal</u>, 301:158-165, 2016. ISSN 1385-8947. doi:10.1016/j.cej.2016.05.003.

[38] Andrea del Pilar Sanchez-Camargo, Monica Bueno, Fabian Parada-Alfonso, Alejandro Cifuentes, and Elena Ibanez. Hansen solubility parameters for

selection of green extraction solvents. Trends in Analytical Chemistry, 118:227-237, 2019. ISSN 0165-9936. doi:10.1016/j.trac.2019.05.046.

[39] Emmanuel Stefanis and Costas Panayiotou. Prediction of Hansen solubility parameters with a new group-contribution method. International Journal of Thermophysics, 29:568-585, 2008. doi:10.1007/s10765-008-0415-z.

[40] Charles M. Hansen. Hansen solubility parameters: a user's handbook. CRC Press Boca Raton, 2000. ISBN 9780429127526. doi:10.1201/9781420006834.

[41] David Fairhurst, Ravi Sharma, Shin-ichi Takeda, Terence Cosgrove, and Stuart W. Prescott. Fast NMR relaxation, powder wettability and Hansen solubility parameter analyses applied to particle dispersibility. Powder Technology, 377(2):545-552, 2021. ISSN 0032-5910. doi:10.1016/j.powtec.2020.09.002.

[42] J.H. Aubert and R.L. Clough. Low-density, microcellular polystyrene foams. Polymer, 26(13):2047-2054. ISSN 0032-3861. doi:10.1016/0032-3861(85)90186-7.

[43] S. Gay, G. Lefebvre, M. Bonnin, B. Nottelet, F. Boury, A. Gibaud, and B. Calvignac. PLA scaffolds production from thermally induced phase separation: effect of process parameters and development of an environmentally improved route assisted by supercritical carbon dioxide. The Journal of Supercritical Fluids, 136:123-135, 2018. ISSN 0896-8446. doi:10.1016/j.supflu.2018.02.015.

[44] Ying Cui, Huaxin Gong, Yujie Wang, Dewen Li, and Hao Bai. A thermally insulating textile inspired by polar bear hair. Advanced Materials, 30(14):1706807, 2018. ISSN 0935-9648. doi:10.1002/adma.201706807.

[45] Bernd Wicklein, Andraz Kocjan, German Salazar-Alvarez, Federico Carosio, Giovanni Camino, Markus Antonietti, and Lennart Bergstrom. Thermally insulating and fire-retardant lightweight anisotropic foams based on nanocellulose and graphene oxide. Nature Nanotechnology, 10:277-283, 20015. doi:10.1038/nnano.2014.248.

[46] Yuyang Qin, Qingyu Peng, Yujie Ding, Zaishan Lin, Chunhui Wang, Ying Li, Fan Xu, Jianjun Li, Ye Yuan, Xiaodong He, and Yibin Li. Lightweight, superelastic, and mechanically flexible graphene/polyimide nanocomposite foam for strain sensor application. ACS Nano, 9(9):8933-8941, 2015. doi:10.1021/acsnano.5b02781.

[47] Zhihui Zeng, Xiu Yun Daphne Ma, Youfang Zhang, Zhe Wang, Bing Feng Ng, Man Pun Wan, and Xuehong Lu. Robust lignin-based aerogel filters: high-efficiency capture of ultrafine airborne particulates and the mechanism. ACS

Sustainable Chemistry & Engineering, 7(7):6959-6968, 2019. doi:10.1021/acssuschemeng.8b06567.

[48] Yang Si, Qiuxia Fu, Xueqin Wang, Jie Zhu, Jianyong Yu, Gang Sun, and Bin Ding. Superelastic and superhydrophobic nanofiber-assembled cellular aerogels for effective separation of oil/water emulsions. ACS Nano, 9(4):3791-3799, 2015. doi:10.1021/nn506633b.

[49] Hongli Cai, Sudhir Sharma, Wenying Liu, Wei Mu, Wei Liu, Xiaodan Zhang, and Yulin Deng. Aerogel microspheres from natural cellulose nanofibrils and their application as cell culture scaffold. Biomacromolecules, 15(7):2540-2547, 2014. doi:10.1021/bm5003976.

[50] Hajar Maleki, Mohammad-Ali Shahbazi, Susan Montes, Seyed Hojjat Hosseini, Mohammad Reza Eskandari, Stefan Zaunschirm, Thomas Verwanger, Sanjay Mathur, Barbara Milow, Barbara Krammer, and Nicola Husing. Mechanically strong silica-silk fibroin bioaerogel: a hybrid scaffold with ordered honeycomb micromorphology and multiscale porosity for bone regeneration. ACS Applied Materials Interfaces, 11(19):17256-17269, 2019. doi:10.1021/acsami.9b04283.

[51] Zedong Zhao, Minqiang Sun, Wuji Chen, Yao Liu, Long Zhang, Nanchen Dongfang, Yingbo Ruan, Jiajia Zhang, Peng Wang, Lei Dong, Yongyao Xia, and Hongbin Lu. Sandwich, vertical channeled thick electrodes with high rate and cycle performance. Advanced Functional Materials, 29(16):1809196, 2019. ISSN 1616-301X. doi:10.1002/adfm.201809196.

[52] Kewei Shu, Caiyun Wang, Sha Li, Chen Zhao, Yang Yang, Huakun Liu, and Gordon Wallace. Flexible free-standing graphene paper with interconnected porous structure for energy storage. Journal of Materials Chemistry A, 3(8):4428-4434, 2015. doi:10.1039/c4ta04324c.

[53] Zhong-Li Wang, Dan Xu, Heng-Guo Wang, Zhong Wu, and Xin-Bo Zhang. In situ fabrication of porous graphene electrodes for high-performance energy storage. ACS Nano, 7(3):2422-2430, 2013. doi:10.1021/nn3057388.

[54] Marija Kirchhöfer, Jan von Zamory, Elie Paillard, and Stefano Passerini. Separators for Li-ion and Li-metal battery including ionic liquid based electrolytes based on the TFSI⁻ and FSI⁻ anions. International Journal of Molecular Sciences, 15(8):14868-14890, 2014. ISSN 1422-0067. doi:10.3390/ijms.150814868.

[55] C. T. Kuo and K. T. Faber. Permeable carbon nanotube-reinforced silicon oxycarbide via freeze vesting with enhanced mechanical stability. Journal of the European Ceramic Society, 40(6):2470-2479, 2020. ISSN 955-2219. doi:10.1016/j.jeurceramsoc.2019.12.059.

[56] Taijung Kuo, Lisa M. Rueschhoff, Matthew B. Dickerson, Tulsi A. Patel, and Katherine T. Faber. Hierarchical porous SiOC via freeze casting and self-assembly of block copolymers. Scripta Materialia, 191:204-209, 2021. ISSN 1359-6462. doi: 10.1016/j.scriptamat.2020.09.042.

[57] Vatsal Shah, Bo Wang, and Kang Li. Blending modification to porous polyvinylidene fluoride (PVDF) membrane prepared via combined crystallization and diffusion (CCD) technique. Journal of Membrane Science, 618:118708, 2021. ISSN 0376-7388. doi: 10.1016/j.memsci.2020.118708.

[58] Hong-Qing Liang, Ke-Jia Ji, Li-Yun Zha, Wen-Bing Hu, Yang Ou, and Zhi-Kang Xu. Polymer membranes with vertically oriented pores constructed by 2D freezing at ambient temperature. ACS Applied Materials & Interfaces, 8(22):14174-14181, 2016. doi: 10.1021/acsami.6b03071.

[59] Chang-Yu Hsu, Ren-Jun Liu, Chun-Han Hsu, and Ping-Lin Kuo. High thermal and electrochemical stability of PVDF-graft-PAN copolymer hybrid PEO membrane for safety reinforced lithium-ion battery. RSC Advances, 6:18082-18088, 2016. doi:10.1039/c5ra26345j.

[60] Ming Xiong, Haolin Tang, Yadong Wang, Yu Lin, Meiling Sun, Zhuangfei Yin, and Mu Pan. Expanded polytetrafluoroethylene reinforced polyvinylidenefluoride-hexafluoropropylene separator with high thermal stability for lithium-ion batteries. Journal of Power Sources, 241:203-211, 2014. ISSN 0378-7753. doi:10.1016/j.jpowsour.2013.04.064.

[61] Boor Singh Lalia, Yarjan Abdul Samad, and Raed Hashaikeh. Nanocrystalline cellulose-reinforced composite mats for lithium-ion batteries: electrochemical and thermomechanical performance. Journal of Solid State Electrochemistry, 17:575-581, 2013. doi:10.1007/s10008-012-1894-1.

[62] Lei Li, Miao Yu, Chao Jia, Jianxin Liu, Yanyan Lv, Yanhua Liu, Yi Zhou, Chuanting Liu, and Ziqiang Shao. Cellulosic biomass-reinforced polyvinylidene fluoride separators with enhanced dielectric properties and thermal tolerance. ACS Applied Materials Interfaces, 9(24):20885-20894, 2017. doi:10.1021/acsami.7b04948.

[63] Marco Bolloli, Claire Antonelli, Yannick Molméret, Fannie Alloin, Cristina Iojoiu, and Jena-Yves Sanchez. Nanocomposite poly(vynilidene fluoride)/nanocrystalline cellulose porous membranes as separators for lithium-ion batteries. Electrochimica Acta, 214:38-48, 2016. ISSN 0013-4686. doi:10.1016/j.electacta.2016.8.020.

[64] Junchen Liu, Kai Yang, Yudi Mo, Shuanjin Wang, Dongmei Han, Min Xiao, and Yuezhong Meng. Highly safe lithium-ion batteries: high strength separator

from polyformaldehyde/cellulose nanofibers blend. Journal of Power Sources, 400:502-510, 2018. ISSN 0378-7753. doi:10.1016/j.jpowsour.2018.08.043.

[65] Tianming Zhu, Xiaoxi Zuo, Yawen Li, Lengdan Zhang, Dongming Xie, Xin Xiao, Jiansheng Liu, and Junmin Nan. A novel membrane based on cellulose acetate nanofibers with a ZrO_2 reinforce201808ment layer for advanced sodium-ion batteries. Journal of Membrane Science, 620:118917, 2021. ISSN 0376-7388. doi:10.1016/j.memsci.2020.118917.

[66] Min Kim and Jong Hyeok Park. Inorganic thin layer coated porous separator with high thermal stability for safety reinforced Li-ion battery. Journal of Power Sources, 212:22-27, 2012. ISSN 0378-7753. doi:10.1016/j.jpowsour.2012.03.038.

[67] Nanxi Dong, Jie Wang, Guofeng Tian, Shengli Qi, Guohua Sun, and Dezhen Wu. Inorganic-shell reinforcement: TiO_2-coated polyimide nanofibers membrane as advanced separator for lithium-ion batteries. Journal of the Electrochemical Society, 167:160560, 2020. ISSN 1945-7111. doi:10.1149/1945-7111/abd60a.

[68] Nanxi Dong, Jie Wang, Nanjun Chen, Bingxue Liu, Guofeng Tian, Shengli Qi, Guohua Sun, and Dezhen Wu. In situ reinforcing: ZrO_2-armored hybrid polyimide separators for advanced and safe lithium-ion batteries. ACS Sustainable Chemistry & Engineering, 9(18):6250-6257, 2018. doi:10.1021/acssuschemeng.0c08818.

[69] Xiaosung Huang. A facile approach to make high performance nano-fiber reinforced composite separator for lithium ion batteries. Journal of Power Sources, 323:17-22, 2016. ISSN 0378-7753. doi:10.1016/j.jpowsour.2016.05.022.

[70] A. Bottino, G. Capannelli, S. Munari, and A. Turturro. Solubility parameters of poly(vinylidene fluoride). Journal of Polymer Science: Part B: Polymer Physics, 26(4):785-794, 1988. doi: 10.1002/polb.1988.090260405.

[71] Kuppan Saravanan, Chad W. Mason, Ashish Rudola, Kim Hai Wong, and Palani Balaya. The first report on excellent cycling stability and superior rate capability of NVP for sodium ion batteries. Advanced Energy Materials, 3(4):444-450, 2013. ISSN 1614-6832. doi:10.1002/aenm.201200803.

[72] Huang Zhang, Bingsheng Qin, Daniel Buchholz, and Stefano Passerini. High-efficiency sodium-ion battery based on NASICON electrodes with high power and long lifespan. ACS Applied Energy Materials, 1(11):6425-6432, 2018. doi:10.1021/acsaem.8b01390.

[73] Ashish Rudola, Doron Aurbach, and Palani. Balaya. A new phenomenon in sodium batteries: voltage step due to solvent interaction. Electrochemistry Communications, 46:56-59, 2014. ISSN 1388-2481. doi:10.1016/j.elecom.2014.06.008.

[74] Xiaolong Lu and Xianfeng Li. Preparation of polyvinylidene fluoride membrane via a thermally induced phase separation using a mixed diluent. Journal of Applied Polymer Science, 114(2):1213-1219, 2009. doi:10.1002/app.30184.

[75] Junchen Liu, Kai Yang, Yudi Mo, Shuanjin Wang, Dongmei Han, Min Xiao, and Yuezhong Meng. Highly safe lithium-ion batteries: high strength separator from polyformaldehyde/cellulose nanofibers blend. Journal of Power Sources, 400:502-510, 2018. ISSN 0378-7753. doi:10.1016/j.jpowsour.2018.08043.

[76] Byoung Soo Kim and Jonghwi Lee. Directional crystallization of dioxane in the presence of PVDF producing porous membranes. Journal of Crystal Growth, 373:45-49, 2013. ISSN 0022-0248. doi:10.1016/j.jcrysgro.2012.09.005.

[77] Yong Cao, Minjie Liang, Zhiduo Liu, Yuming Wu, Xiaoli Xiong, Chaoyang Li, Xingming Wang, Nan Jiang, Jinhong Yu, and Cheng-Te Lin. Enhanced thermal conductivity for poly(vinylidene fluoride) composites with nano-carbon fillers. RSC Advances, 6:68357-68362, 2016. doi:10.1039/c6ra11178e.

[78] Jeffrey W. Gilman. Flammability and thermal stability studies of polymer layered-silicate (clay) nanocomposites. Applied Clay Science, 15(1-2):31-49, 1999. ISSN 0169-1317. doi: 10.1016/S0169-1317(99)00019-8.

[79] Liumin He, Qinhua Zuo, Yunfeng Shi, and Wei Xue. Microstructural characteristics and crystallization behaviors of poly(L-lactide) scaffolds by thermally induced phase separation. Journal of Applied Polymer Science, 131(4):39436, 2014. doi:10.1002/app.39436.

[80] Kobra Atrak, Ali Ramazani, and Saeid Taghavi Fardood. Green synthesis of amorphous and gamma aluminum oxide nanoparticles by tragacanth gel and comparison of their photocatalytic activity for the degradation of organic dyes. Journal of Materials Science: Materials in Electronics, 29:8347-8353, 2018. doi:10.1007/s10854-018-8845-2.

[81] Nengxin Wei, Jiangnan Hu, Mingzu Zhang, Jinlin He, and Peihong Ni. Cross-linked porous polymer separator using vinyl-modified aluminum oxide nanoparticles as cross-linker for lithium-ion batteries. Electrochimica Acta, 307:495-502, 2019. ISSN 0013-4686. doi:10.1016/j.electacta.2019.04.010.

[82] Xiaomei Cai, Tingping Lei, Daoheng sun, and Liwei Lin. A critical analysis of the α, β and γ phases in poly(vinylidene fluoride) using FTIR. RSC Advances, 7:15382-15389, 2017. doi: 10.1039/c7ra01267e.

[83] Takashi Nishiyama, Takayuki Sumihara, Eriko Sato, and Hideo Horibe. Effect of solvents on the crystal formation of poly(vinylidene fluoride) film prepared by a spin-coating process. Polymer Journal, 49:319-325, 2017. ISSN 0032-3896. doi:10.1038/pj.2016.116.

[84] S. Satapathy, Santosh Pawar, P.K. Gupta, and K.B.R. Varma. Effect of annealing on phase transition in poly(vinylidene fluoride) films prepared using polar solvent. Bulletin of Materials Science, 34(4):727-733, 2011.

[85] Yi Feng, Kun Wang, Chris H. J. Davies, and Huanting Wang. Carbon nanotube/alumina/polyethersulfone hybrid hollow fiber membranes with enhanced mechanical and anti-fouling properties. Nanomaterials, 5(3):1366-1378, 2015. ISSN 2079-499. doi:10.3390/nano5031366.

[86] Yi Feng, Ezzatollah Shamsaei, Chris H.J. Davies, and Huanting Wang. Inorganic particle enhanced polymer hollow fiber membranes with high mechanical properties. Materials Chemistry and Physics, 167:209-218, 2015. ISSN 0254-0584. doi:10.1016/j.matchemphys.2015.10.034.

[87] S. Ahmed and F.R. Jones. A review of particulate reinforcement theories for polymer composites. Journal of Materials Science, 25:4933-4942, 1990. doi:10.1007/bf00580110.

[88] G. Elizabeth Rani, R. Murugeswari, Suchart Siengchin, N. Rajini, and M. Arul Kumar. Quantitative assessment of particle dispersion in polymeric composites and its effect on mechanical properties. Journal of Materials Research and Technology, 19:1836-1845, 2022. ISSN 2238-7854. doi:10.1016/j.jmrt.2022.05.147.

[89] Sergiy Kalnaus, Yanli wang, and John A. Turner. Mechanical behavior and failure mechanisms of Li-ion battery separators. Journal of Power Sources, 348:255-263, 2017. ISSN 0378-7753. doi:10.1016/j.jpowsour.2017.03.003.

[90] Jun-Wei Shen, Hajime Matsumoto, Akira Maki, Toshihiko Kuriyama, Tomoyuki Nemoto, Shunsuke Koido, and Hisao Takeuchi. A study on the relationship between microstructure and mechanical properties of porous polymer films. Polymer, 204:122784, 2020. ISSN 0032-3861. doi:10.1016/j.polymer.2020.122784.

[91] Lu Yan, Yu Shui Li, Chai Bao Xiang, and Shun Xianda. Effect of nano-sized Al_2O_3-particle addition on PVDF ultrafiltration membrane performance.

Journal of Membrane Science, 276(1-2):162-167, 2006. ISSN 0376-7388. doi:10.1016/j.memsci.2005.09.044.

[92] Arun Kumar Solarajan, Vignesh Murugadoss, and Subramania Angaiah. Dimensional stability and electrochemical behavior of ZrO_2 incorporated electrospun PVdF-HFP based nanocomposite polymer membrane electrolyte for Li-ion capacitors. Scientific Reports, 7(1):45390, 2017. doi:10.1038/srep45390.

[93] Xiao-Mao Wang, Xiao-Yan Li, and Kaimin Shih. In situ embedment and growth of anhydrous and hydrated aluminum oxide particles on polyvinylidene fluoride (PVDF) membranes. Journal of Membrane Science, 368(1-2):134-143, 2011. ISSN 0376-7388. doi:10.1016/j.memsci.2010.11.038.

[94] A. Manuel Stephan, Kee Suk Nahm, T. Prem Kumar, M. Anbu Kulandainathan, G. Ravi, and J. Wilson. Nanofiller incorporated poly(vinylidene fluoride-hexafluoropropylene) (PVdF-HFP) composite electrolytes for lithium batteries. Journal of Power Sources, 159(2):1316-1321, 2006. ISSN 0378-7753. doi:10.1016/j.jpowsour.2005.11.055.

[95] Zhaohui Li, Guangyao Su, Xiayu Wang, and Deshu Gao. Micro-porous P(VDF-HFP)-based polymer electrolyte filled with Al_2O_3 nanoparticles. Solid State Ionics, 176(23-24):1903-1908, 2005. ISSN 0167-2738. doi:10.1016/j.ssi.2005.05.006.

[96] F. Croce, L. Persi, B. Scrosati, F. Serraino-Fiory, E. Plichta, and M.A. Hendrickson. Role of the ceramic fillers in enhancing the transport properties of composite polymer electrolytes. Electrochimica Acta, 46(16):2457-2461, 2001. ISSN 0013-4686. doi:10.1016/S0013-4686(01)00458-3.

[97] Bicy K., Shruti Suriyakumar, Anu Paul P., Anu A. S., Nandakumar Kalarikkal, Arul Manuel Stephen, Geethamma V. G., Didier Rouxel, and Sabu Thomas. Highly lithium ion conductive, Al_2O_3 decorated electrospun P(VDF-TrFE) membranes for lithium ion battery separators. New Journal of Chemistry, 42:19505-19520, 2018. doi:10.1039/c8nj01907j.

[98] Jiawen Zhang, Yakang Xiang, Muhammad Imran Jamil, Jianguo Lu, Qinghua Zhang, Xiaoli Zhan, and Fengqiu Chen. Polymers/zeolite nanocomposite membranes with enhanced thermal and electrochemical performances for lithium-ion batteries. Journal of Membrane Science, 564:753-761, 2018. ISSN 0376-7388. doi:10.1016/j.memsci.2018.07.056.

[99] Ahmed Salama and Peter Hesemann. Recent trends in elaboration, processing, and derivatization of cellulosic materials using ionic liquids. ACS Sustainable

Chemistry & Engineering, 8(49):17893-17907, 2020. doi:10.1021/acssuschemeng.0c06913.

[100] Yukinobu Fukaya, Kensaku Hayashi, Masahisa Wada, and Hiroyuki Ohno. Cellulose dissolution with polar ionic liquids under mild conditions: required factors for anions. Green Chemistry, 10:44-46, 2008. doi:10.1039/b713289a.

[101] Xiangming He, Qiao Shi, Xiao Zhou, Chunrong Wan, and Changyin Jiang. In situ composite of nano SiO_2-P(VDF-HFP) porous polymer electrolytes for Li-ion batteries. Electrochimica Acta, 51(6):1069-1075, 2005. ISSN 0013-4686. doi:10.1016/j.electacta.2005.05.048.

[102] Z.H. Li, H.P. Chang, P. Zhang, Y.P. Wu, and X.D. Zhou. Macroporous nanocomposite polymer electrolyte for lithium-ion batteries. Journal of Power Sources, 184(2):562-565, 2008. ISSN 0378-7753. doi:10.1016/j.jpowsour.2008.02.068.

[103] Martin Eden Glicksman. Principles of solidification: an introduction to modern casting and crystal growth concepts. Springer-Verlag, New York, 2011. ISBN 978-1-4419-7343-6. doi:10.1007/978-1-4419-7344-3.

[104] Kristen L. Scotti and David C. Dunand. Freeze casting – a review of processing, microstructure and properties via the open data repository, FreezeCasting.net. Progress in Materials Science, 94:243-305, 2018. ISSN 0079-6425. doi:10.1016/j.pmatsci.2018.01.001.

[105] Marcel Benz, William B. Euler, and Otto J. Gregory. The role of solution phase water on the deposition of thin films of poly(vinylidene fluoride). Macromolecules, 35(7):2682-2688, 2002. doi:10.1021/ma011744f.

[106] Jia-Yi Yin, Carlo Boaretti, Alessandra Lorenzetti, Alessandro Martucci, Martina Roso, and Michele Modesti. Effects of solvent and electrospinning parameters on the morphology and piezoelectric properties of PVDF nanofibrous membrane. Nanomaterials, 12(6):962, 2022. doi:10.3390/nano12060962.

[107] A. Salimi and A.A. Yousefi. Conformational changes and phase transformation mechanisms in PVDF solution-cast films. Journal of Polymer Science Part B: Polymer Physics, 42(18):3487-3495, 2004. ISSN 0887-6266. doi:10.1002/polb.20223.

[108] G. Gnana Kumar, Ae Rhan Kim, Kee Suk Nahm, Dong Jin Yoo, and R. Elizabeth. High ion and lower molecular transportation of the poly vinylidene fluoride-hexa fluoro propylene hybrid membranes for the high temperature and lower humidity direct methanol fuel cell applications. Journal of Power

Sources, 195(18):5922-5928, 2010. ISSN 0378-7753. doi:10.1016/j.jpowsour.2009.11.021.

[109] Xiaorui Zhang, Xue Sun, Tong Lv, Ling Weng, Minghe Chi, Jiahao Shi, and Siqi Zhang. Preparation of PI porous fiber membrane for recovering oil-paper insulation structure. Journal of Material Science: Materials in Electronics, 31:13344-13351, 2020. doi:10.1007/s10854-020-03888-5.

[110] Xin Yang, Liqun Zhu, Yichi Chen, Baiqing Bao, Jinlong Xu, and Weiwei Zhou. Controlled hydrophilic/hydrophobic property of silica films by manipulating the hydrolysis and condensation of tetraethoxysilane. Applied Surface Science, 376:1-9, 2016. ISSN 0169-4332. doi:10.1016/j.apsusc.2016.02.068.

[111] Hao Li, Yue-Ming Chen, Xiao-Ting Ma, Jun-Li Shi, Bao-Ku Zhu, and Li-Ping Zhu. Gel polymer electrolytes based on active PVDF separator for lithium ion battery. I: preparation and property of PVDF/poly(dimethylsiloxane) blending membrane. Journal of Membrane Science, 379(1-2):397-402, 2011. ISSN 0376-7388. Doi:10.1016/j.memsci.2011.06.008.

[112] C.M. Costa, L.C. Rodrigues, V. Sencadas, M.M. Silva, J.G. Rocha, and S. Lancero-Mendez. Effect of degree of porosity on the properties of poly(vinylidene fluoride-trifluorethylene) for Li-ion battery separators. Journal of Membrane Science, 407-408:193-201, 2012. ISSN 0376-7388. doi:10.1016/j.memsci.2012.03.044.

[113] K.M. Abraham. Directions in secondary lithium battery research and development. Electrochimica Acta, 38(9):1233-1248, 1993. ISSN 0013-4686. doi:10.1016/0013-4686(93)80054-4.

[114] J.C. Barbosa, D.M. Correia, R. Goncalves, V. de Zea Bermudez, M.M. Silva, S. Lanceros-Mendez, and C.M. Costa. Enhanced ionic conductivity in poly(vinylidene fluoride) electrospun separator membranes blended with different ionic liquids for lithium ion batteries. Journal of Colloid and Interface Science, 582:376-386, 2021. ISSN 0021-9797. doi:10.1016/j.jcis.2020.08.046.

[115] Dingchang Lin, Pak Yan Yuen, Yayuan Liu, Wei Liu, Nian Liu, Reinhold H. Dauskardt, and Yi Cui. A silica-aerogel-reinforced composite polymer electrolyte with high ionic conductivity and high modulus. Advanced Materials, 30(32):1802661, 2018. ISSN 0935-9648. doi:10.1002/adma.201802661.

[116] Joao Nunes-Pereira, Manab Kundu, Attila Goren, Maria Manuela Silva, Carlos M. Costa, Lifeng Liu, and Senentxu Lanceros-Mendez. Optimization of filler type within poly(vinylidene fluoride-co-trifluoroethylene) composite separator membranes for improved lithium-ion battery performance. Composites Part B:

Engineering, 96:94-102, 2016. ISSN 1359-8368. doi:10.1016/j.compositesb.2016.04.041.

[117] Jung-Hwan Kim, Jeong-Hoon Kim, Eun-Sun Choi, Jong Hun Kim, and Sang-Young Lee. Nanoporous polymer scaffold-embedded nonwoven composite separator membranes for high-rate lithium-ion batteries. RSC Advances, 4:54312-54321, 2014. doi:10.1039/c4ra07994a.

[118] Hyun-Seok Jeong, Eun-Sun Choi, Sang-Young Lee, and Jong Hun Kim. Evaporation-induced, close-packed silica nanoparticle-embedded nonwoven composite separator membranes for high-voltage/high-rate lithium-ion batteries: advantageous effect of highly percolated, electrolyte-philic microporous architecture. Journal of Membrane Science, 415-416:513-519, 2012. ISSN 0376-7388. doi:10.1016/j.memsci.2012.05.038.

[119] Ji-Ae Choi, Sa Heum Kim, and Dong-Won Kim. Enhancement of thermal stability and cycling performance in lithium-ion cells through the use of ceramic-coated separators. Journal of Power Sources, 195(18):6192-6196, 2010. ISSN 0378-7753. doi:10.1016/j.jpowsour.2009.11.020.

[120] Gaofeng Shao, Dorain A. H. Hanaor, Xiaodong Shen, and Aleksander Gurlo. Freeze casting: from low-dimensional building blocks to aligned porous structures – a review of novel materials, methods, and applications. Advanced Materials, 32(17):1907176, 2020. ISSN 0935-9648. doi:10.1002/adma.201907176.

[121] Ruiping Liu, Tingting Xu, and Chang-an Wang. A review of fabrication strategies and applications of porous ceramics prepared by freeze-casting method. Ceramics International, 42(2):2907-2925, 2016. ISSN 0272-8842. doi:10.1016/j.ceramint.2015.10.148.

[122] Aaron Lichtner, Denis Roussel, David Jauffres, Christophe L. Martin, and Rajendra K. Bordia. Effect of macropore anisotropy on the mechanical response of hierarchically porous ceramics, Journal of the American Ceramic Society, 99(3):979-987, 2016. ISSN 0002-7820. doi:10.1111/jace.14004.

[123] Edward W. Washburn. Note on a method of determining the distribution of pore sizes in a porous material. Proceedings of the National Academy of Sciences, 7(4):115-116, 1921. doi:10.1073/pnas.7.4.115.

[124] M.D.M. Innocentini, R.K. Faleiros, R. Pisani Jr. I. Thijs, J. Luyten, and S. Mullens. Permeability of porous gelcast scaffolds for bone tissue engineering. Journal of Porous Materials, 17(5):615-627, 2010. ISSN 1380-2224. doi:10.1007/s10934-009-9331-2.

[125] W. Kurz, D.J. Fisher. Fundamentals of solidification. Trans Tech Publications, Switzerland, 1998. ISBN 9783035732399.

[126] David C. C. Lam, Fred F. Lange, and Anthony G. Evans. Mechanical properties of partially dense alumina produced from powder compacts. Journal of the American Ceramic Society, 77(8):2113-2117, 1994. ISSN 0002-7820. doi:10.1111/j.1151-2916.1994.tb07105.x.

[127] Hai Ni, Xiaodong Li, and Hongsheng Gao. Elastic modulus of amorphous SiO_2 nanowires. Applied Physics Letters, 88(4):043108, 2006. ISSN 0003-6951. doi:10.1063/1.2165275.

[128] Ji-Hao Zuo, Chao Wei, Peng Cheng, Xi Yan, Yan Chen, and Wan-Zhong Lang. Breakthrough the upperbond of permeability vs. tensile strength of TIPS-prepared PVDF membranes. Journal of Membrane Science, 604:118089, 2020. ISSN 0376-7388. doi:10.1016/j.memsci.2020.118089.

[129] Da Li, Guoli Sun, Xueqiong Ouyang, Pei Zhong, and Shuangxi Wang. Surface modification of alumina nanoparticles and its application in tape casting of micro-nano green tape. Applied Surface Science, 622:156963, 2023. ISSN 0169-4332. doi:10.1016/j.apsusc.2023.156963.

[130] Zhao Liu, Lehan Yao, Xun Pan, Qiong Liu, and He Huang. A green and facile approach to the efficient surface modification of alumina nanoparticles with fatty acids. Applied Surface Science, 447:664-672, 2018. ISSN 0169-4332. doi:10.1016/j.apsusc.2018.04.035.

[131] E. Yuliwati and A.F. Ismail. Effect of additives concentration on the surface properties and performance of PVDF ultrafiltration membranes for refinery produced wastewater treatment. Desalination, 273:226-234, 2011. ISSN 0011-9164. doi:10.1016/j.desal.2010.11.023.

[132] Jinhan Chen, Hongjiu Hu, Shuang Li, and Yaolong He. Evolution of mechanical properties of polypropylene separator in liquid electrolytes for lithium-ion batteries. Journal of Applied Polymer Science, 135(27):46441, 2018. doi:10.1002/app.46441.

[133] Sumit Kundu, Leonardo C. Simon, Michael Fowler, and Stephen Grot. Mechanical properties of Nafion[TM] electrolyte membranes under hydrated conditions. Polymer, 46(25):11707-11715, 2005. ISSN 0032-3861. doi:10.1016/j.polymer.2005.09.059.

[134] Margaret F. Talbott, George S. Springer, and Lars A. Berglund. The effects of crystallinity on the mechanical properties of PEEK polymer and graphite fiber

reinforced PEEK. Journal of Composite Materials, 21(11):1056-1081, 1987. doi:10.1177/002199838702101104.

[135] C.M. Costa, M. Kundu, V.F. Cardoso, A.V. Machado, M.M. Silva, and S. Lanceros-Mendez. Silica/poly(vinylidene fluoride) porous composite membranes for lithium-ion battery separators. Journal of Membrane Science, 564:842-851, 2018. ISSN 0376-7388. doi:10.1016/j.memsci.2018.07.092.

A p p e n d i x   A

POST-FREEZE-CASTING INFILTRATION PROCEDURE

Besides the most commonly used electrolytes for sodium ion batteries such as the organic electrolyte and the ionic liquid [1], water-in-salt electrolyte, a hyper-concentrated ionic solution, is highly sought-after for the development of aqueous sodium ion batteries [2]. However, most researchers and scientists still rely on thick glass fiber filter papers as separators [2, 3, 4] due to the lack of suitable separators for these batteries. Our preliminary results show that the wettability of water-in-salt electrolyte with tape/freeze-cast PVDF-HFP membranes can be significantly improved by a post-freeze-casting TEOS infiltration process followed by an *in-situ* sol-gel reaction to introduce more SiO_2 particles into the membranes (Figure A.1). These membranes fabricated via the infiltration process show promise in affinity with the water-in-salt electrolyte. To further evaluate these membranes as prospective separators for aqueous sodium ion batteries, electrochemical properties including ionic conductivity of the membranes and the rate and cycling performance when assembled into coin cells need to be assessed.
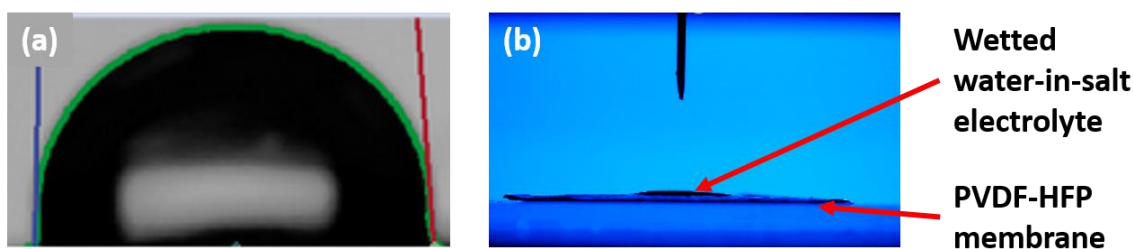
Figure A.1 Contact angle results of water-in-salt electrolyte (17M $NaClO_4$ in water) on (a) PVDF-HFP membrane and (b) PVDF-HFP membrane fabricated by the infiltration process.

A p p e n d i x   B

HIGH-TEMPERATURE FREEZE CASTING

Conventional freeze casting needs to be carried out at cryogenic temperatures, since most commonly used solvents have melting points below room temperature. Some high-melting-point solvents, for example, dimethyl sulfone ($DMSO_2$) with a melting point around 109 $^{\circ}$C, offer the opportunity to perform freeze casting at room temperature, which eliminates the need for cryogenic equipment. From our preliminary results, a PVDF-HFP membrane fabricated with dimethyl sulfone as the solvent at 160 $^{\circ}$C and freeze cast at room temperature exhibits a through-thickness and directionally aligned pore morphology (Figure B.1). Systems such as these require further attention, particularly the design of the high-temperature casting setup including temperature control and choice of substrate material, and the homogeneity of the casting solutions.
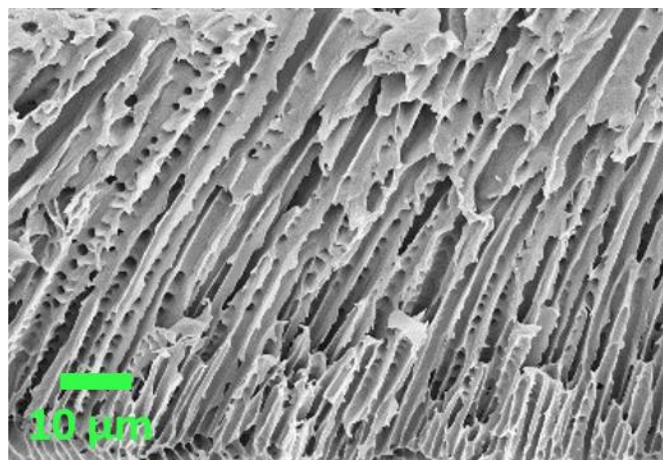
Figure B.1 Cross-sectional micrograph of PVDF-HFP membrane fabricated with dimethyl sulfone as the solvent at 160 $^{\circ}$C and freeze cast at room temperature.

A p p e n d i x   C

CELLULOSE-BASED AND POLYIMIDE MEMBRANES

Cellulose, abundant with hydroxyl groups in molecules, exhibits a high degree of hydrophilicity. Therefore, cellulose is a candidate separator material for aqueous sodium ion battery studies [5]. However, the brittle nature of cellulose fibers limits their use as a separator from a mechanical standpoint. Blending cellulose with another less brittle polymer may be beneficial in this regard. Our preliminary results show that a blend of cellulose and PVDF-HFP dissolved in DMSO can be used to produce cellulose-based membranes with pore directionality via tape/freeze casting as shown in Figure C.1 (a). In order to demonstrate the efficacy of these cellulose-based membranes as separators, further testing including electrolyte affinity, mechanical response, and rate and cycling performance of coin cells need to be carried out.

Polyimide (PI) separators are also long desired in the battery industry, since the high thermal stability of polyimide ($> 300 \ ^{\circ}C$) can reduce the risk of thermal runaway of batteries [6]. Although DMSO is found to be a good solvent for the commercial polyimide, Matrimid 5218, and a polyimide membrane can be tape/freeze-cast from the polyimide/DMSO solution, this membrane exhibits a relatively dense microstructure as shown in Figure C.1 (b). The absence of through-thickness pores and the presence of a bi-layer microstructure in this membrane suggests that the polyimide/DMSO solution may have undergone a non-solvent induced phase separation (NIPS) rather than freeze casting [7]. A more detailed study on the interaction between polyimide and DMSO in the solution is required if any application of such system is envisioned.
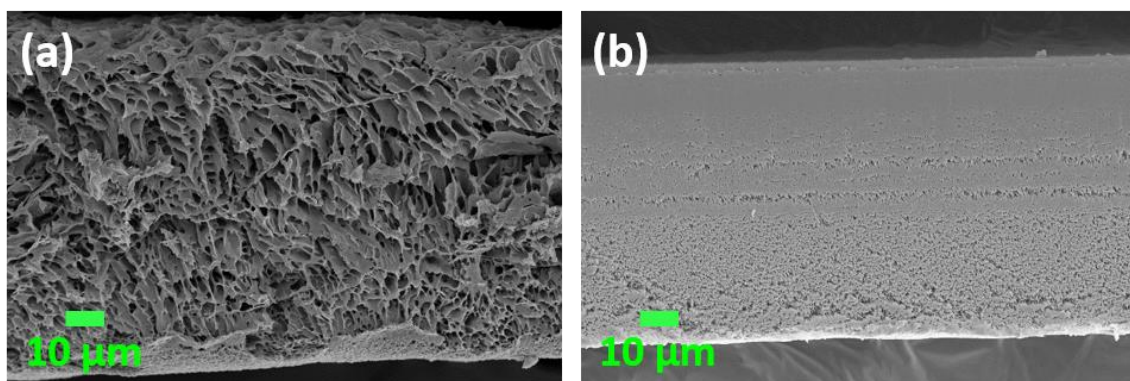
Figure C.1 Cross-sectional micrographs of (a) cellulose/PVDF-HFP membrane (b) polyimide membrane made with dimethyl sulfoxide as the solvent via tape/freeze casting.

REFERENCES

[1] Alexandre Ponrouch, Elena Marchante, Matthieu Coutry, Jean-Marie Tarascon, and M. Rosa Palacin. In search of an optimized electrolyte for Na-ion batteries. Energy and Environmental Science, 5:8572-8583, 2012. doi:10.1039/c2ee22258b.

[2] Liumin Suo, Oleg Borodin, Yuesheng Wang, Xiaohui Rong, Wei Sun, Xiiulin Fan, Shuyin Xu, Marshall A. Schroeder, Arthur V. Cresce, Fei Wang, Chongyin Yang, Yong-Sheng Hu, Kang Xu, and Chunsheng Wang. "Water-in-salt" electrolyte makes aqueous sodium-ion battery safe, green, and long-lasting. Advanced Energy Materials, 7(21):1701189, 2017. ISSN 1614-6832. doi:10.1002/aenm.201701189.

[3] Liwei Jiang, Lilu Liu, Jinming Yue, Qiangqiang Zhang, Anxing Zhou, Oleg Borodin, Lumin Suo, Hong Li, Liquan Chen, Kang Xu, and Yong-Sheng Hu. High-voltage aqueous Na-ion battery enabled by inert-cation-assisted water-in-salt electrolyte. Advanced Materials, 32(2):1904427, 2020. ISSN 0935-9648. doi:10.1002/adma.201904427.

[4] Jin Han, Maider Zarrabeitia, Alessandro Mariani, Zenonas Jusys, Maral Hekmatfar, Huang Zhang, Dorin Geiger, Ute Kaiser, R. Jurgen Behm, Alberto Varzi, and Stefano Passerini. Halide-free water-in-salt electrolytes for stble aqueous sodium-ion batteries. Nano Energy, 77:105176, 2020. ISSN 2211-2855. doi:10.1016/j.nanoen.2020.105176.

[5] Varisara Deerattrakul, Phonghot Sakulaue, Aritsa Bunpheng, Wasawat Kraithong, Aniwat Pengsawang, Pongkarn Chakthranont, Pawin Iamprasertkun, and Vorranutch Itthibenchapong. Introducing hydrophilic cellulose nanofiber as a bio-separator for "water-in-salt" based energy storage devices. Electrochimica Acta, 453:142355, 2023. ISSN 0013-4686. doi:10.1016/j.electacta.2023.142355.

[6] Ziheng Lu, Fan Sui, Yue-E Miao, Guohua Liu, Cheng Li, Wei Dong, Jiang Cui, Tianxi Liu, Junxiong Wu, and Chunlei Yang. Polyimide separators for rechargeable batteries. Journal of Energy Chemistry, 58:170-197, 2021. ISSN 2095-4956. doi:10.1016/j.jechem.2020.09.043.

[7] Darrell A. Patterson, Alice Havill, Sarah Costello, Yoong Hsiang See-Toh, Andrew G. Livingston, and Adrian Turner. Membrane characterization by SEM, TEM and ESEM: The implications of dry and wetted microstructure on mass transfer through integrally skinned polyimide nanofiltration membranes. Separation and Purification Technology, 66(1):90-97, 2009. ISSN 1383-5866. doi:10.1016/j.seppur.2008.11.022.